

**Investigating Self-Assembled
Protein Nanotubes
Using Atomic Force Microscopy**

Lijiang NIU BSc. MSc.

**Thesis submitted to the University of Nottingham
for the degree of Doctor of Philosophy**

July 2009

温故而知新

By reviewing the old, gain the knowledge of the new.

孔子

Confucius

Abstract

Self-assembled protein nanotubular materials are attractive as putative building blocks for a variety of applications. Knowledge of the three-dimensional structures and the physical properties of these protein nanotubes then becomes a prerequisite for their use in rational materials design. The main purpose of the work presented in this thesis is to investigate both the structural and mechanical properties of protein nanotubes utilizing atomic force microscopy (AFM). Several different protein nanotubes will be used as exemplars to develop AFM methods.

AFM is capable of both visualizing and monitoring dynamic processes. Within this thesis, not only could the change in morphology of protein nanotubes be visualized by AFM, but also changes in their mechanical properties were monitored as dynamic processes. For example, changes in the morphology (in chapter 3) and flexibility (in chapter 4) of lysozyme fibrils during fibrillization were investigated.

Chapters 4 to 6 describe a range of different methods to obtain the mechanical properties of protein nanotubes: the persistence length method (chapter 4), the adhesive interaction method (chapter 5) and the bending beam method (chapter 6). All of these had their own advantages. However, each method was found only to be suitable for protein nanotubes with elasticities within a defined range.

The protein nanotubes investigated by AFM in the thesis included *Salmonella* flagellar filaments, lysozyme fibrils and diphenylalanine (FF) nanotubes. All of the investigated protein nanotube structures had Young's moduli lying between

that of gelatin and bone. This highlights their potential, in terms of mechanical properties, for a range of applications in drug-delivery systems and tissue-engineering scaffolds. In future, if a database of mechanical properties of protein nanotubes could be built up using the AFM methods developed and utilized within this thesis, the development of the applications of protein nanotubes will be accelerated, as the right protein nanotubes will be selected for appropriate applications.

Acknowledgements

I would like to thank my supervisors, Professor Saul J. B. Tendler and Dr. Stephanie Allen, for their guidance and various contributions towards this thesis and their constant support.

I would like to thank all my colleagues within the LBSA group for their support and a lot of useful discussions. Many thanks to Dr Xinyong Chen for his help with lots of AFM technical issues and to Dr. Alberto Orta for developing software Veca for data analysis in this thesis.

I wish to thank Dr. Richard Woods (Genetics group, Queen's Medical Centre) for kindly providing *Salmonellar* flagellar filament samples and showing me the sample preparation process. I also thank Dr. Claudio Canale (Università degli Studi di Genova, Italy) for kindly providing β 2-microglobulin protein samples.

I would like to thank all the lovely friends I have made in Nottingham. I thank my parents for always being supportive and forgiving to me. Last but not least I thank my husband and my daughter for being in my life.

List of Contents

Abstract	i
Acknowledgements	iii
List of Contents	iv
List of Tables	ix
List of Figures	x
Chapter 1 Introduction: Protein Nanotubes Are Novel Bio-inspired Materials ..	1
1.1 Protein Nanotubes	1
1.2 Bacterial Flagellar Filaments	4
1.2.1 Bacterial Flagellum	4
1.2.1.1 Motor Function	4
1.2.1.2 Overall Structure	5
1.2.1.3 Self-assembly Process	5
1.2.2 The Bacterial Flagellar Filament	8
1.2.2.1 Bacterial Flagellin	10
1.2.2.2 Intersubunit Interactions in the Filament	11
1.2.2.3 Transformations of Flagellar Filaments in vitro	15
1.2.3 Applications of Bacterial Flagellar Filaments	17
1.3 Amyloid Fibrils	20
1.3.1 Protein Misfolding	20
1.3.1.1 Protein Misfolding and Diseases	20
1.3.1.2 Energy Landscape of Protein Folding	22

1.3.1.3 Structure of Amyloid Fibrils	24
1.3.2 Applications of Amyloid Fibrils	29
1.3.3 Diphenylalanine Nanotubes (FF Nanotubes)	33
1.3.3.1 Discovery and Synthesis of Diphenylalanine Nanotubes	33
1.3.3.2 Structures and Properties of diphenylalanine Nanotubes.....	35
1.3.3.3 Applications of Diphenylalanine Nanotubes	39
1.4 Aims and Outline of Research	42
Chapter 2 Instrumental and Experimental Methods	44
2.1 Atomic Force Microscopy	44
2.1.1 Atomic Force Microscopy.....	44
2.1.1.1 Principle of AFM	45
2.1.1.2 Operation Modes of AFM.....	47
2.1.1.3 Force Measurements by AFM.....	48
Conversion of force curves	49
Problem of zero tip-sample distance.....	50
Determination of spring constant of the cantilever.....	52
2.1.2 AFM Analysis	54
AFM Imaging.....	54
AFM force measurements.....	55
2.1.3 Image Processing	55
2.2 Preparation of Protein Nanotubes	56
2.2.1 Bacterial Flagellar Filaments	56
2.2.2 Lysozyme Fibrils.....	57
2.2.3 β 2-Microglobulin Fibrils.....	57

3.3 Alternative Assembly of Tubular and Spherical Nanostructures from FF Peptides	90
3.4 Conclusion	95
Chapter 4 Persistence Length Study of Protein Nanotubes	96
4.1 Theory and Method	96
4.1.1 Persistence Length is a Measure of the Flexibility of a Filament	96
4.1.2 Analysing AFM Images of Nanofibrils and Nanotubes to Obtain Their Persistence Lengths	98
4.2 The Persistence Length of Flagellar Filaments in Different Environments	103
4.3 Change of Flexibility during Fibrillization of Lysozyme Fibrils	108
4.4 Flexibility of diphenylalanine Fibrils	111
4.5 Conclusion	113
Chapter 5 Using the Adhesive Interaction between AFM Tips and Sample Surfaces to Measure the Elasticity of Protein Nanotubes	115
5.1 Theory and Method	115
5.1.1 The JKR (Johnson, Kendall and Roberts) Model	115
5.1.2 Applying JKR Model to Obtain the Young's Modulus of a Sample ..	121
5.2 The Effects of the Ionic Strength on the Elasticity of <i>Salmonella</i> Flagellar Filaments	125
5.3 Investigating the Interaction between <i>Salmonella</i> Flagellar Filaments and Mica Substrates in Electrolyte Environments	129
5.4 Conclusion	133

Chapter 6 Using the Bending Beam Model to Estimate the Elasticity of Protein Nanotubes	134
6.1 Theory	134
6.1.1 Deformation of a Fixed-End Bending Beam	134
6.1.2 Applying the Bending Beam Model to Nanotubes	135
6.2 β 2-microglobulin Fibrils Lying over Gaps within the Gold Substrate	137
6.3 Elasticity of diphenylalanine Fibrils	139
6.3.1 Elasticity of FF Nanotubes at Room Temperature.....	140
What is a “good” deflection?	140
Is the deflection reversible?	142
Obtaining E and G.....	143
Determination of D effects the resulting E and G.....	145
6.3.2 Effect of Temperature on the Elasticity of FF	146
6.3.3 Effect of Humidity on the Elasticity of FF Nanotubes	149
6.4 Conclusion	151
Chapter 7 Final Conclusions: AFM is a Powerful Tool for Investigating the Properties of Protein Nanotubes	153
7.1 AFM Methods of Investigating Protein Nanotubes	153
7.2 The Mechanical Properties of Protein Nanotubes.....	155
7.3 Future Directions.....	156
References.....	158
Publication	174

List of Tables

Table 1-1 Examples of amyloidogenic peptides and proteins.....	21
Table 3-1 The dimensions of <i>Salmonella</i> flagellar filaments observed in AFM images obtained in liquid.	69
Table 3-2 The average height of <i>Salmonella</i> flagellar filaments on gold surface in a series of propanol-water mixtures.	75
Table 3-3 The average heights of 6 types of lysozyme fibrils observed.	83
Table 3-4 The predicated heights using Khurana’s model (2003).	84
Table 3-5 The predicated heights using the “n+1” model.	85
Table 3-6 The summary of the experimental data of the heights of lysozyme fibrils and the heights predicted by Khurana’s model and “n+1” model.	86
Table 4-1 <i>Salmonella</i> flagellar filaments in different environments.....	106
Table 4-2 Persistence length of lysozyme protofilaments and fibrils of different assembly levels during fibrillization.	108
Table 5-1 Young’s modulus E of <i>Salmonella</i> flagellar filaments in buffer solutions with different concentrations of Mg^{2+}	125
Table 5-2 Young’s modulus E of <i>Salmonella</i> flagellar filaments in buffer solutions with different ionic strength.	126
Table 5-3 Summary of Young’s modulus E of <i>Salmonella</i> flagellar filaments in different buffer solutions.	126
Table 6-1 The reversible indentation of a FF nanotube over a hole under the loading force of AFM tip.	142

List of Figures

Figure 1-1 Ghadiri <i>et al.</i> protein nanotubes.	2
Figure 1-2 Electron micrograph of a negatively-stained bacterium, <i>Salmonella typhimurium</i>	4
Figure 1-3 Schematic diagrams showing the overall architecture of the bacterial flagellum.	6
Figure 1-4 Outward assembly pathway of the flagellum.	9
Figure 1-5 The C α backbone trace, hydrophobic side-chain distribution and structural information of flagellin.	11
Figure 1-6 Polymorphic model of the filament.	12
Figure 1-7 The surface lattice of L- and R-type straight flagellar filaments.	13
Figure 1-8 Three-dimensional density map of the flagellar filament (R-type straight filament), calculated by including data up to 9 Å.	14
Figure 1-9 Ribbon diagram of the C α backbone of the filament model in stereo view.	15
Figure 1-10 Dark field light micrographs of <i>Salmonella</i> flagellar filaments.	17
Figure 1-11 TEM images of disulfide cross-linked Cys-loop flagella bundles stained with 2% phosphotungstic acid (pH7.5).	19
Figure 1-12 TEM images of gold nanoparticles that were synthesized by reduction of Au(I) on a histidine loop peptide flagella scaffold.	19
Figure 1-13 Stereo ribbon diagram of the structure of (a) lysozyme (b) beta2-microglobulin.	22

Figure 1-14 The estimated energy landscape diagram based on data for the folding of lysozyme.. 23

Figure 1-15 A molecular model of an amyloid fibril grown from an SH3 domain. 25

Figure 1-16 Khurana’s model for the hierarchical assembly of insulin into amyloid fibrils..... 26

Figure 1-17 A general scheme of the multipathway fibrilization of insulin. 27

Figure 1-18 AFM height images of insulin amyloid..... 28

Figure 1-19 AFM images of 0.1% (w/w) insulin, aggregated at 60 °C for six days in: (a) water; (b) 5% (w/w) EtOH; (c) 20% (w/w) EtOH; (d) 40% (w/w) EtOH . 29

Figure 1-20 Gold and silver enhancement of NM fibres.. 31

Figure 1-21 Electrical behavior of NM-templated metallic fibres..... 32

Figure 1-22 (a) Schematic structure of FF. (b) The molecular structure of FF from the single crystal structure determination.. 34

Figure 1-23 Model for the construction of hollow FF fibres.. 36

Figure 1-24 SEM images of controlled patterning of aligned diphenylalanine nanotubes. 38

Figure 1-25 AFM topography images of aligned FF nanotubes..... 38

Figure 1-26 Casting of silver nanowires with the peptide nanotubes. 39

Figure 1-27 SEM images of (a) peptide nanotubes and nanovesicles containing Pt particles (inset: tilted image showing the tubes are hollow) and (b) a high resolution TEM image showing the 2 nm Pt nanoparticles embedded in the wall of a platinum nanotube..... 40

Figure 1-28 Integrating FF nanotubes in micro-fabrication processes.. 41

Figure 2-1 Schematic of the concept of AFM and the optical lever.	46
Figure 2-2 Photos of a general purpose silicon nitride cantilever produced by Veeco Probes.....	46
Figure 2-3 A model force measurement curve recorded for an infinitely hard material surface with no surface forces.....	50
Figure 2-4 A force measurement retracting curve for a deformable material with attraction and adhesion forces.....	51
Figure 2-5 Measurement of the dimensions of a protein nanotube from an AFM height image using SPIP.	56
Figure 2-6 AFM height image of gold substrate obtained using evaporation gold coater.....	59
Figure 2-7 An AFM height image of a micropatterned silicon substrate with holes of $5\ \mu\text{m} \times 5\ \mu\text{m}$ and 200 nm in depth.	59
Figure 3-1 Tapping mode AFM height images of <i>Salmonella</i> flagellar filaments in air on mica.....	63
Figure 3-2 Histogram of the contour length measured for <i>Salmonella</i> flagellar filaments on mica in air.....	64
Figure 3-3 A sketch demonstrates that Mg^{2+} works as a bridge between flagellar filaments and the mica surface in pH 7.0 buffer solution.	64
Figure 3-4 A height image of <i>Salmonella</i> flagellar filaments taken in pH 7.0 buffer solution (10 mM PBS & 10 mM MgCl_2) using tapping mode AFM.	66
Figure 3-5 A height image of <i>Salmonella</i> flagellar filaments taken in HCl solution (pH 4.4) using tapping mode AFM.	67

Figure 3-6 A height image of *Salmonella* flagellar filaments taken in pH 10.0 solution (0.1mM NaOH & 10 mM MgCl₂) using tapping mode of AFM. 68

Figure 3-7 Sketch of an example of "tip broadening" effect on a filament. 69

Figure 3-8 A height image of *Salmonella* flagellar filaments taken in pH 4.0 solution using tapping mode of AFM. 71

Figure 3-9 Height images of *Salmonella* flagellar filaments in liquid using tapping mode AFM. 72

Figure 3-10 Tapping mode AFM height images of *Salmonella* flagellar filaments in air on gold. 74

Figure 3-11 Tapping mode AFM height images of *Salmonella* flagellar filaments in 80% propanol on gold. 75

Figure 3-12 A plot of average height of *Salmonella* flagellar filaments vs. percentage of propanol in propanol-water buffer. 76

Figure 3-13 An AFM height image of 10 mM glycine buffer obtained using tapping mode AFM before (a) and after (b) incubation at 57 ± 2 °C for 2 weeks. 78

Figure 3-14 An AFM height image in tapping mode of 10mg/mL lysozyme in 10mM glycine buffer at pH 2.0. 79

Figure 3-15 Histogram of the height of lysozyme particles before incubation measured from AFM images taken on mica in air. 79

Figure 3-16 An AFM height image of lysozyme after 3 days of incubation. 80

Figure 3-17 AFM image of one lysozyme fibril with clear periodicity after 2 days of incubation. 81

Figure 3-18 AFM height image of lysozyme fibrils after 4 days of incubation... 82

Figure 3-19 A model for the hierarchical assembly of insulin into amyloid fibrils..
..... 84

Figure 3-20 “n+1” model for lysozyme fibrils assembly. 85

Figure 3-21 An AFM height image of a lysozyme fibril after 4 days of incubation.
..... 87

Figure 3-22 An AFM height image of lysozyme fibrils after 11 days of
incubation..... 88

Figure 3-23 AFM height images of lysozyme fibrils after 14 days of incubation.
..... 89

Figure 3-24 AFM image of typical long and thick FF nanotubes along with short
and thin fibrillar structures. 91

Figure 3-25 SEM images of (a) peptide nanotubes and (b) a mixture of nanotubes
and vesicles 92

Figure 3-26 An AFM image of FF nanostructures self-assembled at 40°C..... 94

Figure 3-27 An AFM image of FF nanostructures self-assembled at 65°C..... 94

Figure 4-1 A sketch of a thin flexible filament. 97

Figure 4-2 An AFM tapping mode height image of *Salmonella* flagellar filaments
observed on mica in air. 99

Figure 4-3 Use of “Freehand” tool to trace the contour of a filament within Veca.
..... 99

Figure 4-4 The contour of the filament shown in **Figure 4-2** is digitalised to XY-
coordinate sets here. 101

Figure 4-5 Persistence length P against contour segment length l 102

Figure 4-6 The plot of the mean square end-to-end distance $\langle R^2 \rangle$ against the contour length s of the filament on **Figure 4-2**..... 102

Figure 4-7 Histogram of the persistence length obtained for *Salmonella* flagellar filaments on mica in air through the application of **Equation 4-2**. 104

Figure 4-8 Tapping mode AFM height image of *Salmonella* flagellar filaments in air on gold. 105

Figure 4-9 AFM image of FF nanotubes..... 112

Figure 5-1 The adhesive interaction between the AFM tip and the sample..... 116

Figure 5-2 A force-versus-displacement approach curve. 121

Figure 5-3 The force-versus-indentation retract curve from the same experiment of **Figure 5-2**. (a) is the whole retract curve and (b) is zoomed part of the curve. Reading from (b), there are $P_{\delta=0} = 0.69$ nN and $\delta_{P=0} = 6.7$ nm. 122

Figure 5-4 Histogram of Young's modulus E of *Salmonella* flagellar filaments on mica in PBS buffer with $MgCl_2$ ($I = 0.1$ M, $c_{PBS} = 0.01$ M, $c_{Mg^{2+}} = 0.01$ M, pH 7.0) obtained using adhesive interaction method. 124

Figure 5-5 The force-versus-indentation retract curve from the control experiment..... 124

Figure 5-6 Young's modulus E of *Salmonella* flagellar filaments versus the ionic strength I of buffer solutions. 127

Figure 5-7 A force-versus-indentation retracting curve of *Salmonella* flagellar filaments on mica surface in pH 7.0 buffer ($c_{PBS} = 0.01$ M) without Mg^{2+} 130

Figure 5-8 Histogram of desorption forces of *Salmonella* flagellar filaments from mica surface in pH 7.0 buffer without Mg^{2+} 131

Figure 6-1 Schematic of the suspended beam configuration produced by a protein nanotube lying over a cavity on the substrate. 136

Figure 6-2 AFM height image of β 2-microglobulin fibrils after 5 days of incubation. 138

Figure 6-3 AFM image of β 2-microglobulin fibrils obtained in water on gold surfaces. 138

Figure 6-4 Examples of FF nanotubes lying over holes of the silicon substrate with different deflections. 141

Figure 6-5 AFM images of a single FF nanotube on a silicon grid. 144

Figure 6-6 The graph of $1/E_{\text{bending}}$ against $1/L^2$ of the fibril in **Figure 6-5**. 144

Figure 6-7 AFM images of FF nanotubes at different temperatures. 147

Figure 6-8 AFM images of FF nanotubes at different relative humidities. 150

Figure 7-1 Young's modulus of different materials. 156

Chapter 1 Introduction: Protein Nanotubes Are Novel Bio-inspired Materials

Self-assembled protein nanotubular materials are attractive as potential building blocks for a variety of applications, not only because of their biocompatibility and chemical modifiability, but also because of their large-scale production ability and manufacture through simple experimental procedures in laboratories. Knowledge of the three-dimensional structures and the physical properties of these protein nanotubes then becomes a prerequisite for rational materials design. The main purpose of the work presented in this thesis is to investigate how to obtain the structural and mechanical information of protein nanotubes.

In this chapter, I will firstly review the previous studies on the synthesis, properties and applications of protein nanotubes, with a particular focus on the systems studied in this thesis, namely, bacterial flagellar filaments and amyloid fibrils. I will then outline the aim and the design of the work presented in the subsequent chapters in this thesis.

1.1 Protein Nanotubes

There has been rapid progress in the development of nano-scale materials, such as nanowires, nanotubes and nanoparticles. Carbon nanotubes have attracted a great deal of attention and have been used for a number of nano-scale devices. Some of these devices show significant improvements compared to existing devices (Chen *et al.* 2003; Fennimore *et al.* 2003; Modi *et al.* 2003; Melosh *et al.*

2003; Zhong *et al.* 2003). However, carbon nanotubes have been produced by expensive techniques, including arc discharge (Ebbesen and Ajayan 1992), laser ablation (Guo *et al.* 1995a; 1995b), and chemical vapor deposition (CVD) (Li *et al.* 1996). Most of these processes take place in vacuum or with process gases.

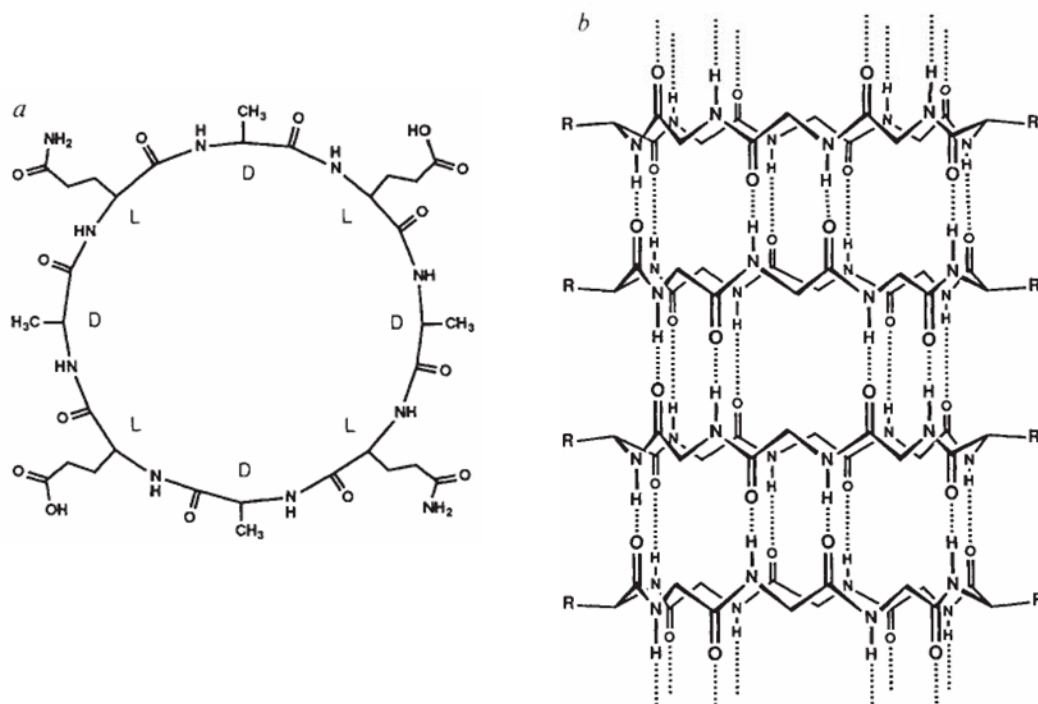


Figure 1-1 Ghadiri *et al.* protein nanotubes. (a) The chemical structure of the peptide subunit. (b) Self-assembled tubular configuration (figure adapted from Ghadiri *et al.* 1993).

Protein nanotubes have structures that possess a well-defined hollow cylinder with a diameter range of 0.5-500nm and an aspect ratio greater than five (Gao 2005). Ghadiri *et al.* brought the definition of protein nanotubes (PNT's) into history by demonstrating that cyclic polypeptides with an even number of alternating D- and L-amino acids can self-assemble into a desired nanotubular structure through intermolecular hydrogen bonding (**Figure 1-1**) (Ghadiri *et al.*

1993). Since then, protein nanotubes have been employed in order to both explore and control molecular aggregation processes (via non-covalent interactions) and to understand the underlying mechanisms of prion and neurodegenerative diseases (Greig and Philip 2001; Harper and Lansbury 1997; Sipe and Cohen 2000). Recently, studies have also been carried out on how to use protein nanotubes as nano-scale devices. The advantages of this over the use of other materials is that, 1) protein nanotubes can be produced by self-assembly processes in vivo and in vitro under mild conditions, ie. room temperature and atmospheric pressure; 2) protein nanotubes can be produced at a large-scale with relatively small cost; 3) smart functionalities for cross-linking and conjugation to other molecules can be added at desired positions in protein nanotubes through well-established chemical and peptide synthetic methods. However, this field is still in the early stages of development. Most of the reports in the literature are of protein nanotubes synthesis (Zhao *et al.* 2008); though some promising results of their use in applications are beginning to appear. The potential applications of protein nanotubes include for targeted drug-delivery systems, tissue-engineering scaffolds and biosensing devices (Krejcova and Rabiskova 2008; Djalali *et al.* 2003; Zhang 2003; Bong *et al.* 2001; Bong and Ghadiri 2001; Yemini *et al.* 2005a; 2005b). In order to discover more potential applications of protein nanotubes, studies of their morphology and physical properties becomes a prerequisite.

1.2 Bacterial Flagellar Filaments

1.2.1 Bacterial Flagellum

1.2.1.1 Motor Function

Bacteria swim actively in liquid environments. They can sense stimuli such as chemicals (Mesibov and Adler 1972; Seymour and Doersch 1973; Tso and Adler 1974) and temperature (Maeda *et al.* 1976) in their immediate environment and change their swimming patterns to move towards favourable, or away from unfavourable conditions, for their survival. These behaviours are called taxis. The bacterial flagellum is the organelle by means of which bacteria swim (**Figure 1-2**).

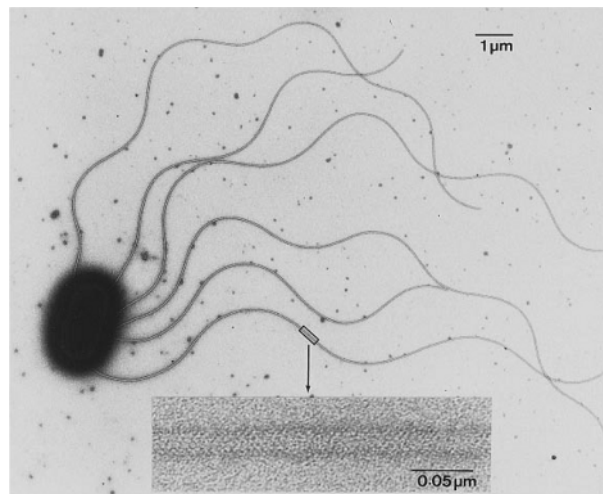


Figure 1-2 Electron micrograph of a negatively-stained bacterium, *Salmonella typhimurium* (figure adapted from Namba and Vonderviszt 1997).

Bacteria swim by rotating their flagellar filaments (Yonekura *et al.* 2002). The fuel for rotation is the membrane gradient of ions, H^+ in most neutrophiles and Na^+ in alkalophiles and marine *Vibrio* species (Hirota *et al.* 1981). The proton-

driven motor rotates at 300 Hz, whereas the sodium-driven motor rotates at up to 1700 Hz (Berry and Armitage 1999; Berg 2002; Oster and Wang 2003). In most species, the motors can rotate either clockwise (CW) or counter clockwise (CCW), and cells direct their movement by regulating switching between the two directions. In *Escherichia coli* or *Salmonella*, for example, CCW rotation allows several filaments on a cell to join in a bundle and drive the cell smoothly forward (a ‘run’), whereas CW rotation disrupts the filament bundle and causes rapid somersaulting (a ‘tumble’) (Blair 2003). This leads to the tactic behaviour, moving towards environments that promote survival (Namba and Vonderviszt 1997; Yonekura *et al.* 2002) at a speed of several body lengths a second (Berry and Armitage 1999).

1.2.1.2 Overall Structure

The flagellum consists of a helical filament connected via the hook to the so-called ‘basal-body’, which is surrounded by a ring of torque-generating particles in the cytoplasmic membrane (**Figure 1-3**). These particles are anchored to the cell wall and are necessary for torque generation. In mechanical terms, the filament is the propeller, and the basal-body and torque-generating particles together are the motor. Within the motor, the basal-body is the ‘rotor’ and rotates (along with the hook and filament) relative to the anchored torque-generating particles or ‘stator’ (Berry and Armitage 1999).

1.2.1.3 Self-assembly Process

The assembly process of the bacterial flagellum starts from the formation of the FliF ring (also called the MS ring, see **Figure 1-3**) complex in the cytoplasmic

membrane, and proceeds in both inward and outward directions, as well as laterally (Figure 1-4) (Namba and Vonderviszt 1997).

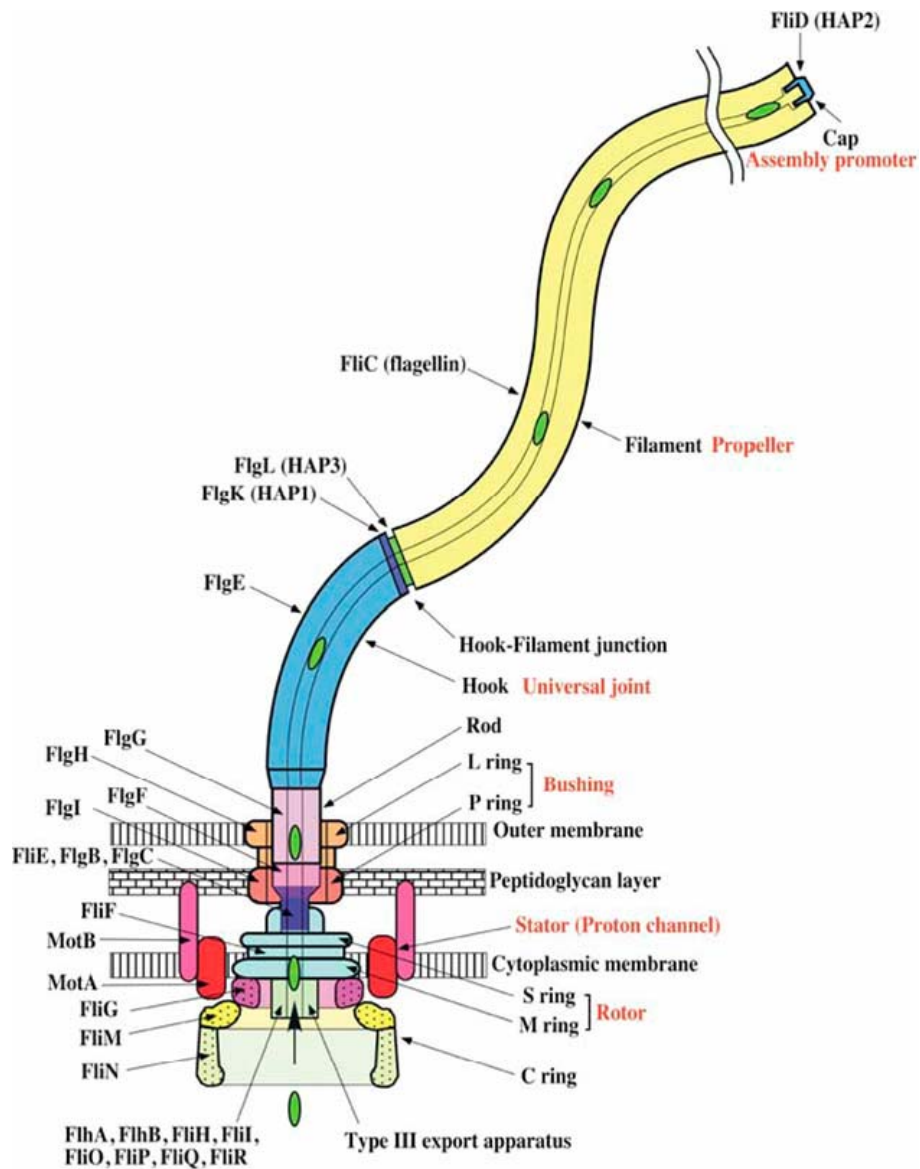


Figure 1-3 Schematic diagrams showing the overall architecture of the bacterial flagellum. Different colours represent different protein components. The filament growth occurs by polymerization of flagellin below the cap (figure adapted from Yonekura *et al.* 2002).

The inward assembly involves the formation of the C-ring, which is also called the switch complex, made of FliG, FliM and FliN (**Figure 1-3**), in the cytoplasmic space. The switch complex regulates the reversal frequency of the motor rotation and is also involved in torque generation. The type III protein export apparatus, which is homologous to those that enable pathogenic bacteria to secrete virulence factors (Kubori *et al.* 1998), is then formed within the C-ring, enabling the export of the flagellar axial proteins through its central channel. The lateral assembly involves the MotA/MotB complex (**Figure 1-3**) in the inner membrane, where it forms a proton channel. This complex acts as the stator by anchoring the periplasmic domain of MotB to the peptidoglycan layer.

The outward assembly (**Figure 1-4**) of the flagellar axial structure, which is the major process in the formation of the flagellum in terms of the mass fraction involved, proceeds at the distal end, as it was initially found for filament growth. The L-P ring (**Figure 1-3**) assembly is an exception, in which the subunit proteins, FlgH and FlgI (**Figure 1-3**), assemble in the outer membrane and peptidoglycan layer, respectively, to form a bushing. For all axial structure formation, the type III protein export system selectively binds and translocates flagellar axial proteins into the central channel of the flagellum by using the energy of ATP hydrolysis (Fan *et al.* 1997; Minamino and Macnab 1999). The axial proteins construct the rod, the hook, the hook-filament junction and the long filament in that order. The rod, composed of five proteins, is connected to the FliF ring (**Figure 1-3**) at its proximal portion with the hook at its distal end, and traverses the inside of the L-P ring. FlgE assembles (**Figure 1-3**) in a helical manner to form the hook. In most species examined, the hook is a short curved structure slightly thicker than the

filament (about 20nm) (Berry and Armitage 1999) and showing a high bending flexibility, which works as a universal joint.

A capping complex made of FlgD (**Figure 1-3**) is attached at the distal end of the hook until it grows up to a length of about 55 nm. Then the FlgD cap falls off the tip of the hook (Ohnishi *et al.* 1994) and is replaced by FlgK, and then FlgL and FliD are transported and bound at the distal end in that order. FlgK, FlgL and FliD are also called hook-associated proteins, HAP1, HAP3 and HAP2, respectively, because the hook-HAP1-HAP3-HAP2 complex is formed momentarily before the initiation of flagellin assembly into the long helical filament (Homma and Iino 1985).

Flagellin travels a long way through the narrow tunnel, only 3 nm in diameter but up to 10–15 μm long, to the distal end of the growing flagellum, which assembles with helical symmetry into the mechanically stable filamentous structure to function as a helical propeller (**Figure 1-4**). The filament cap made of HAP2 is always attached at the distal end, promoting the efficient assembly process (Yonekura *et al.* 2002). The cap has five legs that leave room for only one flagellin subunit at a time, and it counter rotates to accommodate insertion of additional subunits, one after another (Berg 2003).

1.2.2 The Bacterial Flagellar Filament

The flagellar filament has a tubular structure. Varying with the species, the flagellar filament is about 12-25 nm in diameter but grows up to a length of around 15 μm (Kamiya and Asakura 1976b). The central channel through the flagellar filament is about 2.5-3.0 nm (Namba and Vonderviszt 1997).

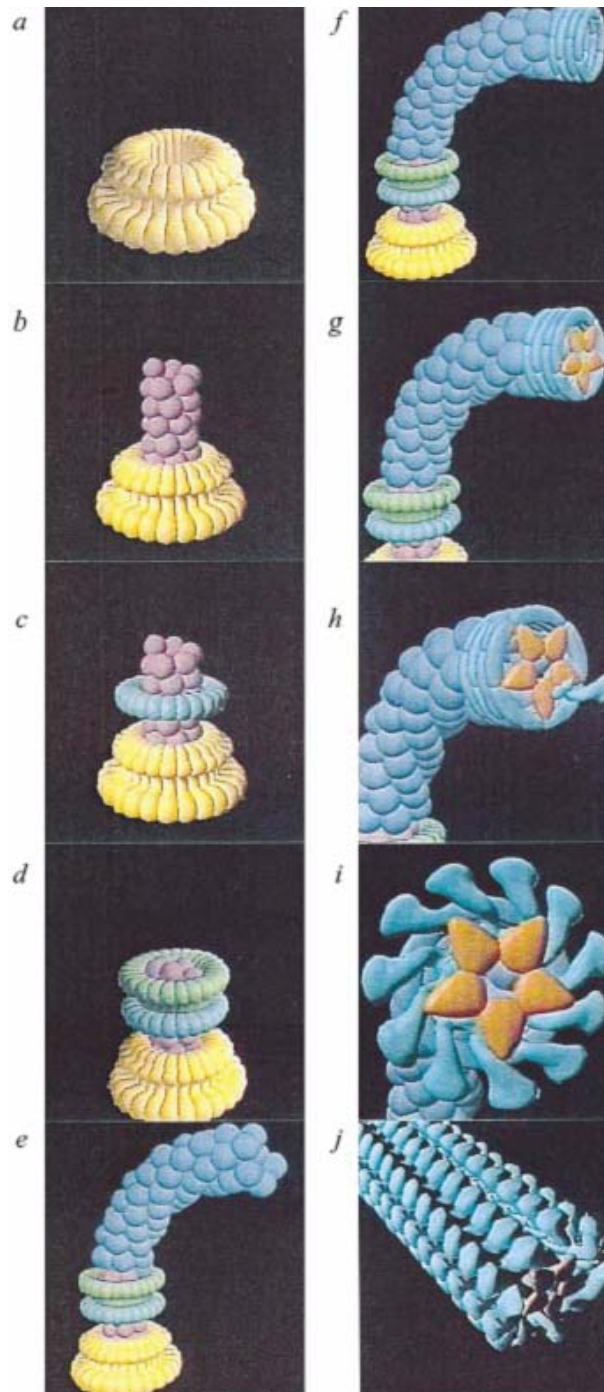


Figure 1-4 Outward assembly pathway of the flagellum. It starts from (a) the FliF ring, followed by sequential addition of (b) the rod, (c) P-ring, (d) L-ring, (e) hook, (f) HAP1 and HAP3, (g) HAP2, (h) a flagellin subunit, (i) 10 flagellin subunits, and (j) filament formation (figure adapted from Namba and Vonderviszt 1997).

1.2.2.1 Bacterial Flagellin

The flagellar filament is generally composed of over 10 000 copies of a single protein, flagellin, with a molecular mass varying from 25 to 60 kDa depending on the species. Some species may have more than one flagellin but the proteins are usually closely related (Berry and Armitage 1999).

Flagellin consists of four linearly connected domains labelled D0, D1, D2 and D3, which are arranged from the inside to outside of the filament (**Figure 1-5 a**). The N-terminal chain starts from D0, going through D1, D2 and reaches D3, and then comes back through D2 and D1, and the C-terminal chain ends in D0. Although all three domain connections are formed by pairs of short antiparallel chains, the one that connects domains D0 and D1 is longer than the other two, and therefore it is called the spoke region. The overall shape of flagellin looks like an upper case Greek gamma (Γ) with a vertical dimension of about 14.0 nm and a horizontal dimension of about 11.0 nm.

Flagellin has been found to be very susceptible to even a mild proteolytic treatment. When digested with trypsin or subtilisin, both termini of flagellin from *Salmonella typhimurium* (51.5 kDa) were found to be quickly degraded, resulting in a compact metastable product of 40 kDa. In contrast, the central region of the molecule is quite stable against proteolysis, probably because it is composed of compact structural units (Namba and Vonderviszt 1997).

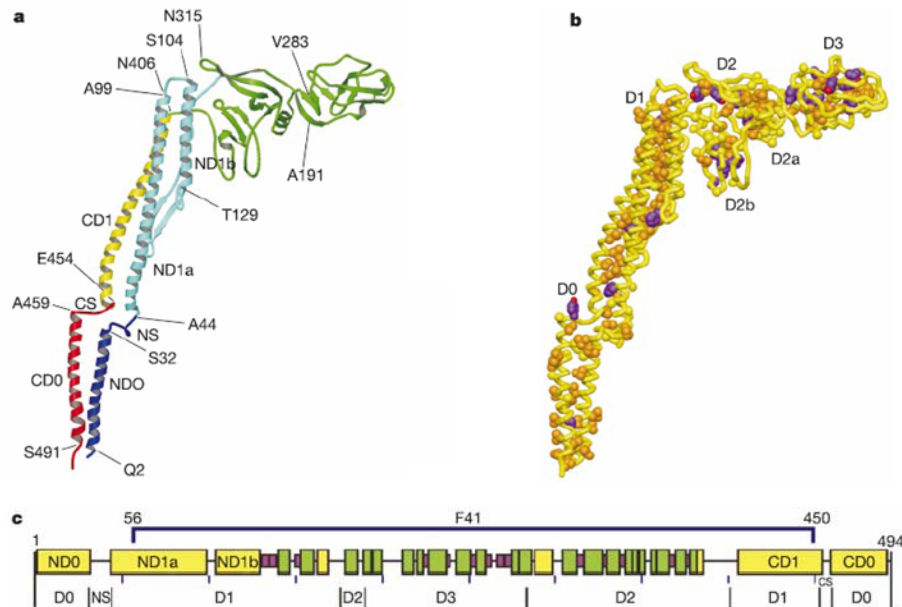


Figure 1-5 The C α backbone trace, hydrophobic side-chain distribution and structural information of flagellin. (a), Diagram of the C α backbone. The chain is coloured as follows: residues 1–44, blue; 44–179, cyan; 179–406, green; 406–454, yellow; 454–494, red. (b), Distribution of hydrophobic side chains, mainly showing hydrophobic cores that define domains D0, D1, D2a, D2b and D3. Side-chain atoms are coloured as follows: Ala and Met, yellow; Leu, Ile and Val, orange; Phe, Tyr and Pro, purple (carbon) and red (oxygen). (c), Position and region of various structural features in the amino acid sequence of flagellin. Shown are, from top to bottom: the secondary structure distribution with α -helix in yellow, β -structure in green and β -turn in purple; the well conserved amino-acid sequence in red and variable region in violet (figure adapted from Yonekura *et al.* 2003).

1.2.2.2 Intersubunit Interactions in the Filament

The filament is a tubular structure composed of 11 protofilaments (**Figure 1-6**) with their lateral disposition staggered axially by about half a subunit, and therefore approximately 5.5 subunits exist in one turn of the one-start helical path that goes through all the subunits (Yonekura *et al.* 2002).

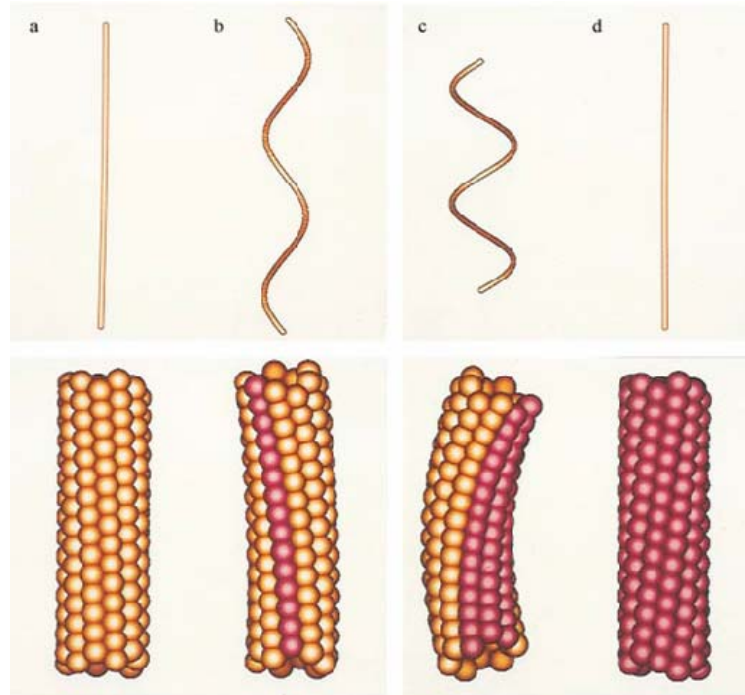


Figure 1-6 Polymorphic model of the filament. The top panel shows morphology of the filaments and the bottom panel shows the subunit arrangements within a short segment. The filaments are named: (a) L-type straight, (b) normal, (c) curly and (d) R-type straight. The two subunit colours represent the two distinct states of flagellin. The supercoil in (b) is left-handed and that in (c) is right-handed (figure adapted from Namba and Vonderviszt 1997).

The subunits pack in two different ways: The subunits in ‘short’ protofilaments (R-type) are closer together than the subunits in ‘long’ protofilaments (L-type) (**Figure 1-6, Figure 1-7**). R and L refer to the direction of twist. If both types are present at the same time, the filament has curvature as well as twist and is helical, with the short protofilaments running along the inside of the helix (Berg 2003). Mechanical strain energy is minimized when short protofilaments are next to short protofilaments and long protofilaments are next to long protofilaments, leading to 12 possible conformations, 2 straight (all short or all long) and 10 helical (Berg 2003). Filaments can be made to switch between these different helical

conformations, which is driven by motor switching or by changes in either the viscous forces on the filament or pH (Berry and Armitage 1999).

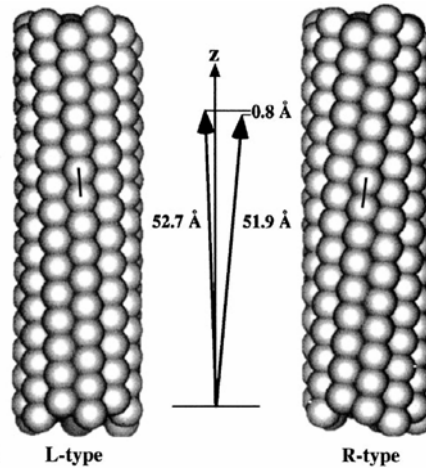


Figure 1-7 The surface lattice of L- and R-type straight flagellar filaments. The spacing between flagellin subunits along an 11-start helix (a protofilament) of the R-type is 0.08 nm less than between corresponding subunits of the L-type. L and R refer to the handedness of the filament twist. The distances are measured at a radius of 4.5 nm and are shown magnified in the middle of the drawing (figure adapted from Berg 2003).

The structure of the filament has been analyzed at around 10 Å resolution by electron cryomicroscopy and helical image reconstruction (Mimori *et al.* 1995; Morgan *et al.* 1995). The density map shows a densely packed core region out to a radius of about 60 Å, a central channel with a diameter of about 30 Å, and well-resolved outer parts that slew out to a radius of 115 Å. There are two radial regions of high density in the core region, one from 15 to 30 Å (Domain D0) and the other from 35 to 60 Å (Domain D1). These two regions form a concentric double tubular structure, and the inner and outer tubes are connected by radial spoke-like densities. The outer part also consists of two domains: domain D2 has

the shape of a vertical column; domain D3 is a projection that extends out from the upper part of the vertical column. Domains D2 and D3 consist of mainly β -strands and domain D1 contains three long α -helices paired with a β -hairpin (Yonekura *et al.* 2002). The subunits are closely packed in the core region and it is not possible to determine the subunit boundary there. In the outer region, however, the subunits are well separated from each other (Namba and Vonderviszt 1997).

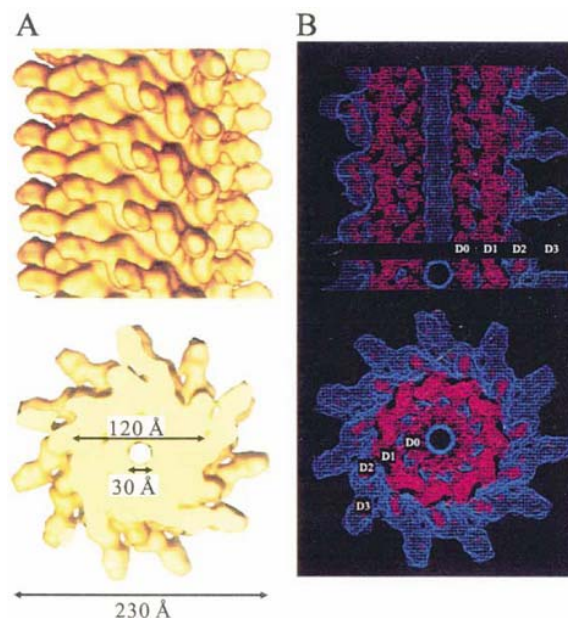


Figure 1-8 Three-dimensional density map of the flagellar filament (R-type straight filament), calculated by including data up to 9 Å. (A) Solid surface representation of a side view with the distal end up (upper panel) and the end-on view from the proximal end (lower panel). (B) Wire frame representation of a 50 Å thick cross section and a 30 Å thick longitudinal section. The directions of views are the same as in (A). Counter lines in blue represent approximately the correct volume of the filament, and those in red show a density level twice as high as that in blue (figure adapted from Yonekura *et al.* 2002).

Domains D0 and D1 make intimate intersubunit interactions, both axially and laterally. Thus, the N- and C-terminal chains of flagellin are essential for filament assembly.

Most of the intersubunit interactions found within the outer tube are polar–polar or charge–polar, and contributions of hydrophobic interactions are relatively small, whereas those found within the inner tube and between the inner and outer tubes are mostly hydrophobic, contributing to the high stability of the filament structure.

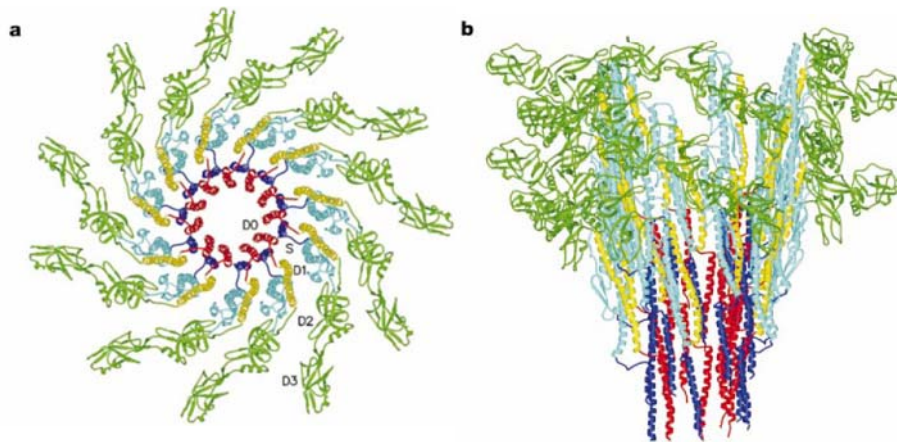


Figure 1-9 Ribbon diagram of the C α backbone of the filament model in stereo view. (a), End-on view from the distal end of the filament. Eleven subunits are displayed. (b), Side view from outside the filament. Three protofilaments on the far side have been removed for clarity. Top and bottom of the side view image correspond to the distal and proximal ends of the filament, respectively. The chain is colour coded as in **Figure 1-5** (a) (figure adapted from Yonekura *et al.* 2003).

1.2.2.3 Transformations of Flagellar Filaments in vitro

For chemotaxis and thermotaxis, the swimming pattern of bacteria such as *Salmonella* and *Escherichia coli* alternates between ‘run’ and ‘tumble’; a run lasts

for a few seconds and a tumble for a fraction of second. During a run, the motor rotates anticlockwise (as it is viewed from outside the cell), and several flagellar filaments with a left-handed helical shape form a bundle and propel the cell. A tumble is caused by quick reversal of the motor to clockwise rotation (Larsen *et al.* 1974), which produces a twisting force that transforms the left-handed helical form of the filament into a right-handed one (Macnab *et al.* 1977; Turner *et al.* 2000), causing the bundle to fall apart rapidly. The separated filaments act in an uncoordinated way to generate forces that change the orientation of the cell. Thus, the structure of the flagellar filament and its dynamic properties have an essential role in bacterial taxis.

Reconstituted *Salmonella* flagellar filaments were found by dark field light microscopy to undergo reversible transformations at both acidic and alkaline pH (Kamiya and Asakura 1976). Flagellar filaments from SJ670 strain are left-handed helices with a pitch of 2.3 μm (normal type) at neutral pH. When, however, the pH of the solution is lowered to 4.7, they are discontinuously transformed into closed-coils with a pitch of 0.5 μm and a diameter of 1.2 μm , and a further lowering of the pH converts these coiled flagellar filaments into so-called curly ones, which are right-handed helices with a pitch of 1.1 μm . When the pH was increased from 7 to 12.5, flagellar filaments from strain SJ670 were found to rapidly transform from the normal type to a left-handed close-coil (coiled type) or to two types of right-handed helices with a pitch of 1.0 or 0.9 μm . Kamiya and Asakura concluded that the pH is an important factor in the control of flagellar transformation.

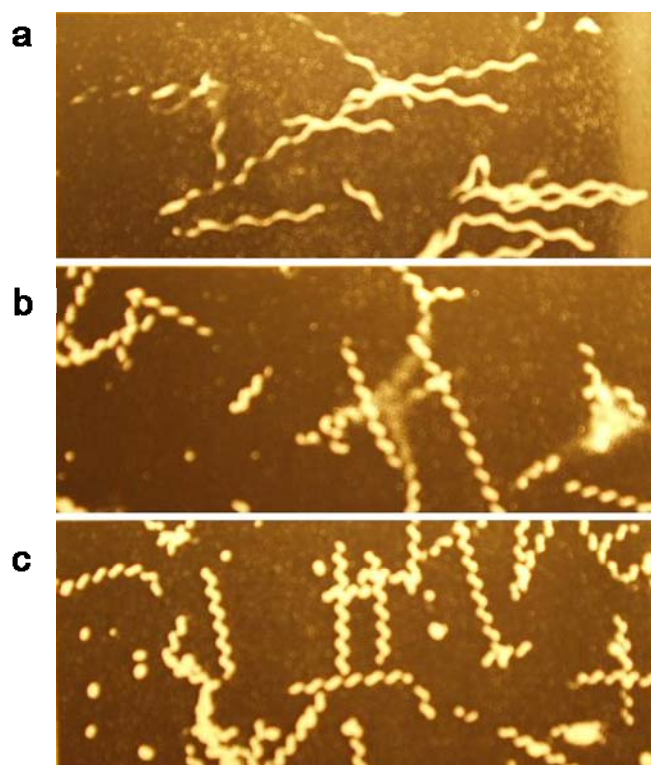


Figure 1-10 Dark field light micrographs of *Salmonella* flagellar filaments. (a) Normal form found at pH 7.0 (1mM potassium phosphate buffer and 100 mM KCl) with pitch = 2.3 μm ; (b) curly form at pH 4.1 (0.1 M NaCl, 1 mM acetic acid and 1mM sodium acetate, pH value was adjusted by the addition of 1 M HCl or 1 M NaOH) with pitch = 1.1 μm ; (c) curly form at pH 12.0 (100 mM KCl, pH value was adjusted by the addition of 1M KOH or 1 M HCl) with pitch = 1.0 μm (figure adapted from Kamiya and Asakura 1976).

1.2.3 Applications of Bacterial Flagellar Filaments

The flagellar filaments can be naturally produced by bacteria very quickly (see section 2.2.1). They can be easily removed from the cells by mechanical shearing. The flagellin has conserved regions at the N- and C-termini, that are required for anchoring of the flagellin into the nanotubular structure. However, the central region which is partially displayed on the filament surface is variable. The single gene encoding flagellin can be easily engineered to allow the surface display of

inserted epitopes along the length of the filament. Woods and co-workers (2007) functionalized *Escherichia coli* FliC flagellin to form tailored nanotubes capable of binding single types or pairs of ligands, including divalent cations, fluorescent antibodies, or biotin-avidin-linked moieties such as ferritins.

Kumara and co-workers (2006) produced cysteine-containing FliTrx to form bundles of functionalized flagellar nanotubes (**Figure 1-11**). Later (2007) they also demonstrated that the peptide loop modified flagella nanotubes could be used as scaffolds for the generation of ordered array of metal nanoparticles or uniform nanotubes (**Figure 1-12**). FliTrx was genetically modified to display designed histidine, arginine-lysine, and aspartic acid-glutamic acid peptide loops on the solvent-accessible outer domain region. The resulting flagellin monomers were self-assembled to obtain flagellar nanotubes in which the peptide loops were 5 nm apart. These flagellar nanotubes were equilibrated with solutions of various metal ions (Co(II), Cu(II), Cd(II), Ag(I), Au(I), and Pd(II)). Controlled reduction of these metal ions yielded ordered arrays of nanoparticules or nanotubes, and in some cases, extensive aggregation resulted in the formation of metal nanotube bundles.

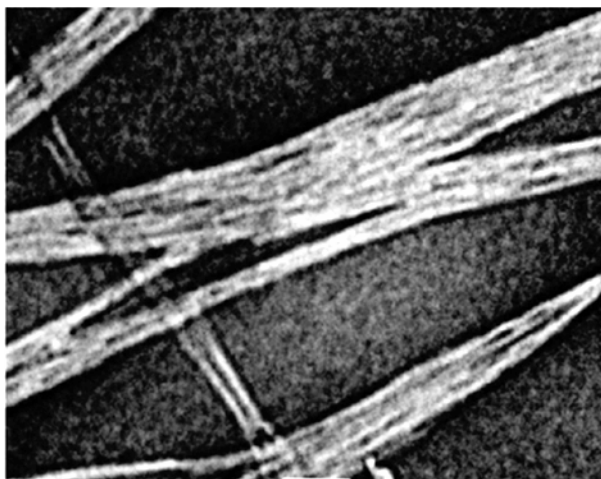


Figure 1-11 TEM images of disulfide cross-linked Cys-loop flagella bundles stained with 2% phosphotungstic acid (pH7.5) (scale bar 100nm) (figure adapted from Kumara *et al.* 2006).

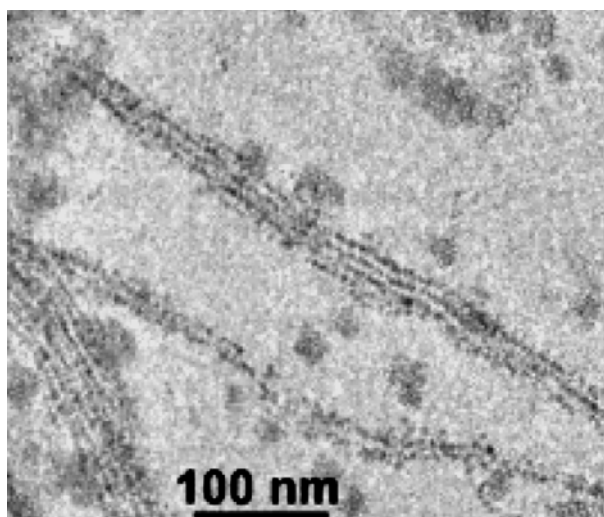


Figure 1-12 TEM images of gold nanoparticles that were synthesized by reduction of Au(I) on a histidine loop peptide flagella scaffold (figure adapted from Kumara *et al.* 2007).

1.3 Amyloid Fibrils

1.3.1 Protein Misfolding

1.3.1.1 Protein Misfolding and Diseases

Amyloid is an insoluble form of protein that results when a normally soluble protein converts via a self-assembly process to form a well-defined fibrillar structure. Amyloid accumulates in a variety of organs including the liver, spleen, and brain. Amyloid fibrils underlie a large family of clinical disorders, and the term amyloidosis is used to describe the clinical conditions with which amyloid is associated (Chiti and Dobson 2006). Examples of amyloidogenic peptides and proteins are listed in **Table 1-1**.

Lysozyme (**Figure 1-13 (a)**), for example, is a 129-amino-acid-residue enzyme which catalyzes hydrolysis of 1,4-beta-linkages between N-acetylmuramic acid and N-acetyl-D-glucosamine residues in peptidoglycan and between N-acetyl-D-glucosamine residues in chitodextrins. The molecular weight of lysozyme is approximately 14.7 kDa. Lysozyme is present in a number of secretions such as saliva, tears and mucus. Large amounts of lysozyme can also be found in egg whites. Lysozyme's catalytic activity is non-specifically targeted to the bacterial cell membranes and related with general non-specific organism defence. Human lysozyme has been shown to form amyloid fibrils in individuals suffering from non-neuropathic systemic amyloidosis (Krebs *et al.* 2000).

Table 1-1 Examples of amyloidogenic peptides and proteins (Table adapted from Dzwolak 2005)

Peptide/protein	Conditions of fibrillation	Properties of the aggregate/fibrils	Remarks
Poly(L-lysine), poly(L-threonine), poly(L-glutamic acid)	65 °C and charge depleting pH (alkalic for K, acidic for E)	From straight, unbranched to short and twisted	Main chain interactions promote aggregation
Poly(L-lysine)+ poly(D-lysine), FF ^a	Mixing at room temp. and alkalic pH Precipitation upon dilution with water	Highly distorted Regular "empty" nanotubes	Racemic fibrils form due to increase in water ΔS Form "nanowires" when filled with Ag atoms
KVVE, KFFE ^a	Long incubation at 37 °C, neutral pH	Bundles resembling in vivo deposits	Charges compensated in the antiparallel alignment
(DPKG) ₂ -(VT) ₃ -S ^a GKGDPKPD-NH ₂ ^a	Spontaneous fibrillation at 25 °C	Sequence-dependent morphologies	Monomers and early fibrils are soluble
Alzheimer β-peptide fragments	Aggregation dependent on pH	CD spectra same as for in vivo deposits	The pH-range parallels in vivo conditions
Oxidized glutathione (GSSG) ^a	Aqueous solutions of DMSO, DMF, MeOH	Thick, 75 nm in diameter fibrils	Network with β-sheet like motive traps solvent
Cyclic octa-peptides alternating D/L amino acids	Precipitation at acidic pH in the presence of cosolvent	Fibrils 1.5 nm thick with an internal diameter 0.7–0.8 nm	Open-ended "nanotubes" with a regular β-sheet like motive
Bovine serum albumin	Sonification at room temperature	Heterogeneous fibrils, 20 nm thick	Possible role of free radicals in the aggregation
Antifreeze protein of winter flounder	Repetitive freezing–thawing cycles.	Short, 5 nm in diameter	Ice-binding may trigger the fibrillation
C11A/C14A mut. cytochrome c ₅₅₂	Incubation at 25 °C, neutral pH	Typical fibrils are 6–13 nm thick	C11A/C14A substitution destabilizes <i>holo</i> -protein
Horse <i>apo</i> -myoglobin	A day-long incubation at 65 °C, pH 9	Fibrils are unstable above 65 °C	Amyloidogenesis requires complete unfolding
Bovine insulin	Hours-long incubation at 65 °C, pH 2	Fibrils associated in spherulites	Characteristic optical properties
Tetramerization domain p53 protein	Gradual heating up to 95 °C, pH 4	Straight and curly forms 1–2 nm thick	Amyloid disassembles above pH 8.5
Transthyretin	3.5 kbar pressure, at 37 °C, neutral pH	Formed after depressurization	Non-native aggregation-prone tetramers formed
Hen egg white lysozyme	2–5 M guanidine HCl, 50 °C, neutral pH	Twisted, approx. 13 nm thick	Denaturant concentration within range of 2 and 5 M
Yeast prion protein Ure2	Shaking at 37 °C, pH 8	Straight fibrils, 4–8 nm in height (AFM)	Highly heterogeneous samples
Prion proteins: Human PrP(90-231), Mouse PrP(89-230)	Shaking at 37 °C, at pH ranging from 3.7 to 7.2	Fibrils at neutral pH shorter than those formed at pH 3.7	Fibrillation enhanced by homologous seeding (Hu → Hu, Mo → Mo)

^a Peptide names decode amino acid sequence according to the one-letter system.

Beta2-microglobulin (**Figure 1-13 (b)**) which belongs to the immunoglobulin superfamily, is known to aggregate into amyloid that deposit at joint spaces in patients on long-term hemodialysis, a disease known as dialysis-related amyloidosis (DRA) (Smith and Radford 2001; Manning *et al.* 2003).

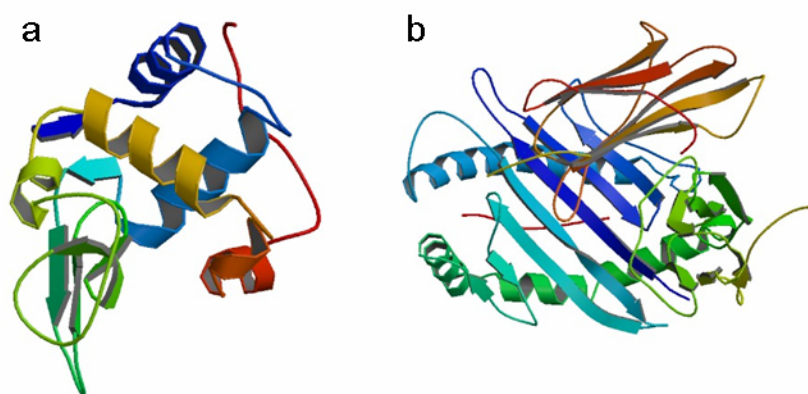


Figure 1-13 Stereo ribbon diagram of the structure of (a) lysozyme (b) beta2-microglobulin (www.pdb.org ID: 133l. Harata *et al.* 1993; ID: 1a1m. Smith *et al.* 1997).

1.3.1.2 Energy Landscape of Protein Folding

A typical energy landscape diagram of protein folding is displayed in **Figure 1-14**. The unfolded polypeptide chain gradually progress through various levels of organization that ultimately lead to the energetically stable folded native state (Dobson *et al.*, 1998). The nature of this energy landscape is influenced by features such as the protein sequence and the conditions under which folding occurs. Therefore, changing the conditions under which a protein folds, as in a disease state or as in the laboratory, can result in local energy minima; and an energy barrier may be created that halts continued folding towards the native state.

The increasing populations of these partially folded proteins may lead to a self-association process whereby they become “trapped” in an aggregated, non-native form.

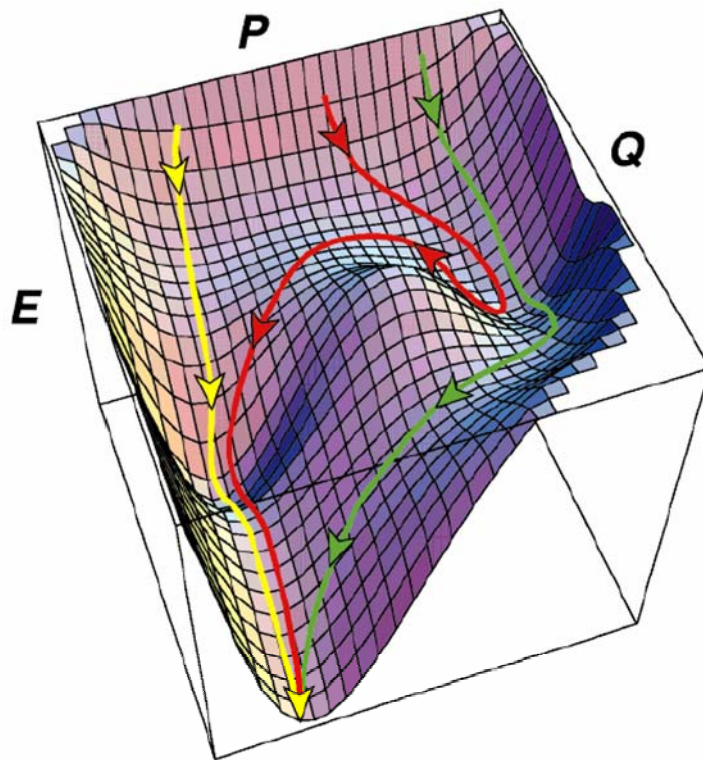


Figure 1-14 The estimated energy landscape diagram based on data for the folding of lysozyme. Several possible folding pathways are shown: a fast folding route (yellow), a slow folding route involving an energy barrier (green), and a slow folding route that returns to a less folded state and then joins the fast folding route (red). E refers to energy, P is a measure of the available conformational space, and Q is the fraction of native contacts (figure adapted from Dobson *et al.* 1998).

The formation of amyloid fibrils reflects the conformational struggle of polypeptide chains to reduce their surface accessible area, to saturate hydrogen

bonding, and to reach an alternative non-native free energy minimum (Dobson *et al.* 1998).

1.3.1.3 Structure of Amyloid Fibrils

Despite the diverse range of proteins that are involved in amyloid related diseases, all of which have unique native folding states, they are found to have extremely similar final morphologies in their misfolding states. The generic structure of amyloid fibrils has been revealed in some detail; however, the exact molecular conformation and supramolecular organization still needs to be determined. Perutz and co-workers (2001) proposed that amyloid fibrils are nanotubes with central water-filled cavity.

A generally accepted fibrilization pathway is as follows: first, the globular proteins partially unfold under certain conditions and self-assemble into protofilaments; the protofilaments then intertwine with each other into mature fibrils (Ban *et al.* 2006; Chamberlain *et al.* 2000; Khurana *et al.* 2003; Makin *et al.* 2005).

In laboratories, amyloid fibrils are usually produced by exposing proteins to mildly denaturing conditions, such as low pH or elevated temperatures. The exposure to denaturing conditions allows the peptide backbone to be accessible to form the interchain hydrogen bonds associated with amyloid fibrils (Dobson *et al.* 1998).

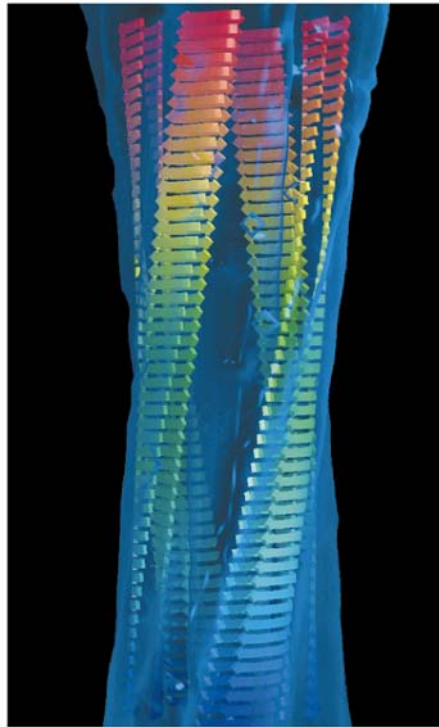


Figure 1-15 A molecular model of an amyloid fibril grown from an SH3 domain. The fibril consists of four protofilaments that twist around one another to form a hollow tube. Each protofilament is assembled through β domain (figure adapted from Dobson 1999).

Based on AFM analysis of the morphology of fibrillar species formed during amyloid fibrillization processes, Khurana and co-workers (2003) proposed a general model for the assembly of protein fibrils (**Figure 1-16**). Insulin fibrils were formed *in vitro* by stirring the protein in an acid solution (pH 1.6). Under those conditions, insulin fibrils were found to reach maturity after 4 hours of incubation. During the fibrillization process, protofilaments (1.2 ± 0.3 nm in diameter) and protofibrils (1.9 ± 0.3 nm in diameter) were observed. Two sizes of mature fibrils were also observed: a smaller fibril of 3.0 ± 0.4 nm in diameter, and a larger fibril of 4.8 ± 0.4 nm in diameter, which they identified as types I and II fibrils, respectively. They suggested that protofilament pairs intertwine with each other to

form protofibrils, and two protofibrils then intertwine to form a type I fibril. A type II fibril is formed by winding of two type I fibrils.

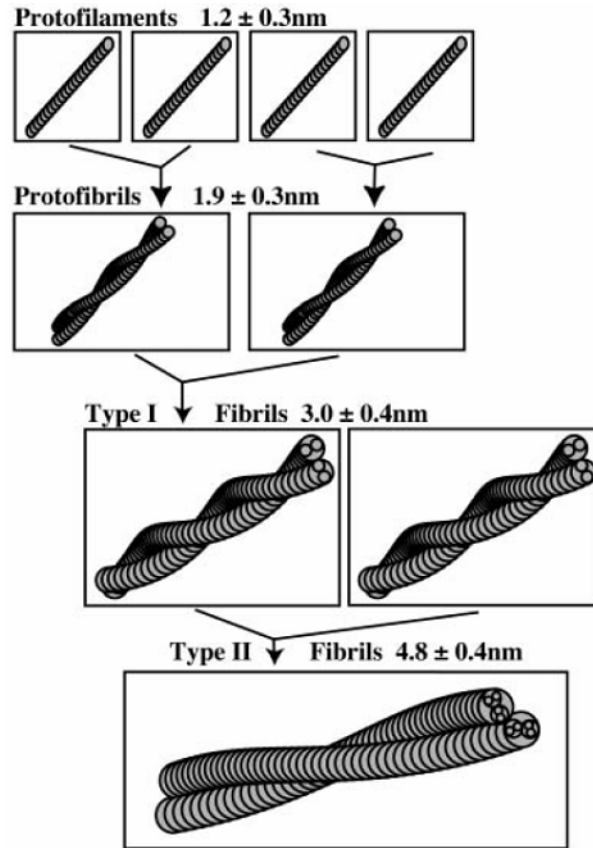


Figure 1-16 Khurana’s model for the hierarchical assembly of insulin into amyloid fibrils. Protofilament pairs wind together to form protofibrils, and two protofibrils wind to form a type I fibril. Type II fibrils are the result of winding of type I fibrils (figure adapted from Khurana 2003).

Another AFM study carried out by Jansen and co-workers (2005) on insulin aggregates suggested that, in addition to the hierarchical pathway of fibrilization, there was an alternative self-assembly route leading to insulin fibrils which involved the lateral interaction of early, prefibrillar forms with protofilaments.

The nature of multipathway fibrilization resulted in a more complex morphological variety.

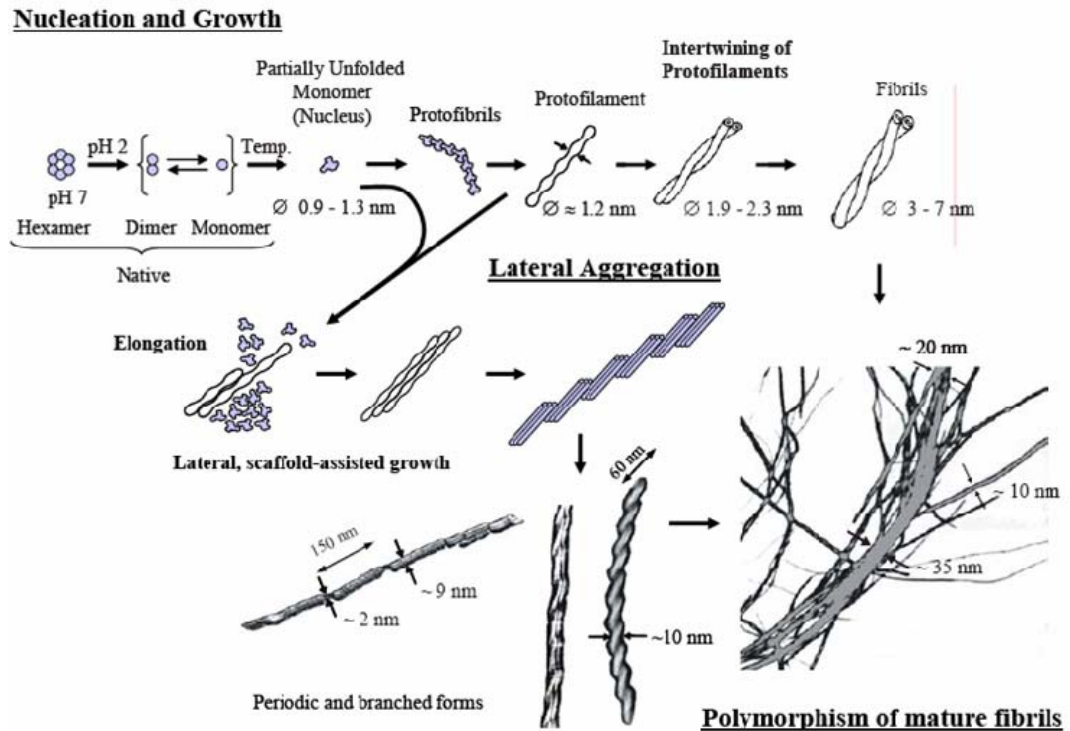


Figure 1-17 A general scheme of the multipathway fibrilization of insulin. Insulin hexamers undergo monomerization at low pH and then form protofilaments which then intertwine with each other to form mature fibrils. The lateral interaction of early, prefibrillar forms with protofilaments, followed by the lateral association of protofilaments, is an alternative self-assembly route. Under the given conditions, insulin fibrilization proceeds through both pathways (figure adapted from Jansen *et al.* 2005).

An interesting circular morphology of insulin amyloid formed under high hydrostatic pressure was discovered by Jansen and co-workers (2004) (**Figure 1-18**). While high pressure was found to prevent insulin aggregation, the protein nevertheless was able to slowly form amyloid with this unprecedented circular

morphology. Jansen suggested that at high pressure, the fibril tends to bend in one direction throughout the elongation process.

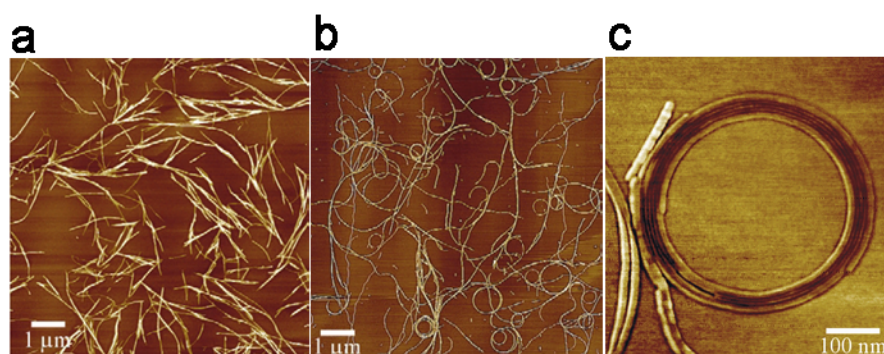


Figure 1-18 AFM height images of insulin amyloid. (a) Control sample, 0.5% (w/w) of bovine insulin in water, pH adjusted to 1.9, was kept at ambient pressure and 60 °C for 21 hours. (b) Insulin sample was kept at 60 °C for 20 hours after increasing the pressure to 1500 bar and kept for one hour after pressure-release. (c) High-resolution AFM images of the circular amyloid reveal its ultrastructural features (figure adapted from Jansen 2004).

Similar circular forms of insulin fibrils (**Figure 1-19**) were observed by Grudzielanek and co-workers (2005) when they were studying the solvational effects on the unfolding, aggregation and amyloidogenesis of insulin. Ethanol acts as an aggregation enhancer at low concentrations and an inhibitor at higher concentrations. The addition of concentrations as low as 5% (w/w) of ethanol was found to trigger the appearance of bent and circular fibrils, the diameter of which was typically 750-800 nm. The amount of circular forms reduced in 20% (w/w) ethanol and vanished completely at 40% (w/w) ethanol.

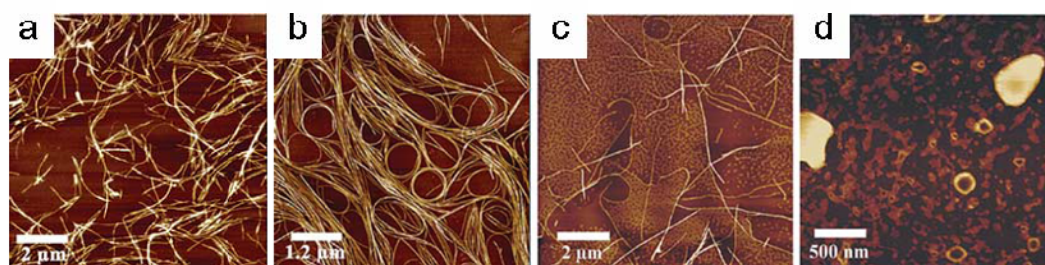


Figure 1-19 AFM images of 0.1% (w/w) insulin, aggregated at 60 °C for six days in: (a) water; (b) 5% (w/w) EtOH; (c) 20% (w/w) EtOH; (d) 40% (w/w) EtOH (figure adapted from Grudzielanek 2005).

Dzwolak (2006) reviewed the results of tuning amyloidogenic conformations through cosolvents and hydrostatic pressure, and proposed a hypothetical model of hyperbaric and solvational control of insulin amyloid polymorphism. He pointed out that although both native insulin and insulin amyloid are resistant to high pressure and the influence of cosolvents, the intermediate aggregation-prone conformations are susceptible to either condition. A lower void volume conformation was proposed to be favoured under high pressure. The persistent bending of a fibril towards one direction during its elongation to form circular morphology was proposed to suggest an anisotropic distribution of cavities within the ambient fibril.

1.3.2 Applications of Amyloid Fibrils

The well-ordered structure of amyloid fibrils confers stability at extremes of pH, temperature, or pressure; fibrillar structure is typically preserved in both aqueous and organic solvents. Amyloid fibrils are also resistant to proteolysis and dehydration (Gras 2007a; 2007b). All of these favourable properties, associated with the versatile modifiability of the peptides/polypeptides by chemically

introducing functional groups, enable amyloid fibrils to hold a great potential as biomaterials for nanotechnology and bionanotechnology.

Before commercial applications of amyloid fibrils in nanotechnology and bionanotechnology can be fully realised, a high degree of control of their properties needs to be achieved, which requires the further study of the relationship between the functionalization of the peptides/polypeptides and the characteristics of amyloid fibrils (Waterhouse and Gerrard 2004). Meanwhile, some recent attempts to exploit amyloid fibrils as biomaterials have been promising.

Scheibel and co-workers (2003) reported the use of self-assembling fibres to construct nanowire elements. Self-assembly of a prion determinant from *Saccharomyces cerevisiae*, the N-terminal and middle region (NM) of Sup35p, produced 10-nm-wide protein fibres. These NM fibres were stable under a wide variety of harsh physical conditions; and their length could be roughly controlled by assembly conditions in the range of 60 nm to several hundred micrometers. A genetically modified NM variant that presented reactive, surface-accessible cysteine residues was used to covalently link NM fibres to colloidal gold particles. These fibres were placed across gold electrodes, and additional metal was deposited by highly specific chemical enhancement of the colloidal gold by reductive deposition of metallic silver and gold from salts. The resulting silver and gold wires were ~ 100 nm wide (**Figure 1-20**). These biotemplated metal wires demonstrated the conductive properties of a solid metal wire, such as low resistance and ohmic behaviour (**Figure 1-21**). With such materials it should be

possible to harness the extraordinary diversity and specificity of protein functions to nanoscale electrical circuitry.

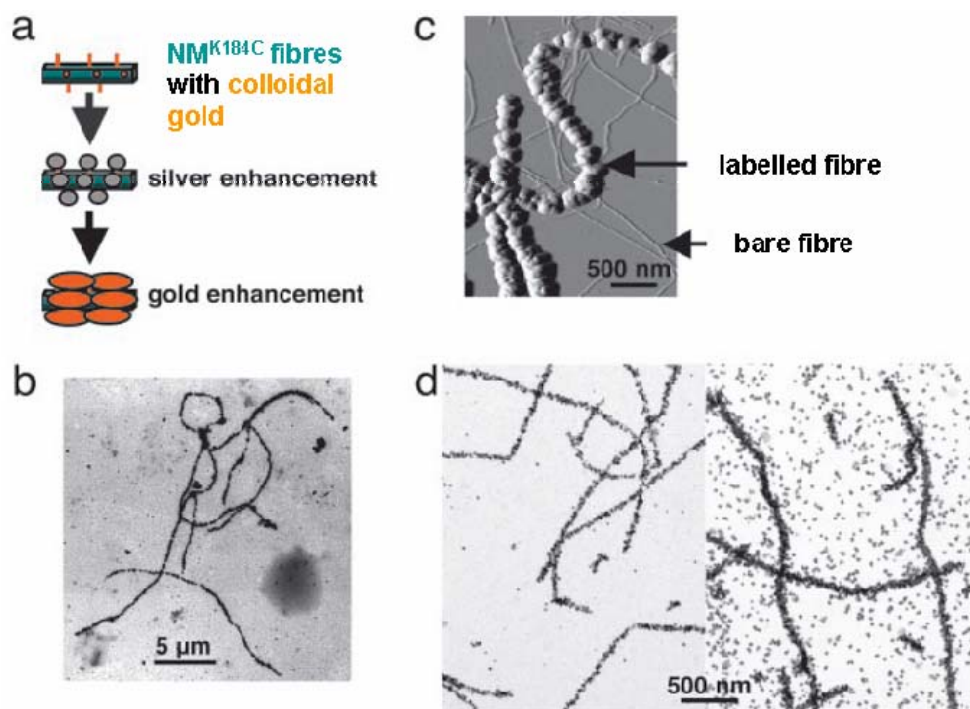


Figure 1-20 Gold and silver enhancement of NM fibres. (a) Illustration of silver and gold enhancements. Monomaleimido nanogold was covalently cross-linked to NM^{K184C} fibres and then fibres were gold-toned by enhancing with LI Silver and GoldEnhance LM. (b) TEM image of gold-toned fibres. (c) AFM height image of gold toned fibres with significant increase in height compared to bare fibres. (d) AFM height images of (left) gold-labelled fibres on Si₃N₄ subjected to 3 min of silver enhancement and 5 min of gold enhancement, leading to a fibre diameter of 50 ± 5 nm, and (right) fibres after 5 min of silver enhancement and 5 min of gold enhancement, leading to a fibre diameter of 100 ± 7 nm (Figure adapted from Scheibel *et al.* 2003).

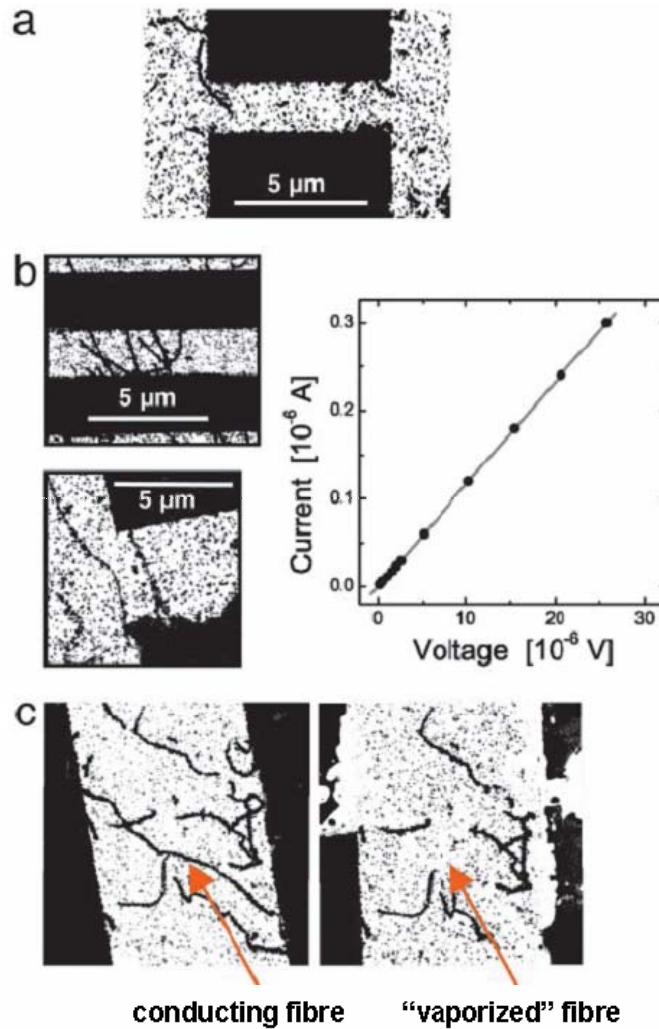


Figure 1-21 Electrical behavior of NM-templated metallic fibres. TEM images of gold- and gold-toned fibres randomly deposited on patterned electrodes. (a) Gold nanowires that did not bridge the gap between two electrodes did not conduct. (b) Gold nanowires that bridged the gap between two electrodes (left) exhibit linear I–V curves (right), demonstrating ohmic conductivity with low resistance of $R = 86 \Omega$ (the same for each). Such ohmic response is indicative of continuous, metallic connections across the sample. (c) In some experiments, after ramping up the voltage, reversing the scan direction no longer showed conductivity. Imaging revealed that the conducting nanowires were vaporized. Before (left) and after (right) conductivity measurement (figure adapted from Scheibel *et al.* 2003).

1.3.3 Diphenylalanine Nanotubes (FF Nanotubes)

1.3.3.1 Discovery and Synthesis of Diphenylalanine Nanotubes

By comparing a number of structurally unrelated short functional fragments of amyloid-related polypeptides, Gazit (2002) noted a remarkable occurrence of aromatic residues. In many areas of chemistry and biochemistry, especially in self-assembly and molecular recognition, the attractive non-bonded interactions between planar aromatic rings, which are referred to as π - π interactions or π -stacking, play a central role. Gazit then speculated that the π - π interactions may provide energetic contribution as well as order and directionality in the self-assembly of amyloid structures. Bearing this in mind, in the spirit of looking for the simplest building blocks of bionanomaterials, Reches and Gazit (2003) discovered the self-assembly of diphenylalanine peptide (NH_2 -L-Phe-L-Phe-COOH, FF see **Figure 1-22**) into discrete and stiff nanotubes. They dissolved diphenylalanine peptide in 1,1,1,3,3,3-hexafluoro-2-propanol (HFIP) at high concentrations ($\geq 100\text{mg/mL}$) and then diluted into a aqueous solution with a final μM concentration range; a rapid assembly was observed. A stable analogue of the nanotubes composed of D-isomer amino acids (NH_2 -D-Phe-D-Phe-COOH) could also be prepared; but unlike those prepared from the L-isomer, these nanotubes were stable to proteolytic degradation.

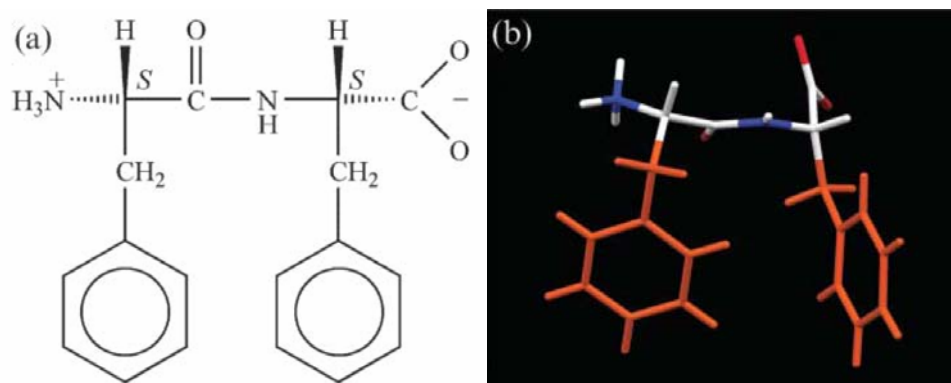


Figure 1-22 (a) Schematic structure of FF. (b) The molecular structure of FF from the single crystal structure determination. Side-chain atoms are shown in orange (figure adapted from Gorbitz 2001).

FF nanotubes synthesized by the Reches and Gazit (2003) method, were several micrometers in length and 50 to 300 nm in diameter. Song and co-workers reported (2004) another method which simplified the synthesis and made it more environmentally benign by omitting HFIP. In a typical synthesis, 10 mg of lyophilized peptide ($\text{HN}_2\text{-D-Phe-D-Phe-COOH}$) was dissolved in 5 mL water at 65 °C, and the sample equilibrated for 30 min and then gradually cooled to room temperature. Scanning Electron Microscopy (SEM) images showed that the nanotubes obtained using this procedure were 100 nm to 2 μm in diameter and could exceed 100 μm in length. Interestingly, when 0.1 mL of the nanotube mixture was diluted by adding 0.1 mL of water, vesicles were observed in addition to the nanotubes. Song suggested that these results indicated that the concentration of the peptide was a key factor in the formation of the nanotubes and that the HFIP was not critical for the self-assembly process.

1.3.3.2 Structures and Properties of diphenylalanine Nanotubes

Transmission Electron Microscopy (TEM) analysis with negative staining indicated that the structures of FF nanotubes were well-ordered elongated assemblies with no branching. Almost no amorphous aggregates were observed (<1%), which is in contrast to other peptide assemblies (such as amyloid fibrils) in which a mixture of ordered and aggregated structures are frequently observed.

A tentative model for the construction of FF nanotubes was proposed by Görbitz in 2006 (**Figure 1-23**). The exact nature of the inner surface shown in **Figure 1-23** is not known, it may be mixed hydrophobic/hydrophilic as shown, or entirely hydrophobic. The individual narrow channels proposed within the model are hydrophilic in nature and are able to accommodate guest molecules of some size as well as hydrated metal ions. The aromatic groups generate a striking three-dimensional aromatic stacking arrangement serving as a glue between the hydrogen-bonded cylinders of peptide main chains and promoting fibre formation. It was also proposed that the laminated construction provides exceptional strength for a low-density porous supramolecular network and makes this structure unique among organic materials.

In order to understand the compatibility of FF nanotubes with common lithographic techniques, as well as the long-term durability of nano-devices based on FF nanotubes, Adler-Abramovich and co-workers (2006) investigated the thermal and chemical instability of FF nanotubes. A cold field emission gun (CFEG) high-resolution scanning electron microscope (HRSEM) study showed that FF nanotubes dry-heated up to 150 °C were clearly stable with the same morphology as that observed for untreated FF nanotubes. A significant destruction

of the structures occurred when FF nanotubes were heated to 200-300 °C. They also reported that FF nanotubes were chemically stable in organic solvents such as ethanol, methanol, 2-propanol, acetone, and acetonitrile, as shown by SEM analysis. Using atomic force microscopy (AFM), Sedman and co-workers (2006) showed through in-situ heating studies that FF nanotubes kept its wall integrity at temperatures up to 100 °C. On increasing the temperature further to 150 °C, the nanotubes lost spatial volume. They argued that it was possible that the elevated temperature made the nanotubes more deformable and that they became distorted by the AFM probe during the imaging process. Time-of-flight secondary ion mass spectrometry (ToF-SIMS) analysis suggested that at temperatures at and above 150 °C, the loss in mass and apparent degradation in the nanotubes morphology was due to the loss of phenylalanine.

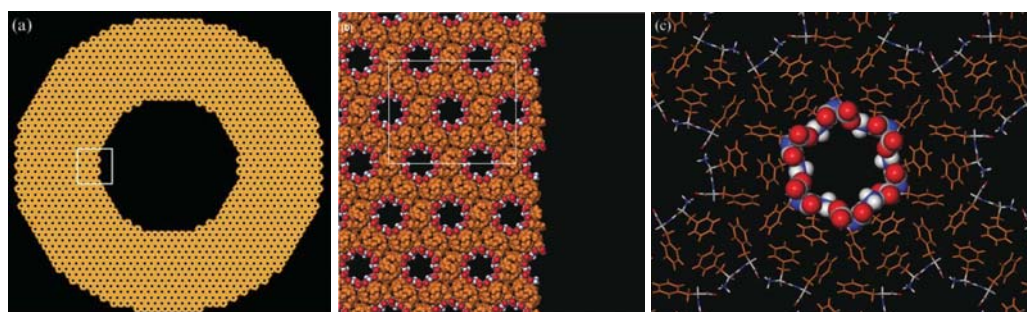


Figure 1-23 Model for the construction of hollow FF fibres. Atoms in the peptide main chains are colored according to atom type, while atoms in the phenylalanine side chains are depicted in orange. Shown in (a) is a tube with a 110 nm outer diameter and a 50 nm inner diameter. This is comparable to the average size obtained by Reches and Gazit (2003), but smaller than that obtained by Song (2004) and in the present investigation. The white square indicates the part enlarged in (b) showing a model of the peptide-channel interface at the inner surface. The rectangle represents the detailed view given in (c) in a capped sticks representation, but with atoms constituting the pore surface in spacefill (figure adapted from Gorbitz 2006).

The elasticity of FF nanotubes was investigated by Kol and co-workers (2005) using the AFM indentation method, and a Young's modulus of ~19 GPa was obtained. In chapter 6 and also in my recent publication (Niu *et al.* 2007), we built on these studies through application of the bending-beam model to AFM images of FF nanotubes suspended across cavities to obtain the Young's modulus and the shear modulus. We were able to utilize this method to study the influence of temperature and relative humidity on the elasticity of FF nanotubes.

Attempts to control the spatial organization of FF nanotubes have also been made. Reches and Gazit (2006) achieved vertical alignment of FF nanotubes by applying the FF peptide monomers dissolved in the organic solvent onto siliconized glass (**Figure 1-24** left). They also achieved horizontal alignment of FF nanotubes by assembling the FF peptide monomers in the presence of ferrofluid and then exposing formed nanotubes to an external magnetic field (**Figure 1-24** right). Hill and co-workers (2007) have also demonstrated that FF nanotubes align in a magnetic field without any additional treatment (**Figure 1-25**). They predicted that most of the magnetic torque on the structure to be generated by the diamagnetic anisotropy of the aromatic rings.

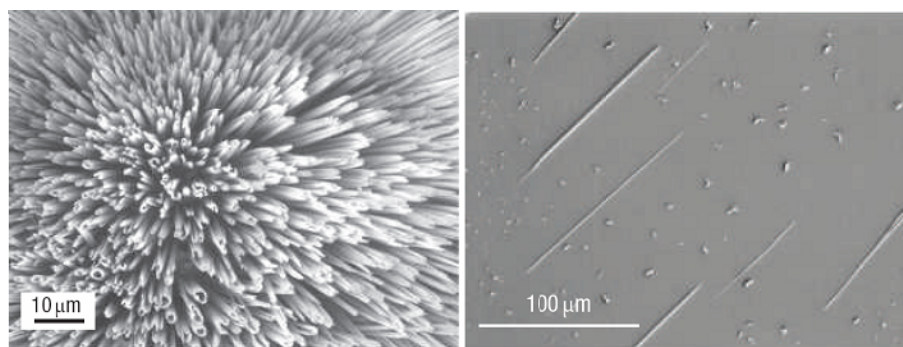


Figure 1-24 SEM images of controlled patterning of aligned diphenylalanine nanotubes. The left picture shows vertically aligned FF nanotubes. The FF peptide monomers were dissolved in the organic solvent and then applied onto siliconized glass. The right picture shows the horizontal arrangement of the aligned FF nanotubes. The FF peptide monomers self-assembled in the presence of ferrofluid and then were exposed to an external magnetic (figure adapted from Reches and Gazit, 2006).

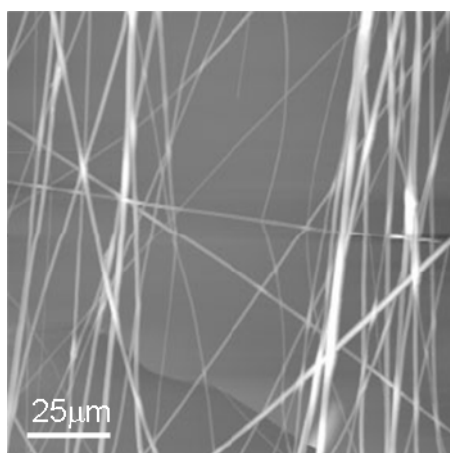


Figure 1-25 AFM topography images of aligned FF nanotubes. The droplet of HFIP–water solution containing FF nanotubes on mica was allowed to evaporate in applied magnetic fields of 12 T. The magnetic field direction lies in the plane of the substrate, along the direction from down to up (figure adapted from Hill *et al.* 2007).

1.3.3.3 Applications of Diphenylalanine Nanotubes

Reduction of ionic silver within FF nanotubes using citrate, followed by enzymatic degradation of the peptide backbone, resulted in the production of discrete silver nanowires with diameter $\sim 20\text{nm}$ (Figure 1-26) (Reches and Gazit 2003). The unique properties of FF nanotubes (see section 1.3.3.2) and their proteolytic lability allow their use as nanoscale molds for the casting of silver nanowires. Reches and Gazit claimed this study also proved that FF nanotubes are indeed hollow and filled with aqueous solution.

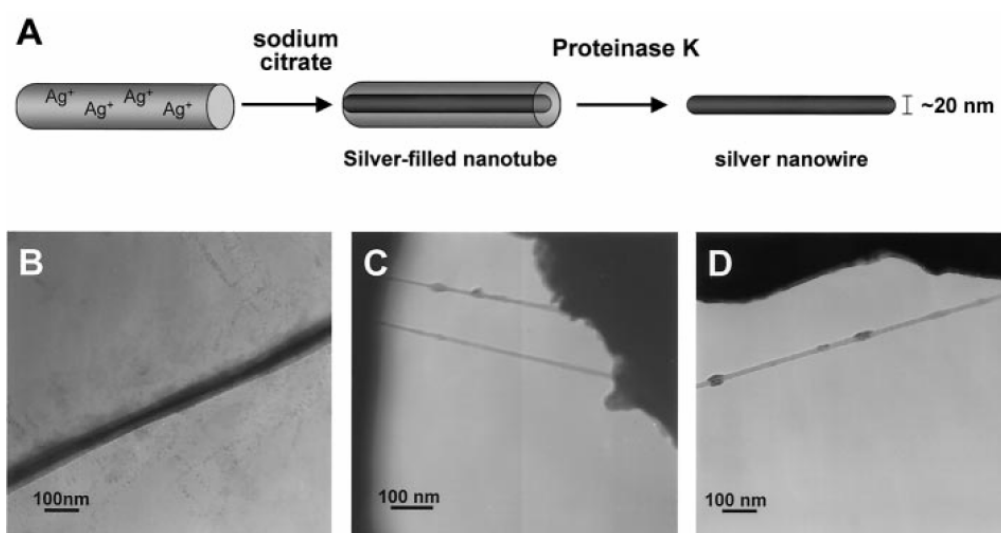


Figure 1-26 Casting of silver nanowires with the peptide nanotubes. (A) The nanowires were formed by the reduction of silver ions within the tubes, followed by enzymatic degradation of the peptide mold. (B) TEM analysis (without staining) of peptide tubes filled with silver nanowires. (C and D) TEM images of silver nanowires that were obtained after the addition of the proteinase K enzyme to the nanotube solution (figure adapted from Reches and Gazit 2003).

Song and co-workers (2004) reported the synthesis of platinum-nanoparticle peptide-nanostructure composites (**Figure 1-27**). Their work suggested that the walls of peptide nanostructures could be porous. The proposed porosity allowed the formation of novel nanocomposites without the disruption of the original nanostructure morphology. The composites prepared in their study has many potential applications, e.g., catalysis; they could also serve as useful scaffolds for the synthesis of other nanomaterials.

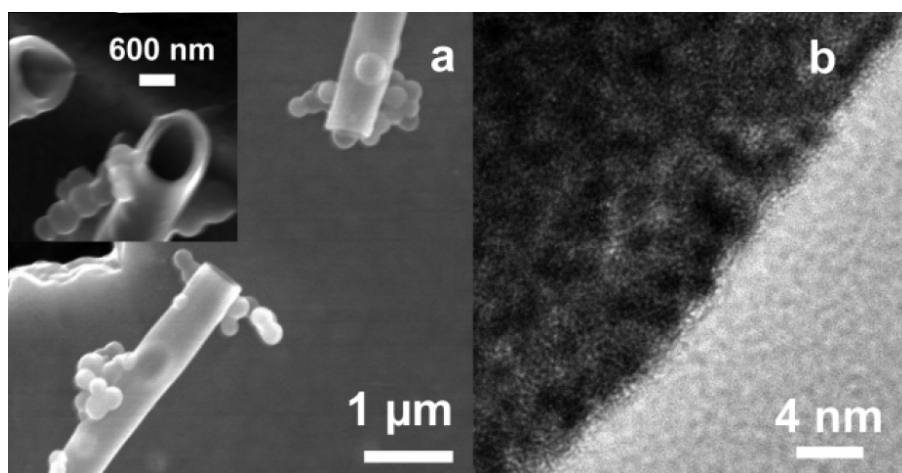


Figure 1-27 SEM images of (a) peptide nanotubes and nanovesicles containing Pt particles (inset: tilted image showing the tubes are hollow) and (b) a high resolution TEM image showing the 2 nm Pt nanoparticles embedded in the wall of a platinum nanotube (figure adapted from Song *et al.* 2004).

Using voltammetric and time-based amperometric techniques, FF nanotube modified graphite electrodes were demonstrated to have improved electrochemical reactivity for the potassium hexacyanoferrate oxidation-reduction reaction over non modified electrodes (Yemini 2004); the FF nanotubes modified gold electrodes, in addition, showed improved sensitivity for hydrogen peroxide

and NADH detection (Yemini 2005). These studies offered novel perspectives for the development of sensors and biosensors.

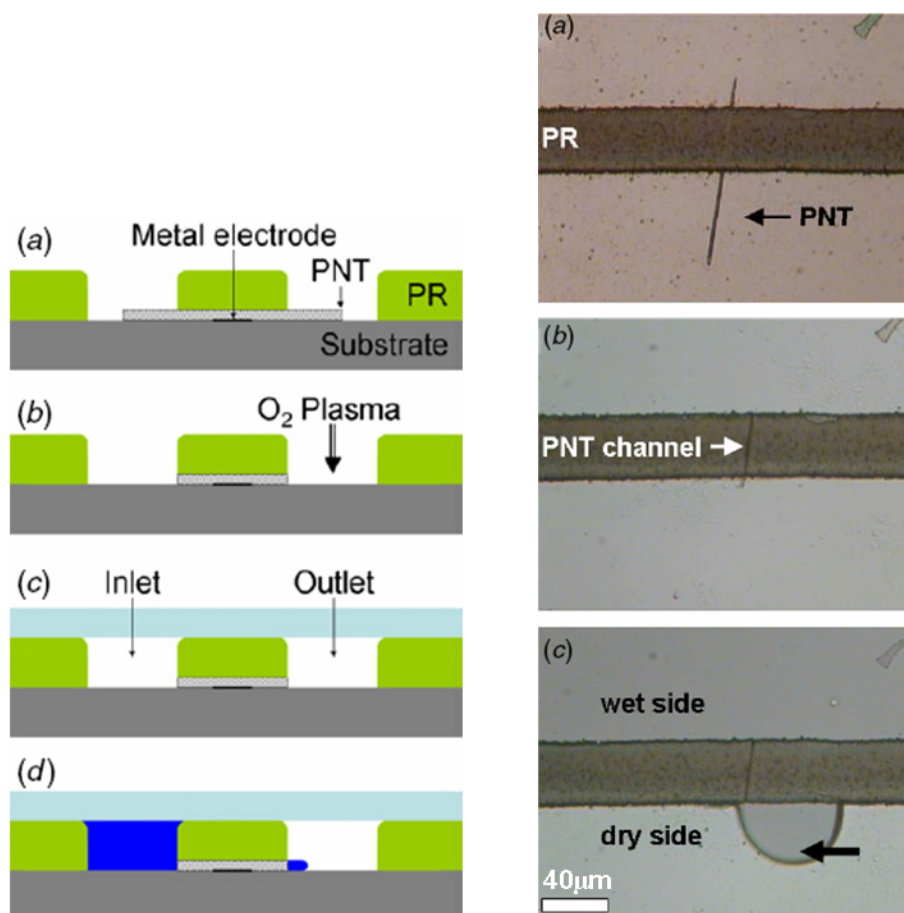


Figure 1-28 Integrating FF nanotubes in micro-fabrication processes. The left picture is a schematic shows the fabrication steps used to create protein nanotube (PNT) based fluidic channel. (a) Interfacing channels are formed using photoresist (PR); (b) unnecessary PNT parts are removed using O₂ plasma treatment and de-ionized water rinsing; (c) sealing the interfacing channel using a thin PDMS cap; (d) flow of solution via the PNT channel. The right picture is an optical image of a nano-fluidic channel using the steps described above. (a) A PNT based nano-fluidic channel before the final fabrication step of the PNT-end trimming; (b) a dry channel ready for use; (c) PBS flow through the nano-fluidic channel (figure adapted from Sopher *et al.* 2007).

Sopher and co-workers (2007) presented an adjusted photo-lithography compatible scheme that allowed the integration of FF nanotubes in micro-fabrication processes; specifically, a scheme for creating nano-fluidic channels using FF nanotubes (**Figure 1-28**).

Dipeptides linked to fluorenylmethoxycarbonyl (Fmoc-dipeptides) were found to entangle into fibrous hydrogels (Jayawarna *et al.* 2006; Mahler *et al.* 2006). These hydrogels were found to be stable under cell-culture conditions. Liebmann and co-workers (2007) utilized Fmoc-FF nanotube hydrogel for in situ 3D cell culturing. Their results showed that use of highly biocompatible Fmoc-FF hydrogel components significantly reduced the cytotoxic effects seen with alternate 3D culture materials. In addition, the peptide-derivative hydrogel simplified both handling and loading of the gel to the microstructures, with the ability to easily control the cell type, cell density and composition of each given hydrogel layer. They suggested that it was plausible to design and construct more complex culture systems, which opened the door to new possibilities and new approaches to cell biology. FF fibrils self-assembled in organic solvents can also entangle further to form gels (Yan *et al.* 2008). Yan and co-workers encapsulated quantum dots (QDs) into the FF gel and noted that this was an effective method to protect QDs from oxidation and improve the stability of QDs.

1.4 Aims and Outline of Research

As introduced above, protein nanotubes have a wide range of potential applications in biotechnology. The comprehensive understanding of the properties of these protein nanotubes has become a prerequisite of rational materials design.

The main purpose of the work presented in this thesis is to investigate how to obtain the structural and mechanical information of protein nanotubes utilizing the advantages of atomic force microscopy. Several different protein nanotubes introduced above will be used as examples to develop AFM methods.

Chapter 2 Instrumental and Experimental

Methods

Atomic force microscopy (AFM) is a powerful tool to investigate the morphology and mechanical properties of protein nanotubes. In this chapter, the principles of AFM will be first introduced. Then the protocols of AFM analysis and image processing used in the later chapters will be explained. The preparation of protein nanotube samples for AFM analysis will also be presented.

2.1 Atomic Force Microscopy

2.1.1 Atomic Force Microscopy

AFM, which was invented in 1986, expanded the application of scanning tunnelling microscopy to nonconductive, soft, and live biological samples (Binnig *et al.* 1986; Zasadzinski *et al.* 1998; Marti *et al.*, 1998). AFM has several capabilities including the ability to characterize topographic details of surfaces from the submolecular to the cellular level (Radmacher *et al.* 1992), monitor the dynamic processes of single molecules in physiologically relevant solutions (Engell and Muller 2000), and measure the forces between interacting molecules (Zlatanova *et al.* 2000). AFM is a powerful tool for characterizing the structural properties of macromolecular complexes both in air and under near-physiological conditions. In addition, modified AFMs can be used to manipulate single

molecules (Yang *et al.* 2003). In the past two decades, the application of AFM has spread to many areas of biological sciences including studies of DNA (Fritzsche *et al.* 1997; Hansma 2001), RNA (Lyubchenko *et al.* 1992; Bonin *et al.* 2000; Henn *et al.* 2001; Liphardt *et al.* 2001), proteins (Heymann *et al.* 1997; Isralewitz *et al.* 2001), lipids (Dufrene 2000; Balashev *et al.* 2001), carbohydrates (Misevic 1999; Dettmann *et al.* 2000; Marszalek *et al.* 2001), biomolecular complexes (Lyubchenko *et al.* 1995; Willemsen *et al.* 2000; Safinya 2001), organelles (Oberleithner *et al.*, 1997; Danker and Oberleithner 2000) and cells (Henderson 1994; Ohnesorge *et al.* 1997).

2.1.1.1 Principle of AFM

The principle of the AFM is relatively simple (**Figure 2-1**). The key element of the AFM is the cantilever. It consists of one or more beams of silicon or silicon nitride of 100–500 μm in length and 0.5–5 μm in thickness. At the end of the cantilever a sharp tip is mounted to sense the force acting between it and the sample surface. Photos of general purpose silicon nitride cantilevers (Veeco Probes, Camarillo, CA, USA) are shown in **Figure 2-2**. For normal topographic imaging, the tip is brought into continuous or intermittent contact with the sample as it raster-scans over the surface. An optical system is then used to measure the changes of the laser beam reflected from the gold-coated back of the cantilever onto a position-sensitive photodiode (PSPD), which can measure changes in the position of the incident laser as small as 0.1 nm.

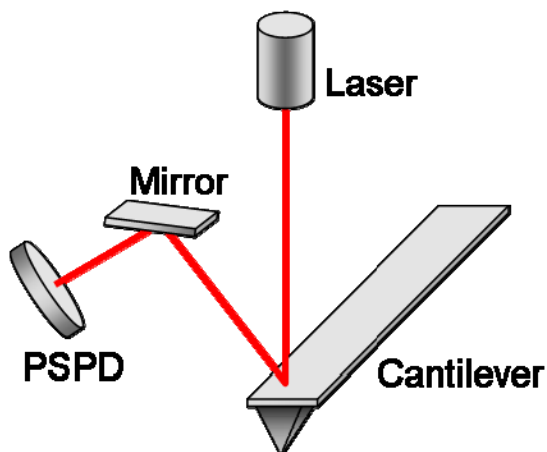


Figure 2-1 Schematic of the concept of AFM and the optical lever.

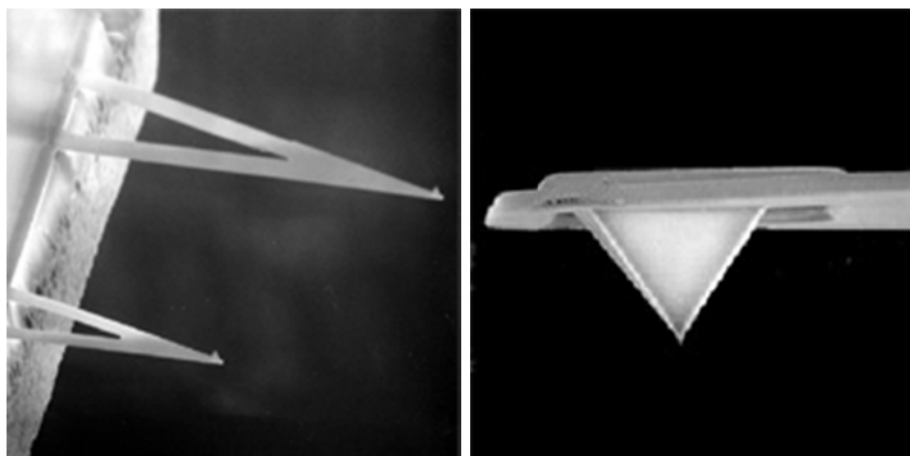


Figure 2-2 Photos of a general purpose silicon nitride cantilever produced by Veeco Probes. Two cantilevers with the tips pointing upwards are shown on the left. A tip is shown on the right. The tip height is 2.5-3.5 μm , the thickness of the cantilever is 0.4-0.7 μm . The triangular cantilever lengths are 196 μm and 115 μm respectively.

<URL: https://www.veecoprobes.com/probe_detail.asp?ClassID=17> [Accessed 22 Feb 2008]

2.1.1.2 Operation Modes of AFM

The AFM is available in several operating modes, including contact mode and tapping mode, which are chosen depending on the sample, environment, and measurements required.

In contact mode (CM), the AFM cantilever is deflected by the sample surface (Yang *et al.*, 2003). Generally, the cantilever deflection is kept constant by the use of a piezoelectric feedback system which permanently regulates the vertical (z) position of either the tip or the sample and produces a constant force image (Bonnell 2001). The image represents the topographic structure of the surface. Deflection is not the most sensitive measurement, having a relatively small signal-to-noise ratio. Furthermore, due to direct contact with the sample, the scanning motion induces lateral forces onto the material which can be intolerable for soft surfaces. However, in some cases, contact mode is still the imaging mode of choice. For example, the alternative modes do not provide the direct information of the force applied onto the sample surface by the tip (Salvetat 1999).

Tapping mode (TM) uses an alternative and more sensitive measurement: the vibrational characteristics of the cantilever. The mechanical resonant frequency of the cantilever is determined by the dimensions of the structure and the properties of materials from which it is made. The vibration amplitude detected at a given frequency changes as a function of the force gradient. Varying the vertical position of the tip such that the amplitude of oscillation at a particular frequency is constant produces a constant force gradient image. TM has a larger signal-to-noise ratio than does CM (Bonnell 2001). It also generates smaller lateral forces on the sample, which improves the lateral resolution of the AFM image, as well as

reducing the damage to the sample while scanning. Consequently, TM is often preferred over CM for most biological applications (Yang *et al.*, 2003).

Phase imaging is relatively new and has the advantage of being able to be performed at the same time as topographic imaging with tapping mode, i.e. both topographic and phase images can be obtained in a single scan. Because the interactions between the tip and the surface depend not only on the topography of the sample but also on other characteristics (such as hardness, elasticity, adhesion, or friction), the movements of the cantilever to which the tip is attached depend also on these properties. In phase imaging, the phase of the sinusoidal oscillation of the cantilever is measured relative to the driving signal applied to the cantilever to cause the oscillation. Phase images are produced by recording this phase shift during the tapping mode scan. Phase imaging can detect, for example, different components in polymers related to their stiffness or areas of different hydrophobicity in hydrogels immersed in saline solutions (Magonov and Reneker 1997).

2.1.1.3 Force Measurements by AFM

In addition to imaging AFM can also probe elastic properties or adhesion on a surface by generating force curves. These curves are generated by performing controlled vertical tip-sample interactions, without lateral scanning movement and while recording the cantilever's deflections. Force curves measure nano- to piconewton range vertical forces applied to the surface, and allow the estimation of the nanomechanical properties of the samples. The ability to coat the tip with different molecules (proteins, lipids) has increased the utility of force curves in understanding the specific attraction between a ligand and its receptor (Dammer *et*

al. 1996; Vinckier *et al.* 1998). This technique can also be used to measure charge densities on surfaces (Heinz and Hoh 1999), to estimate the folding force of biomolecules like titin (Rief *et al.* 1997), and to measure forces associated with polymer elongation (Rief *et al.* 1998).

Conversion of force curves

The direct result of a force measurement is a curve of the photodiode current I versus height position of the piezoelectric translator Z_p . In order to obtain the curve of tip-sample interactive force F versus piezo displacement Z_p , the I signal must be converted to F . This is explained as follows by an ideal example as in **Figure 2-3**, which is a model curve as would be observed for an infinitely hard sample surfaces with no surface forces. The curves of the tip approaching to and retracting from the surface are identical. The horizontal part (**Figure 2-3 A-B**) is the non-contact line. The linearly increasing part (**Figure 2-3 B-C**) is the contact line, from the slope of which the sensitivity $\Delta I/\Delta Z_p$ can be obtained. The I signal can be converted into a cantilever deflection Z_c by dividing the I signal by the sensitivity, which leads to $Z_c = I/(\Delta I/\Delta Z_p)$. Knowing the spring constant of the cantilever k_c , the I signal can easily be converted into force according to Hooke's Law: $F = k_c Z_c$. The non-contact line defines zero deflection of the cantilever, which is therefore the zero force line (Butt *et al.* 2005).

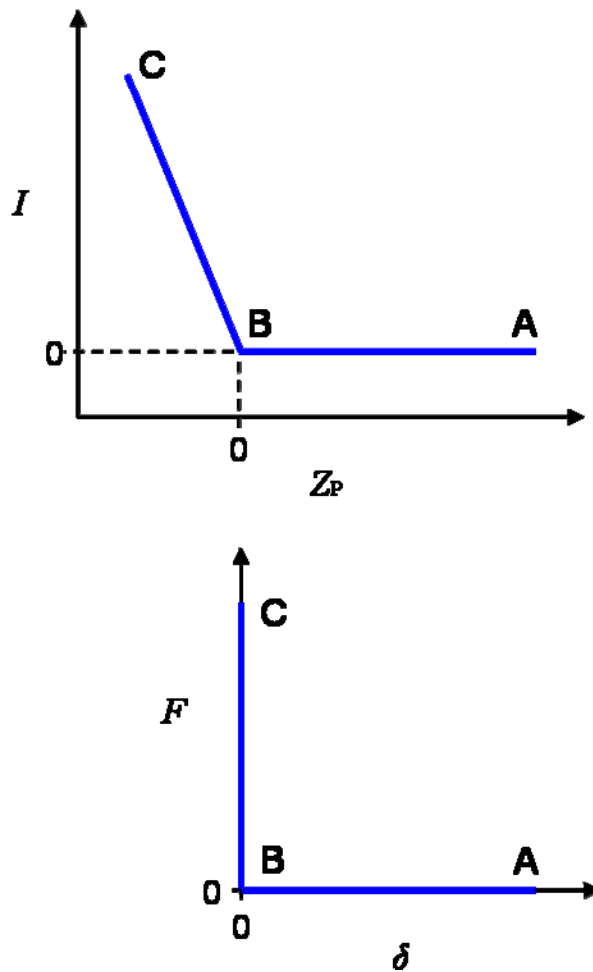


Figure 2-3 A model force measurement curve recorded for an infinitely hard material surface with no surface forces. The approaching and retracting curves are identical. The I vs. Z_p curve is converted to F vs. δ curve. A-B is the non-contact line and B-C is the contact line.

Problem of zero tip-sample distance

The true tip-sample distance, or the indentation δ is the piezo displacement Z_p deduced by the cantilever deflection Z_c : $\delta = Z_p - Z_c$. Using the ideal example of an infinitely hard sample surface without surface forces again (**Figure 2-3**), the definition of zero indentation is as follows: The zero cantilever deflection Z_{c0} lies on the horizontal non-contact line (**Figure 2-3** A-B). The point where the two linear

parts of the force curve cross is defined as zero piezo displacement Z_{P0} (Figure 2-3 B). The curve of force F versus piezo displacement Z_p then can be converted to force F versus indentation $\delta (= (Z_p - Z_{P0}) - (Z_c - Z_{c0}))$ curve.

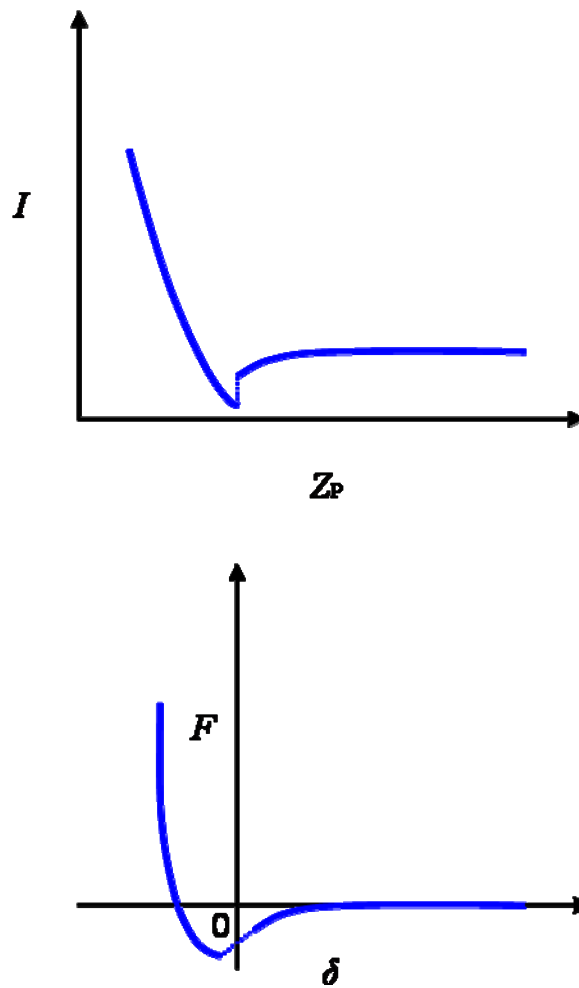


Figure 2-4 A force measurement retracting curve for a deformable material with attraction and adhesion forces. The I vs. Z_p curve is converted to F vs. δ curve.

However, in reality, especially for biological samples, the definition of zero indentation is more complicated. A typical retracting force curve of deformable materials with surface forces is displayed in **Figure 2-4**. Note that for deformable materials, the approach and retract curves of a force measurement are no longer

identical. The approach curve is used to define zero tip-sample distance. The zero cantilever deflection lies on the horizontal non-contact line at large distances away from the surface, where surface forces are negligible. The sensitivity is obtained from the linear contact part of the approach curve. One way to find the zero piezo displacement Z_{P0} is to extrapolate the two linear regimes of the approach curve. Another way to find Z_{P0} , which is more robust and reliable, is to fit experimental data in the range on the approach curve when the tip and sample are in contact using a Hertzian model as described in **Equation 2-1** (Hertz 1882; Rotsch *et al.* 1999; Bhanu and Hörber 2002).

$$Z_P - Z_{P0} = (Z_c - Z_{c0}) + \sqrt{\frac{k_c \cdot (Z_c - Z_{c0})(1 - \nu^2)}{(2/\pi) \cdot E \cdot \tan(\alpha)}}$$

Equation 2-1

where k_c is the spring constant; α is the half-opening angle of a conical shaped tip; ν is the Poisson ratio and E is the elastic modulus. E and Z_{P0} are two unknown variables, which are determined by the fit. By employing a Monte Carlo fit, it is possible to optimize values of E and Z_{P0} . Igor software (Igor Pro version 4; WaveMetrics, OR, USA) was used to perform this type of fitting in chapter 5 of this thesis.

Determination of spring constant of the cantilever

For AFM force measurements, the value of spring constant of the cantilever is usually needed. Several methods have been described, but many do not appear to be simple, reliable and precise at the same time (Albrecht *et al.* 1990; Butt *et al.* 1993; Neumeister and Ducker 1994; Sader 1995; Sader *et al.* 1995, 1999; Senden and Ducker 1994; Cleveland *et al.* 1993; Gibson *et al.* 1996).

Hutter and Bechhofer (1993) proposed an elegant and widely used method, which is implemented in many commercial AFMs. They suggested to measure the intensity of the thermally excited cantilever oscillations or the cantilever thermal noise. For an ideal spring of spring constant k_c , the mean square deflection of the cantilever is:

$$\langle Z_c^2 \rangle = \frac{k_B T}{k_c}$$

Equation 2-2

where k_B is the Boltzmann constant and T is the absolute temperature.

In reality, considering the shape of the cantilever (which leads to several possible vibration modes) (Butt and Jaschke 1995) and the systematic error of the deflection detecting technique (usually optical lever technique) (Stark *et al.* 2001), there is:

$$k_c = \beta^* \frac{k_B T}{\langle Z^{*2} \rangle}$$

Equation 2-3

where Z^* is the effective deflection, which is the deflection read from the instrument after determining the sensitivity from the contact part of a force curve on a hard substrate; β^* is the effective correction factor, which is 0.817 for a rectangular cantilever and 0.764 for a V-shape cantilever (Stark *et al.* 2001).

In practice, a force curve is acquired on a hard substrate to characterize the sensitivity, and then a noise spectrum of the deflection amplitude is taken. This spectrum shows a peak at the resonance frequency. The peak is fitted with a Lorentzian curve and the mean square deflection of the peak is obtained by

integration. The thermal noise method was used to obtain the spring constant of cantilever in chapters 5 and 6 of this thesis.

2.1.2 AFM Analysis

AFM Imaging

AFM imaging experiments presented in section 3.1, 3.2, 4.2, 4.3 and 6.2 were carried out using MultiMode scanning probe microscope with Nanoscope IIIa controller (Veeco, Metrology Group, Santa Barbara, CA, USA) equipped with an E-scanner (maximum scan size $10\ \mu\text{m} \times 10\ \mu\text{m}$, vertical range $2.5\ \mu\text{m}$). AFM imaging experiments presented in section 3.3, 4.4 and 6.3.1 were carried out using the same MultiMode AFM equipped with a J-scanner (maximum scan size $125\ \mu\text{m} \times 125\ \mu\text{m}$, vertical range $5.0\ \mu\text{m}$).

For the AFM imaging experiments presented in section 6.3.2 and 6.3.3, an EnviroScope AFM (eScope AFM; Digital Instruments) was used. This AFM has an enclosed sample chamber allowing the control of temperature (from room temperature up to 185°C in air) and humidity (range of 0-80% RH).

Silicon probes (OMCL-AC160TS, Olympus Optical, Tokyo, Japan) with nominal spring constant $34.4\sim 74.2\ \text{N/m}$ were used for images obtained using tapping mode in air. V-shaped silicon nitride levers (Veeco Probes, Camarillo, CA, USA) with a nominal spring constant of $0.32\ \text{N/m}$ were used for images obtained using tapping mode in liquid. The V-shaped silicon nitride levers (Veeco Probes) with nominal spring constants of $0.06\ \text{N/m}$ were used for contact mode in air (these are all manufacturer's data). Scan rates employed were typically $1.0\text{-}2.0\ \text{Hz}$.

AFM force measurements

Force measurements presented in chapter 5 were carried out using MultiMode AFM equipped with a Picoforce module (Digital Instruments). V-shaped silicon nitride levers (Veeco Metrology Group) with nominal spring constants of 0.06 N/m (manufacturer's data) were used for force measurements.

2.1.3 Image Processing

AFM image data were analyzed with SPIP software (The Scanning Probe Image Processor, Version 3.3.9.0; Image Metrology A/S, Denmark). It should be noted that, in this thesis, the “height” of a sample means the vertical difference between the top of the sample and the substrate surface; while the “width at the half height” means the horizontal width of a sample at the half of the height of the sample. It is demonstrated in **Figure 2-5** how the height and the half height width of a diphenylamine nanotube from an AFM height image were determined using SPIP software.

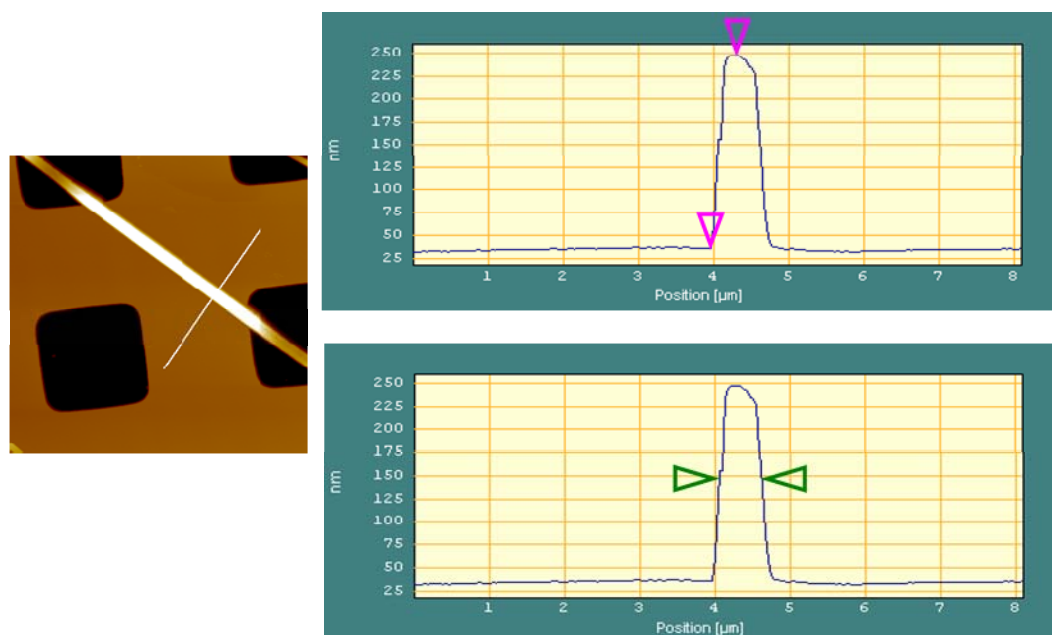


Figure 2-5 Measurement of the dimensions of a protein nanotube from an AFM height image using SPIP. The left picture is an AFM height image of a diphenylalanine nanotube on silicon grid substrate with square holes of $5\ \mu\text{m} \times 5\ \mu\text{m}$. The two pictures on the right are the profiles along the white line (which is perpendicular to the direction of the nanotube of interest) on the left image. The vertical difference between the tips of the two pink triangles on the top right profile is the “height” of the nanotube. The horizontal difference between the tips of the two green triangles on the bottom right profile is the “width at the half height”.

2.2 Preparation of Protein Nanotubes

2.2.1 Bacterial Flagellar Filaments

Salmonella flagellar filaments were removed from cells by mechanical shearing. Deflagellated cells were removed by centrifugation, and then the flagellar filaments were collected by ultracentrifugation. *Salmonella* flagellar filament samples were stored in 10mM HEPES (pH 7.0, pKa 7.31) and were kindly

provided by Dr. Richard Woods from Queen's Medical Centre (QMC), University of Nottingham.

2.2.2 Lysozyme Fibrils

Chicken egg-white lysozyme (dialyzed lyophilized powder; Sigma Chemical Company, St. Louis, MO, USA) was dissolved to 10mg/mL in 10mM glycine ($C_2H_5NO_2$; SigmaUltra; Sigma Chemical Company) buffer (pH 2.0). Then lysozyme solution was incubated in an electrical oven at 57 ± 2 °C (Krebs, *et al.* 2000).

2.2.3 β 2-Microglobulin Fibrils

β 2-microglobulin (lyophilized powder; Sigma) was dissolved to 2mg/mL in 25mM sodium acetate (CH_3COONa ; Sigma) and 25mM sodium phosphate (Na_3PO_4 ; Sigma) buffer (pH2.5). Then β 2-microglobulin solution was incubated at 37 °C in an incubator.

2.2.4 Diphenylalanine Nanotubes (FF Nanotubes)

The diphenylalanine peptides were purchased from Sigma-Aldrich (Gillingham, Dorset, UK). Fresh stock solutions were prepared by dissolving the lyophilised peptides in 1,1,1,3,3,3-hexafluoro-1-propan-2-ol (HFIP) (Sigma Aldrich) at a concentration of 100 mg/mL. In a typical preparation, a stock solution of ~ 20 μ L was made in an eppendorf tube.

The diphenylalanine peptides stock solution was diluted in double distilled H_2O to a final concentration of 2 mg/mL. In a typical preparation, 2 μ L peptides stock solution was added into 98 μ L distilled H_2O in an eppendorf, and the sample solution was vortexed for 20~30 seconds. An aliquot of 10 μ L of sample solutions

were then immediately dropped onto the substrates and were subsequently dried under a gentle flow of nitrogen.

2.2.5 Sample Preparation for AFM Analysis

Substrates employed for AFM analysis

The substrates used in this thesis were mica, gold or silicon grid.

Mica (Agar Scientific, Essex, UK) surfaces were freshly cleaved prior to sample application.

Gold substrates were prepared by coating gold onto freshly cleaved mica surfaces using an evaporation gold coater. Gold was deposited at ~ 280 °C under 10^{-6} mbar, and then annealed at ~ 320 °C for 24 hours (Hegner *et al.* 1993; Wagner *et al.* 1995; Huang *et al.* 2001). The gold substrate was then UV cleaned (UV cleaner from Scientific & Medical Products Ltd., Cheshire, UK) for 10 minutes prior to applying the nanotube sample. Gold substrate prepared in this way had flat islands (typically 0.2 μm to 1.0 μm in width), separated by gaps ~ 30 nm to ~ 150 nm in width (**Figure 2-6**).

Micropatterned silicon substrates (with holes of 5 $\mu\text{m} \times 5$ μm and 200 nm deep) (**Figure 2-7**) were cleaned with the UV cleaner (Scientific & Medical Products Ltd.) for 10 minutes prior to applying the sample.

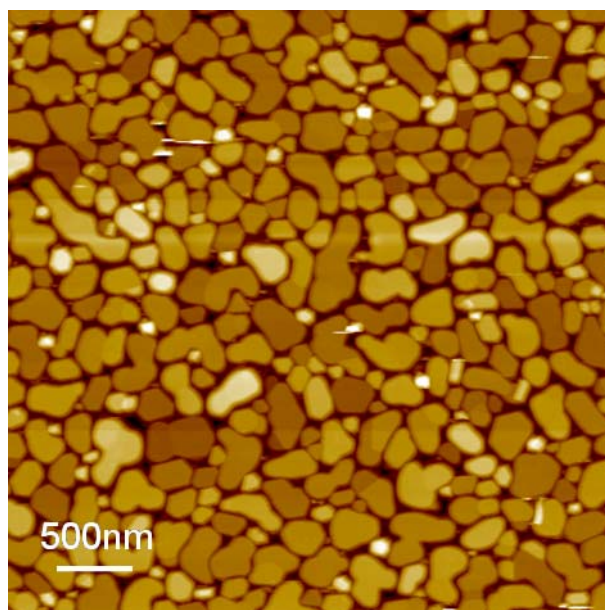


Figure 2-6 AFM height image of gold substrate obtained using evaporation gold coater. The image was obtained in tapping mode in water. There are gaps between gold plateau. Those gaps are ~ 30 nm to ~ 150 nm in width. The Z-range of the image was 237.3 nm.

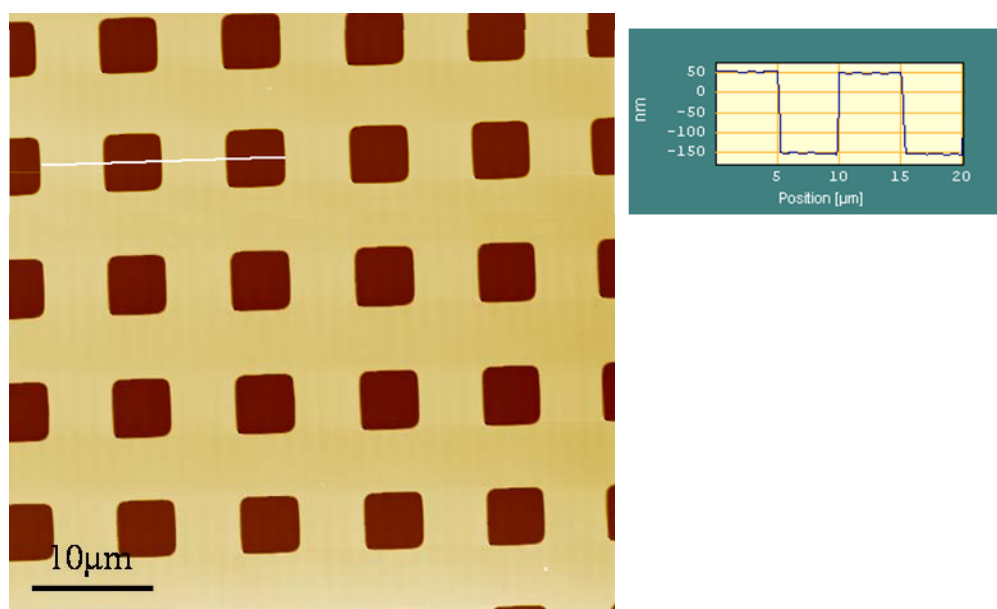


Figure 2-7 An AFM height image of a micropatterned silicon substrate with holes of $5 \mu\text{m} \times 5 \mu\text{m}$ and 200 nm in depth. The pitch of this substrate is 10 μm. The right picture is the profile of the white line on the left image, which shows two pitches of the substrate.

General sample preparation protocols for AFM analysis

The general protocol for sample preparation for AFM analysis was as follows:

Stocks of samples were first diluted with a range of solutions employed for AFM sample preparation. These solutions were prepared from the following chemicals as needed: Hydrochloride acid (36.5-38.0%), sodium hydroxide (pellet), propanol (anhydrous), phosphate-buffered saline (tablet), magnesium chloride (power), which were also purchased from SIGMA[®].

For AFM imaging in air, a 10 μ L droplet of the appropriate sample solution was applied to a substrate. The sample solution was left to stand on the substrate for a certain time to allow the sample to deposit onto the mica surface; samples were then rinsed using distilled water, and then dried in a gentle flow of nitrogen. Rinsing the surface was required to remove solution components, but care was taken as over-washing could denature samples and also decrease the coverage. Under-drying can potentially reduce AFM resolution because samples can move around on moist surfaces. Conversely, over-drying can alter the features of the samples because of dehydration of the protein (Bonnell 2001). The mica with the sample was attached to a metal stub using double-sided sticky tape and mounted onto a strong magnet located on the sample stage.

For AFM imaging in liquid, a 10 μ L droplet of the appropriate sample solution was applied to the substrate. The substrate with the sample was attached to a metal stub using double-sided sticky tape and mounted onto a strong magnet located on the sample stage. A standard fluid imaging cell (Veeco) was needed to seal the solution, to prevent evaporation and allow for solution exchange. Solution was injected into the fluid cell with a syringe, and for some experiments, the

solution in the cell had to be changed during experiments. During this latter process new solution was carefully injected into the cell, while old solution was drawn out through the other channel of the cell by a second syringe.

Variation in deposition procedures (for imaging in air or in liquid) can affect the quality of the image. For example, longer deposition times can increase coverage of samples but also increase the chances that the features of the samples are altered by interaction with the surface (imaging in air or in liquid) or by the effects of buffer solution (imaging in liquid). For these studies, the shortest deposition time that provided reasonable surface coverage was optimal.

Chapter 3 Dynamic Processes of Assembly and Degradation of Protein Nanotubes

The AFM is capable of monitoring a range of dynamic processes, including biomaterial assembly and degradation under near-physiological conditions (Engel and Müller, 2000). If the process of interest occurs on the scale of a few minutes to a few hours, and the conditions of such process are suitable for AFM operation, real-time monitoring can be obtained. Otherwise the process needs to be interrupted, and individual samples at certain time parts prepared for AFM analysis. Here three processes occurring on different time scales will be investigated and discussed, as examples to explore this ability of AFM to understand the dynamic properties of protein nanotubes. This chapter also provide the imaging study as foundation to support further studies on physical properties in later chapters (chapter 4, 5 and 6).

3.1 Flagellar Filaments in Different Environment

3.1.1 Flagellar Filaments on Mica in Air

Salmonella flagellar filaments were firstly imaged on mica in air, as it is generally the simplest AFM imaging condition (see section 2.2.5), which establishes the basic experimental conditions for further investigations.

Stock solutions of *Salmonella* flagellar filaments were diluted 100 times using pH 7.0 buffer solution (10 mM PBS), and then imaged using tapping mode AFM in air on mica (**Figure 3-1**; detailed sample preparation see section 2.2).

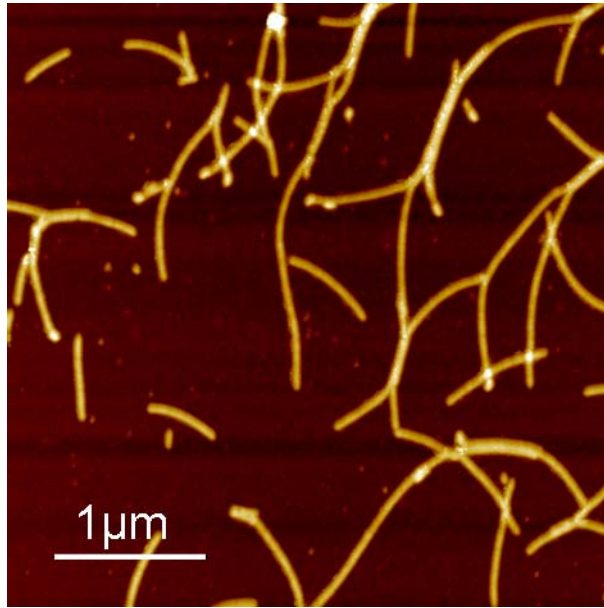


Figure 3-1 Tapping mode AFM height images of *Salmonella* flagellar filaments in air on mica. Stock sample solutions were 100 times diluted. The Z-range is 37.3 nm.

The contour length of *Salmonella* flagellar filaments was found to be 1.0 ± 0.4 μm (**Figure 3-2**). The shorter filaments are most likely the fragments resulted from the mechanical shearing during the filaments preparation (see section 2.2.1). The average height of the filaments was 4.5 ± 0.6 nm.

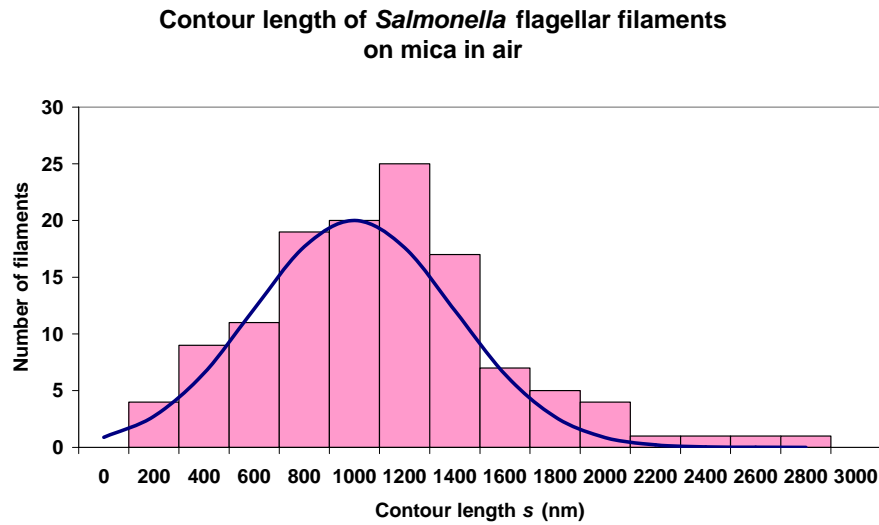


Figure 3-2 Histogram of the contour length measured for *Salmonella* flagellar filaments on mica in air. The mean contour length measured was $1.0 \pm 0.4 \mu\text{m}$ ($N = 125$).

3.1.2 Dissociation of Flagellar Filaments in Low pH Environment

Salmonella flagellar filaments are known to dissociate in acid environments (Namba and Vonderviszt 1997). Here, in order to directly monitor this dissociation process, the conditions required to image the filaments in aqueous environments first needed to be established.

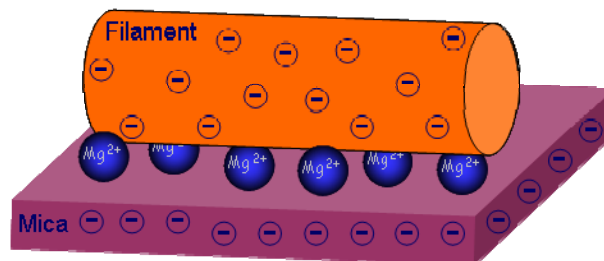


Figure 3-3 A sketch demonstrates that Mg^{2+} works as a bridge between flagellar filaments and the mica surface in pH 7.0 buffer solution.

Because the isoelectric point (pI) of flagellin is 5.2 and the amino acid residues on the outer surface of *Salmonella* flagellar filaments are mostly charged residues (Namba and Vonderviszt 1997), in $pH > 5.2$ solution, the surface of *Salmonella* flagellar filaments will be negatively charged; as is the surface of the mica substrate (Vesenka *et al.* 1992). Therefore, without the inclusion of additional ions, the imaging of the *Salmonella* flagellar filaments on mica substrates is problematic due to poor immobilization. Two methods were explored to resolve this problem. First, magnesium ions (Mg^{2+}) were added into solution to immobilize the *Salmonella* flagellar filaments onto the mica surface (**Figure 3-3**) (Vesenka *et al.* 1992, see section 3.1.1 and 3.1.3); second, AFM images were obtained at a pH at least lower than 5.2 (see section 3.1.2).

3.1.2.1 *Salmonella* Flagellar Filaments in Neutral Condition

Salmonella flagellar filaments were first imaged in pH 7.0 solution. A height image taken in pH 7.0 buffer solution (10 mM PBS & 10 mM $MgCl_2$) using tapping mode AFM is displayed on **Figure 3-4**. To prepare samples for imaging, stock solution of *Salmonella* flagellar filaments (for preparation of stock solution see section 2.2.1) was diluted 100 fold using pH 7.0 buffer solution (10 mM PBS & 10 mM $MgCl_2$). A 10 μ L droplet of diluted sample solution was spread on a freshly cleaved mica surface, and left for 1 hour on mica, before covering with pH 7.0 buffer solution (10 mM PBS & 10 mM $MgCl_2$) for AFM imaging. There are two long filaments and two short filaments visible in **Figure 3-4**. Some very short flagellar filament fragments can also be seen in **Figure 3-4**, which were probably produced during the mechanical shearing process when the flagellar filaments were removed from the living cells (see section 2.2.1).

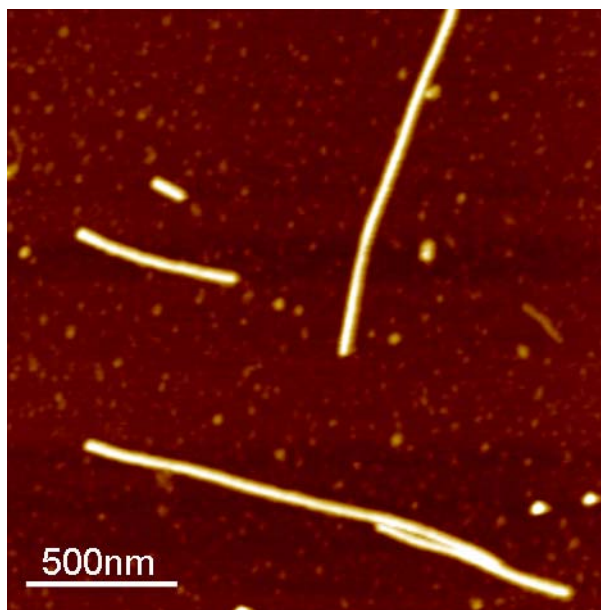


Figure 3-4 A height image of *Salmonella* flagellar filaments taken in pH 7.0 buffer solution (10 mM PBS & 10 mM MgCl₂) using tapping mode AFM. The Z-range is 9.3 nm.

3.1.2.2 Salmonella Flagellar Filaments in Weak Acidic Condition

As stated above, in low pH solution (pH<5.2), *Salmonella* flagellar filaments would be positively charged, therefore, they could be immobilized directly onto the mica surface via electrostatic attraction. A height image taken in pH 4.4 solution using tapping mode AFM is displayed in **Figure 3-5**. Stock solution of *Salmonella* flagellar filaments was diluted 100 fold by HCl to achieve a final pH of 4.4 for AFM imaging. A 10 μ L droplet of sample solution was spread on a freshly cleaved mica surface and left for 1.5 h before covering with HCl (pH 4.4) solution for AFM imaging.

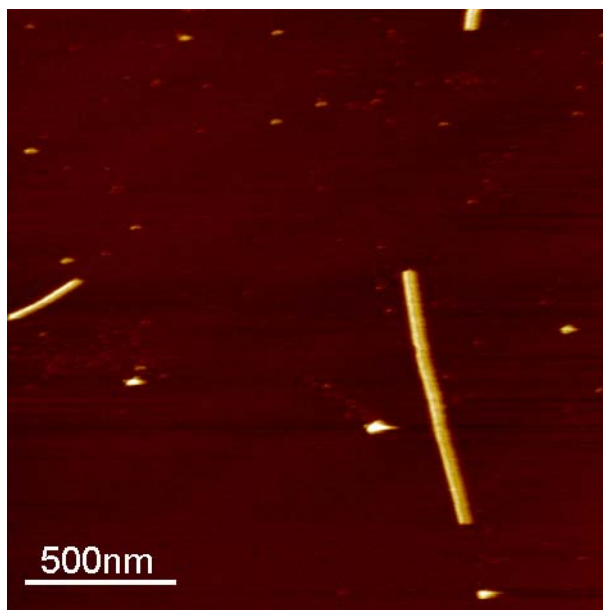


Figure 3-5 A height image of *Salmonella* flagellar filaments taken in HCl solution (pH 4.4) using tapping mode AFM. The Z-range is 14.2 nm.

3.1.2.3 Salmonella Flagellar Filaments in Alkaline Condition

Salmonella flagellar filaments were also imaged in alkaline solution, with the presence of Mg^{2+} ions. A height image taken in pH 10.0 solution (0.1mM NaOH & 10 mM $MgCl_2$) using tapping mode AFM is displayed on **Figure 3-6**. The stock solution of *Salmonella* flagellar filaments was diluted 100 fold with solution (0.1mM NaOH & 10 mM $MgCl_2$) to a final pH of 10.0 for AFM imaging. A 10 μ L droplet of sample solution was spread on a freshly cleaved mica surface and allowed to stand for 1h before covering with solution (0.1mM NaOH & 10 mM $MgCl_2$, pH 10.0) for AFM imaging.

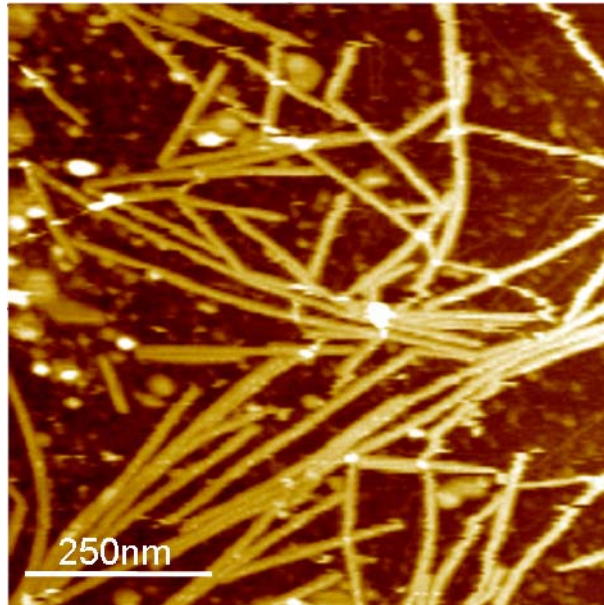


Figure 3-6 A height image of *Salmonella* flagellar filaments taken in pH 10.0 solution (0.1mM NaOH & 10 mM MgCl₂) using tapping mode of AFM. The Z-range is 22.6 nm.

The results of AFM experiments of *Salmonella* flagellar filaments in acidic, alkaline and neutral environments are presented in **Table 3-1** for comparison. The dimensions were measured using SPIP software (see section **2.1.3**).

The cross section of *Salmonella* flagellar filaments is known to be circular (Mimori *et al.* 1995; Morgan *et al.* 1995). However, measured from AFM images, the diameters were found to be bigger than the height measurements (**Table 3-1**). This may be because of three reasons: First, it may be due to tip broadening phenomena. Tip broadening arises when the radius of curvature of the tip is comparable with, or greater than, the size of the feature being imaged (West and Starostina n.d.). The diagram in **Figure 3-7** illustrates this problem. As the tip scans over the filament, the sides of the tip make contact before the apex, and the microscope begins to respond to the feature. Second, the pressure caused by the AFM tip may also result in compression of the *Salmonella* flagellar filaments

(Morris *et al.* 1999). Third, the attraction between the *Salmonella* flagellar filaments and the mica surface may also result in some compression and a decrease the height of the filaments (Israelachvili 1992).

Table 3-1 The dimensions of *Salmonella* flagellar filaments observed in AFM images obtained in liquid.

pH of the solutions	pH 4.4	pH 7.0	pH 10.0
Diameter D (nm)	33.7 ± 0.8	26.8 ± 0.8	34.2 ± 0.9
Height H (nm)	7.2 ± 0.6	9.1 ± 0.5	7.1 ± 0.6
Length L (μm)	1.0 - 3.0		
N	5	8	10

N is the number of *Salmonella* flagellar filaments measured; *D* is the average diameter of *Salmonella* flagellar filaments; *H* is the average height of *Salmonella* flagellar filaments; *L* is the length range of the most *Salmonella* flagellar filaments observed. All the images were taken in liquid using tapping mode AFM and analyzed using SPIP software (see section 2.1.3).

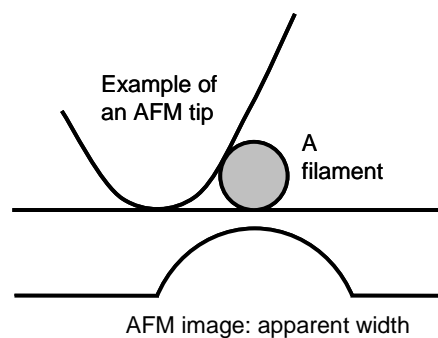


Figure 3-7 Sketch of an example of "tip broadening" effect on a filament. On the bottom a resulting scan line is shown.

Although the dimensions of *Salmonella* flagellar filaments in AFM images may be affected by the difference of the AFM tips and/or the imaging conditions employed (e.g. set point), the observed dimensions may still provide useful information on the environmental effect on the filaments. For example, the average diameter of *Salmonella* flagellar filaments measured in pH 4.4 solution was ~33% wider than in pH 7.0 solution; while the average height measured in pH 7.0 solution was ~24% less in pH 4.4 solution. This may be because *Salmonella* flagellar filaments were “softer” and more compressible by AFM tip under low pH environment.

The height and the diameter of the filaments in alkaline solution are close to the dimensions of the filaments in weak acidic solution, which indicates that the conformations of *Salmonella* flagellar filaments in acidic and alkaline environments may be similar (Kamiya and Asakura 1976; also see section 1.2.2.3).

3.1.2.4 Dissociation of Salmonella Flagellar Filaments in Acidic Condition

Salmonella flagellar filaments are not stable in low pH environments (pH<4.4), where they are likely to be dissociated into single flagellin proteins (Namba and Vonderviszt 1997).

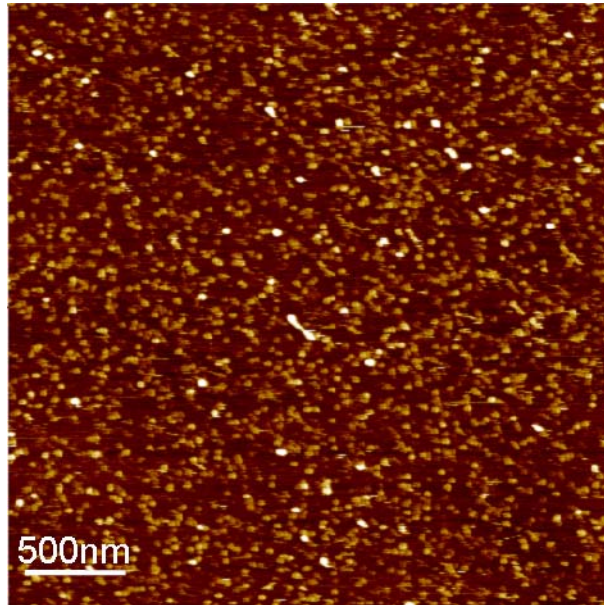


Figure 3-8 A height image of *Salmonella* flagellar filaments taken in pH 4.0 solution using tapping mode of AFM. The Z-range is 8.8 nm.

A height image of *Salmonella* flagellar filaments taken in pH 4.0 solution using tapping mode AFM is displayed in **Figure 3-8**. Sample solution was allowed to stand for 1 h on mica before imaging. The average height of the particles observed in this image is 2.4 ± 0.3 nm. The particles are most likely single flagellin or subunits of several flagellins (Namba and Vonderviszt 1997). From the sample preparation of these images it was clear that *Salmonella* flagellar filaments dissociated in pH 4.0 solution within 1 h. Therefore to directly observe the process of dissociation, the experiment of changing the pH of solution while imaging was performed.

3.1.2.5 Direct Observation of the Dissociation of Salmonella Flagellar

Filaments in Acidic Condition

The dissociation of *Salmonella* flagellar filaments in acidic solution is shown in **Figure 3-9**. Three filaments were initially imaged in pH 7.0 PBS solution. Image (a) was taken right after the injection of 1mM HCl into the fluid cell (see section 2.2.5), no visible dissociation was observed. Image (b) was taken 20 minutes after the injection. Most parts of the three filaments had undergone a dissociation process, though several fragments of filaments could still be seen (e.g. a fragment in the centre of the cross) in image (b). Image (c) was taken 40 minutes after the injection. There were almost no fragments remaining in image (c). Image (d) was taken 1 hour after the injection. The filaments were completely dissociated into particles and diffusing away from the original site.

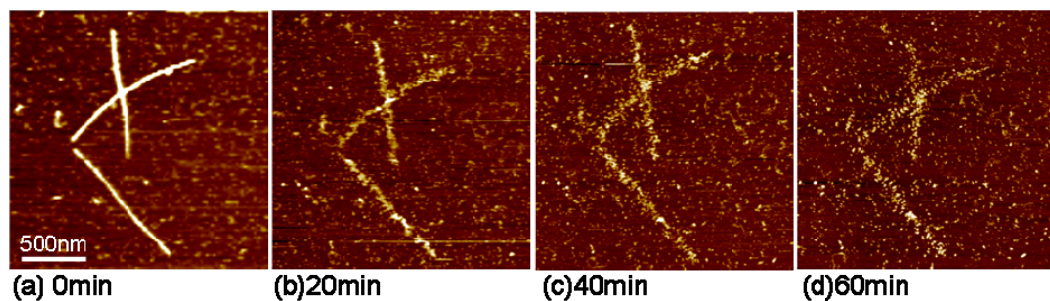


Figure 3-9 Height images of *Salmonella* flagellar filaments in liquid using tapping mode AFM. The sample was in pH 7.0 buffer solution (10 mM PBS & 10 mM MgCl₂) at first, then 1mM HCl was injected into the sample solution. (a) was taken right after injection; then (b) was taken 20 min after injection; (c) was taken 40 min after injection; (d) was taken 1 h after injection. The Z-range is 9.9 nm.

This was the first time that the dissociation process of *Salmonella* flagellar filaments in low pH solution has been visualised by AFM. This study provided highly valuable information for the development of applications for *Salmonella* flagellar filaments. Most of the intersubunit interactions found within the outer tube of flagellar filaments are polar–polar or charge–polar (Yonekura *et al.* 2002; 2003; also see section 1.2.2). When basic residues are protonated, the interactions between flagellin break down. All parts of a filament exposed to the low pH solution were found to break down instantly. The centre piece fragment of the cross in image **Figure 3-9** (b) was probably a fragment from the lower filament of the cross on image (a), which survived in the first 20 minutes because of the protection of the upper filament of the cross from the low pH solution. This could be used advantageously in the controlled digestion of flagellar filaments when flagellar filaments are used as scaffolds to obtain nanowires (Kumara *et al.* 2006; 2007; Woods *et al.* 2007, also see section 1.2.3).

3.1.3 Flagellar Filaments on Gold Surface

Salmonella flagellar filaments on gold substrate also studied. It is part of the study to explore the imaging capability of AFM in different environment, as well as the foundation for studies on physical properties in later chapters (e.g. chapter 4 and 6).

3.1.3.1 Salmonella Flagellar Filaments imaged in Air on Gold Surfaces

Gold substrates were prepared by coating gold onto freshly cleaved mica surface using evaporation gold coater (see section 2.2.5). Stock solutions of *Salmonella* flagellar filaments were diluted 100 times using pH 7.0 buffer solution

(10 mM PBS) and then imaged using tapping mode AFM in air on gold (**Figure 3-10**; detailed sample preparation see section 2.2). The average height of the *Salmonella* flagellar filaments observed on the gold substrates was 4.4 ± 0.6 nm ($N = 20$).

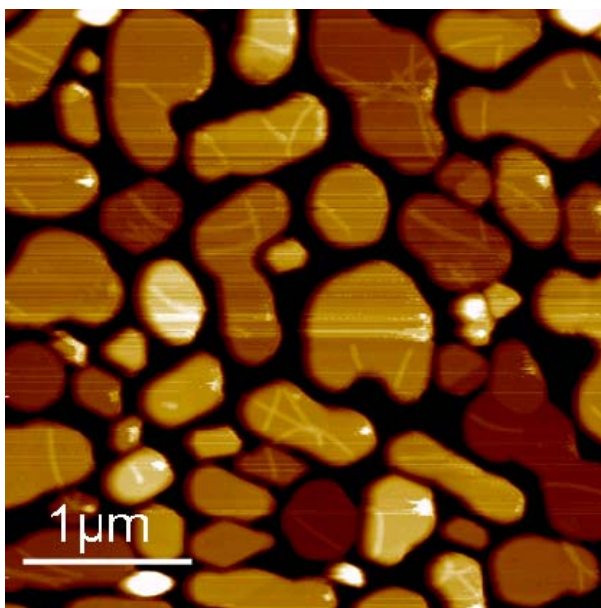


Figure 3-10 Tapping mode AFM height images of *Salmonella* flagellar filaments in air on gold. Stock sample solutions were 100 times diluted. The Z-scale is 351.5 nm.

3.1.3.2 The *Salmonella* Flagellar Filaments in Propanol on Gold Surface

It was found difficult to immobilize *Salmonella* flagellar filaments onto gold substrate while scanning in aqueous buffer solution. However, in propanol or water mixed with propanol (>80% propanol), *Salmonella* flagellar filaments were found to bind to the substrate firmly enough to allow imaging (**Figure 3-11**). This may be due to the dehydration and/or the insolubility of *Salmonella* flagellar filaments in propanol solutions. The dehydration may help to expose the filaments

surface to the probing tip (Hansma *et al.* 1992; 1993; Lyubchenko *et al.* 1993). The influence of imaging condition on the observed filament dimensions was investigated by imaging in a series of propanol-water mixtures (Table 3-2) (Figure 3-12).

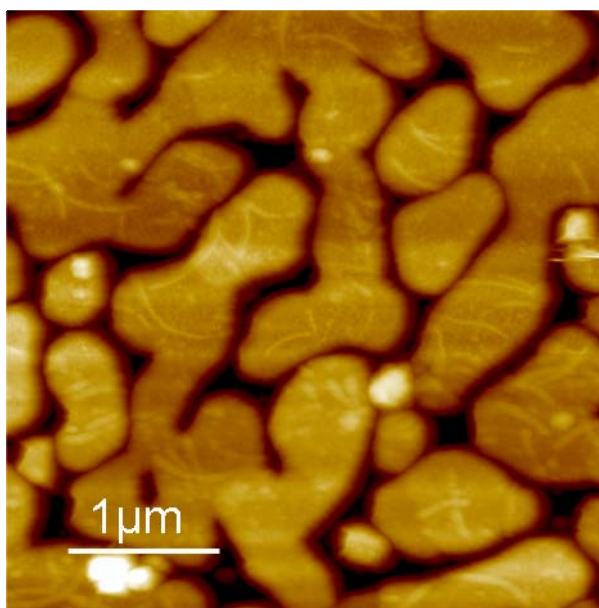


Figure 3-11 Tapping mode AFM height images of *Salmonella* flagellar filaments in 80% propanol on gold. Stock sample solutions were 5 times diluted.

Table 3-2 The average height of *Salmonella* flagellar filaments on gold surface in a series of propanol-water mixtures.

Buffer	100% propanol	90% propanol + 10% water	80% propanol + 20% water
Height (nm)	5.4 ± 0.5	12.2 ± 0.9	17.0 ± 1.1

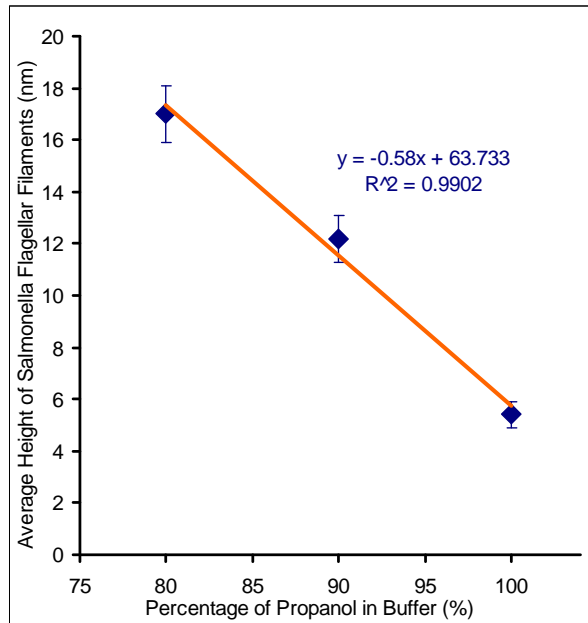


Figure 3-12 A plot of average height of *Salmonella* flagellar filaments vs. percentage of propanol in propanol-water buffer.

In 100% propanol, the average height of *Salmonella* flagellar filaments was close to that observed in air; the average height increased proportionally while the percentage of propanol in buffer decreased. In below a concentration of 70% propanol, *Salmonella* flagellar filaments could not be immobilized onto gold.

3.2 Fibrillization Processes of Lysozyme

Unlike the dissociation of *Salmonella* flagellar filaments in low pH environments which occurred within an hour, the fibrillization of lysozyme takes up to two weeks in laboratory (Krebs, *et al.* 2000, also see section 2.2.2). Therefore, real-time monitoring of this fibrillization process by AFM imaging is not feasible. In order to observe it, the assembly process has to be interrupted, so that samples can be prepared for AFM analysis.

3.2.1 Preparation of Lysozyme Samples

Lysozyme protein dissolved in glycine buffer was incubated at 57 ± 2 °C (details see section 2.2.2). After a certain incubation time, the sample was removed from the oven to room temperature and a 10 μ L droplet of sample solution spread onto a freshly cleaved mica surface. After 2 minutes, the mica surface was rinsed with distilled water, and then dried under a gentle flow of nitrogen gas. The sample then was imaged with AFM using tapping mode in air (Figure 3-16 to Figure 3-23). This AFM sample preparation process, especially the drying procedure stopped the continuous fibrillization of lysozyme.

Glycine buffer was imaged under the same conditions before and after incubation as the control experiment (Figure 3-13). A few particles (height range from ~ 2 nm to ~ 10 nm) were observed on the images, which we attribute to undissolved glycine powder produced when the buffer was prepared.

The initial lysozyme sample was also imaged prior to incubation (Figure 3-14). Lysozyme protein is known to have hydrodynamic diameter of 4.1nm (Merrill, *et al.*, 1993). Particles of lysozyme proteins were observed on the AFM images. The average height of lysozyme particles measured from AFM images was 1.6 ± 0.5 nm. A histogram of the height of lysozyme particles was displayed in Figure 3-15. The particles observed are most likely single lysozyme proteins or clusters of several lysozyme proteins. The average height obtained however was smaller than the previously known diameter of lysozyme protein. The reduction of the diameter is most likely due to the drying process during the sample preparation and/or the pressure caused by the AFM probe while scanning (Rossell 2003).

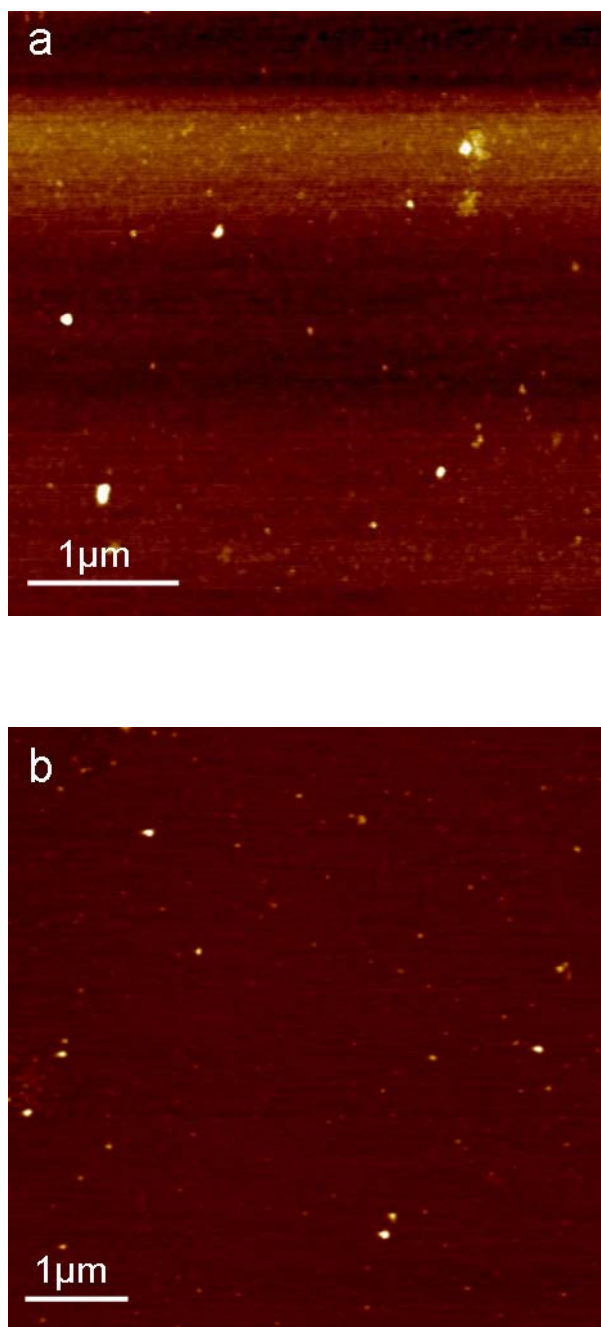


Figure 3-13 An AFM height image of 10 mM glycine buffer obtained using tapping mode AFM before (a) and after (b) incubation at 57 ± 2 °C for 2 weeks. The Z-range is 8.1 nm.

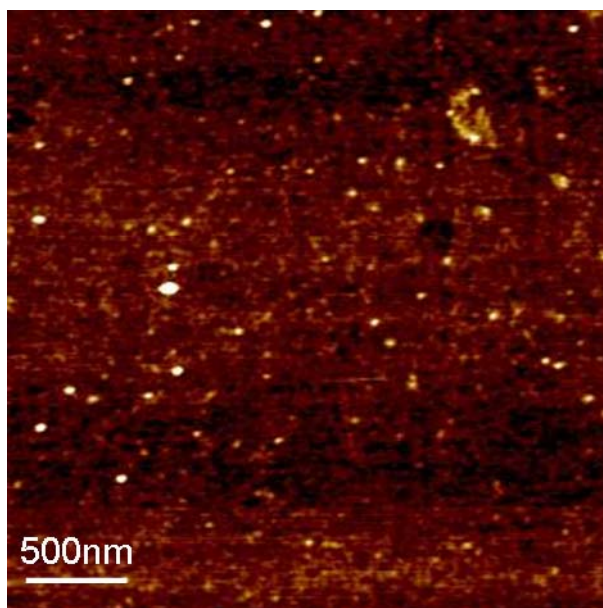


Figure 3-14 An AFM height image in tapping mode of 10mg/mL lysozyme in 10mM glycine buffer at pH 2.0. The Z-range is 9.8 nm.

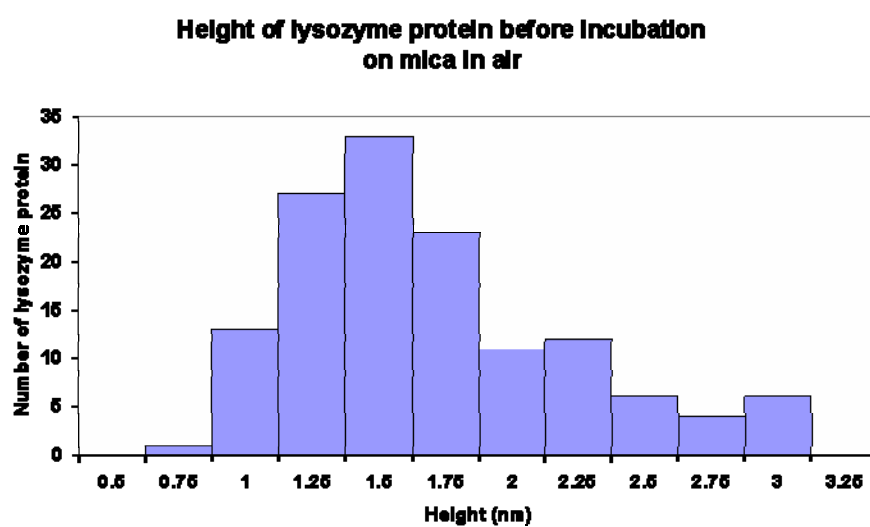


Figure 3-15 Histogram of the height of lysozyme particles before incubation measured from AFM images taken on mica in air. The average height of lysozyme particles was 1.6 ± 0.5 nm ($N = 136$).

3.2.2 The Early Stages of Lysozyme Fibrillization

Samples from different batches were found to have slightly different rates of fibrillization. Highly flexible protofilaments of elongated lysozyme proteins were however always observed after 2 to 3 days of incubation (**Figure 3-16**).

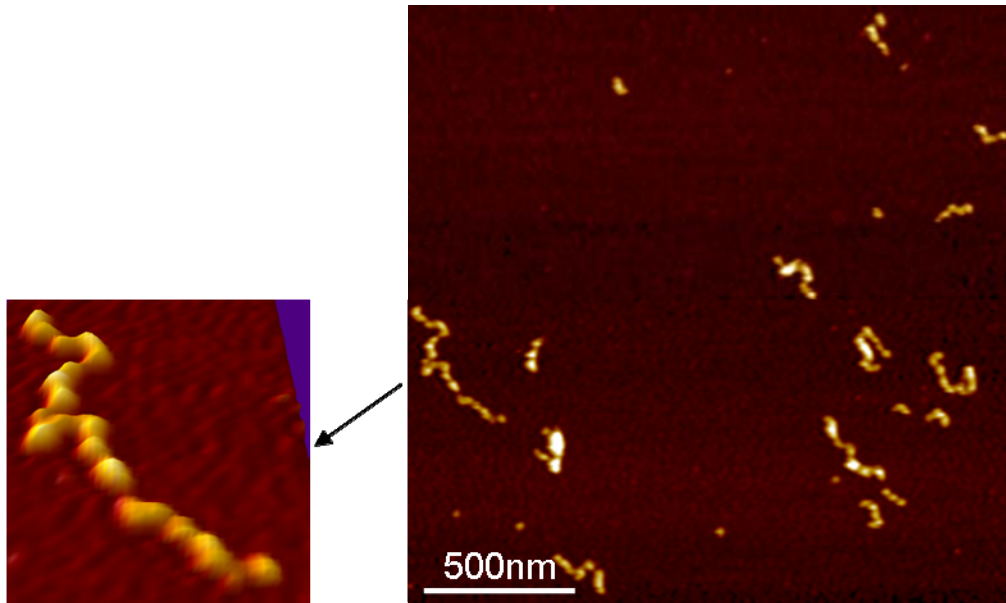


Figure 3-16 An AFM height image of lysozyme after 3 days of incubation. A 3D image (generated by SPIP software) of one protofilament, which is indicated by the black arrow, is displayed on the left. The Z-range is 10.4 nm.

The protofilament appeared to be a chain of single particles (**Figure 3-16**, Jansen *et al.* 2005; Goldsbury *et al.* 2005). The lengths of the protofilaments were from ~80 nm to ~700 nm. The average height of the higher points of the protofilaments was 4.4 ± 0.6 nm; while the average height of the lower points of the protofilaments was 2.9 ± 0.2 nm. Compared to the height of the single lysozyme proteins (1.6 ± 0.5 nm), the elongated particles were ($4.4 / 1.6 =$) 2.8 times in

height. This suggested that lysozyme proteins had undergone a dramatic structural change in order to form protofilaments (Dobson *et al.*, 1998).

After 2 to 3 days of incubation, along with the protofilaments, a few fibrils with clear periodicities began to be observed. One such fibril is shown in **Figure 3-17**. This fibril has a pitch of 85 ± 4 nm, an average height 5.3 ± 0.9 nm with the average height of the higher points 7.0 ± 0.3 nm and average height of the lower points 3.5 ± 0.1 nm (Jansen *et al.* 2005).

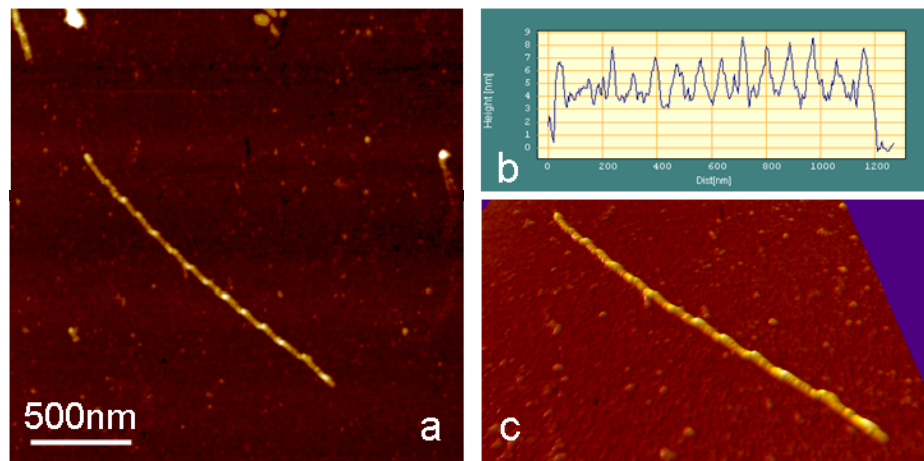


Figure 3-17 AFM image of one lysozyme fibril with clear periodicity after 2 days of incubation; (a) is the height image, (b) is the profile along the axis of the fibril on (a), and (c) is a 3D image of the fibril on (a) generated by SPIP software (see section 2.1.3). The pitch of this fibril is 85 ± 4 nm. The average height of this fibril is 5.3 ± 0.9 nm with the average height of the higher points 7.0 ± 0.3 nm and average height of the lower points 3.5 ± 0.1 nm. The Z-range is 20.5 nm.

3.2.3 The Middle Stages of Fibrillization

Fibrils with distinct branches splaying apart (**Figure 3-18**, indicated by green arrows) were observed after 4 days of incubation. The highly flexible protofilaments (**Figure 3-18**, indicated by blue arrows) have an average height of 2.3 ± 0.2 nm.

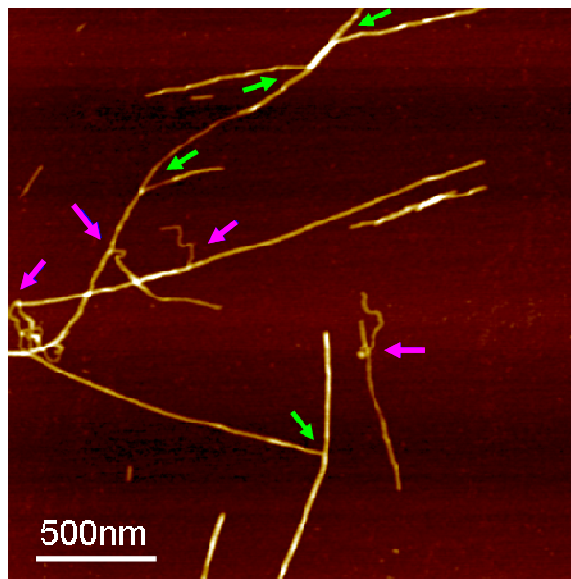


Figure 3-18 AFM height image of lysozyme fibrils after 4 days of incubation. The green arrows indicate fibrils with distinct branches splaying apart. The pink arrows indicate highly flexible protofilaments connected to rigid mature fibrils. The Z-range is 15.9 nm.

Lysozyme fibrils from three different batches on the middle stages of incubation (2 to 10 days) were imaged and categorised according to their heights into 6 types (**Table 3-3**).

As described in section 1.3.1.3, Khurana and co-workers (2003) proposed a general hierarchical assembly model of amyloid fibrils. For example, the assembly model of insulin into amyloid fibrils is as shown in **Figure 3-19**. Two identical subunits intertwine with each other to form fibrils of a higher assembly

level. The subunit can be a protofilament or a fibril consisting of 2 or 4 protofilaments, and the average height of a fibril is $1.5D$ (D is the diameter of the cross section of a subunit), with the height of the higher points $2D$ and the height of the low points D .

Table 3-3 The average heights of 6 types of lysozyme fibrils observed. Types II to VI fibrils have clear periodicity. Type I fibrils did not have clear periodicity.

	Type I	Type II	Type III	Type IV	Type V	Type VI
Average height of higher points (nm)	2.3 ± 0.2	4.5 ± 0.3	5.7 ± 0.1	7.0 ± 0.3	7.2 ± 0.2	10.2 ± 0.2
Average height of lower points (nm)		2.5 ± 0.2	3.8 ± 0.1	3.5 ± 0.2	5.4 ± 0.2	6.0 ± 0.1
N	50	30	30	20	9	6

If the assembly of lysozyme fibrils also followed the same model as in **Figure 3-19**, from the height of lysozyme protofilaments (2.3 ± 0.2 nm), the Type I fibrils, the heights of the fibrils would be predicted as shown in **Table 3-4**.

Compared **Table 3-4** with **Table 3-3**, Type II lysozyme fibrils fit well into “1+1” model; Type IV fibrils fit well into “2+2” model; and Type VI fibrils fit well into “4+4” model. However, other types of fibrils do not fit into Khurana’s model.

As indicated by pink arrows in **Figure 3-18**, highly flexible protofilaments were observed connected to fibrils of different types. This may therefore suggest a new assembly model i.e. an “n+1” model (where n is the number of protofilaments in one subunit) (**Table 3-5**). In other words, a protofilament might intertwine with a fibril already consisting of more than one protofilament (**Figure 3-20**). The average

height of an “n+1” fibril is $(D_n + D_1)/2$ (D_n is the diameter of the cross section of the subunit consisting of more than one protofilaments; D_1 is the diameter of the cross section of one protofilament), with the height of the higher points ($D_n + D_1$) and the height of the lower points D_n .

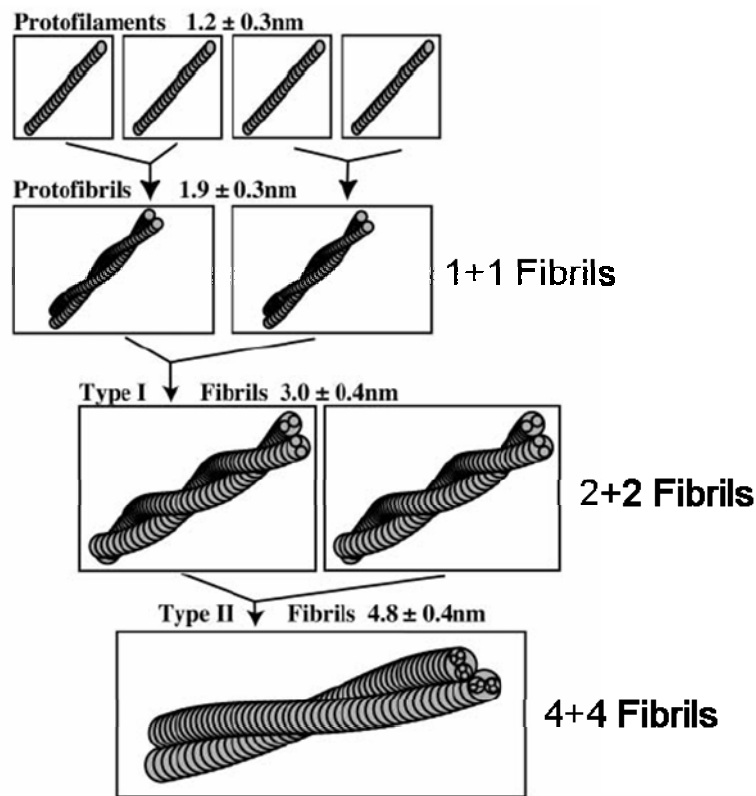


Figure 3-19 A model for the hierarchical assembly of insulin into amyloid fibrils. Protofilament pairs wind together to form “1+1” fibrils, and two “1+1” fibrils wind to form a “2+2” fibril. “4+4” fibrils are the result of winding of two “2+2” fibrils (figure adapted from Khurana 2003).

Table 3-4 The predicated heights using Khurana’s model (2003).

	Protofilaments	1+1 Fibrils	2+2 Fibrils	4+4 Fibrils
Height of higher points (nm)	2.3	4.6	6.9	10.4
Height of lower points (nm)		2.3	3.4	5.2

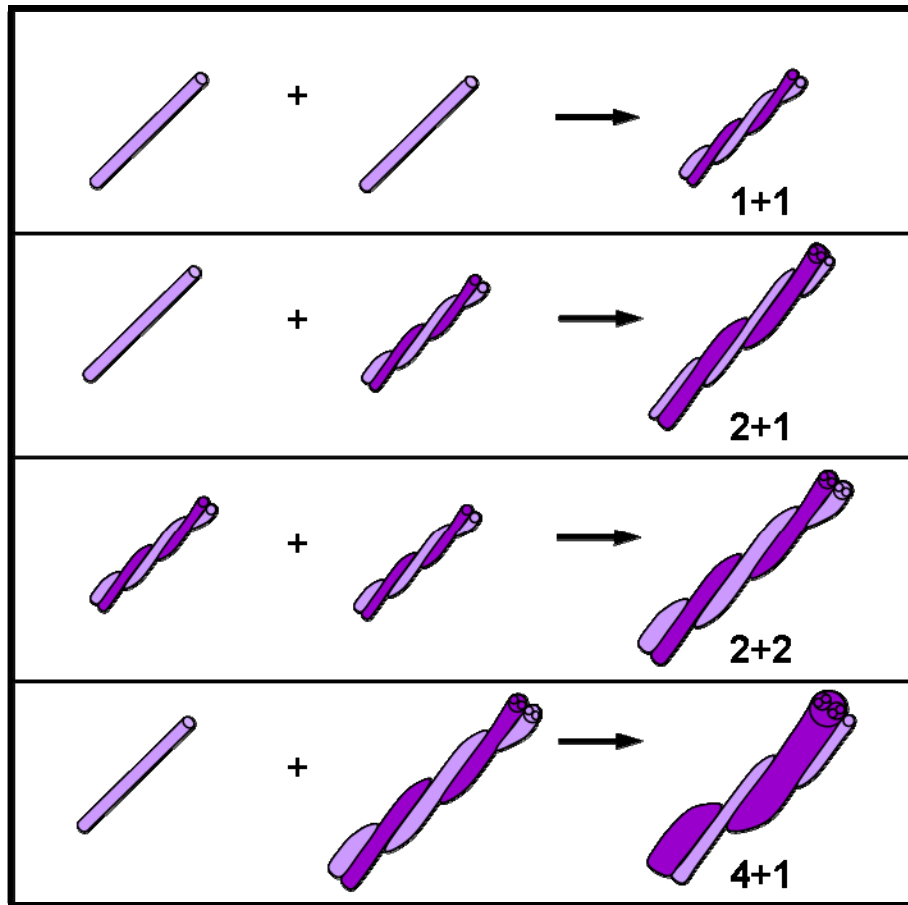


Figure 3-20 “n+1” model for lysozyme fibrils assembly. Protofilaments intertwine with each other to form “1+1” fibrils. Two “1+1” fibrils intertwine into a “2+2” fibril. A protofilament can intertwine with a “1+1” fibril to form a “2+1” fibril or with a “2+2” fibril to form a “4+1” fibril.

Table 3-5 The predicated heights using the “n+1” model.

	Protofilaments	2+1 Fibrils	4+1 Fibrils
Height of higher points (nm)	2.3	5.8	7.5
Height of lower points (nm)		3.4	5.2

Compared with **Table 3-5** with **Table 3-3**, Type III lysozyme fibrils fit well into “2+1” model, and Type V fibrils fit well into “4+1” model. The data is summed up in **Table 3-6** for comparison.

Table 3-6 The summary of the experimental data of the heights of lysozyme fibrils and the heights predicted by Khurana’s model and “n+1” model.

Fibrils model		1+1	2+1	2+2	4+1	4+4
Experimental data	Average height of higher points (nm)	4.5 ± 0.3	5.7 ± 0.1	7.0 ± 0.3	7.2 ± 0.2	10.2 ± 0.2
	Average height of lower points (nm)	2.5 ± 0.2	3.8 ± 0.1	3.5 ± 0.2	5.4 ± 0.2	6.0 ± 0.1
Predicted by model	Height of higher points (nm)	4.6	5.8	6.9	7.5	10.4
	Height of lower points (nm)	2.3	3.4	3.4	5.2	5.2

Note that for the heights of the higher points, the experimental data are 4% less to 2% more than predicated by the model. However, for the heights of the lower points, the experimental data are 3% to 15% more than predicated by the model; especially for the “4+4” fibrils, the experimental data is $((6.0-5.2) / 5.2 =)$ 15% more than predicated by the model. This might be because the fibrils were raised from the mica surface at the lower points due to the stiffness of the fibrils and intertwining, which would increase the height of the lower points measured from the profile of AFM images. Since the stiffness increased with the increasing of the assembly level (a detailed discussion of the elasticity of the lysozyme fibrils will

be presented in section 4.3), the increasing of the height of the lower points of “4+4” fibrils was more observable than other fibrils.

Using both Khurana’s model and “n+1” model, the fibrils observed on AFM images can therefore be explained. An example is given in **Figure 3-21**: a “1+1” fibril intertwines with a protofilaments to form a “2+1” fibril.

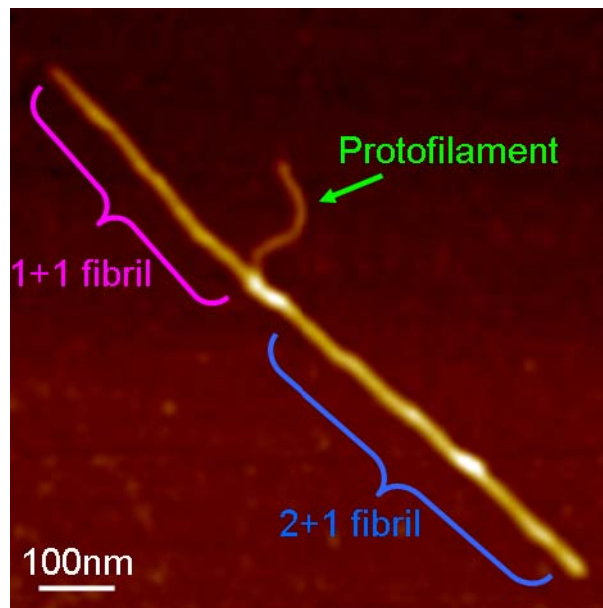


Figure 3-21 An AFM height image of a lysozyme fibril after 4 days of incubation. The fibril indicated by green arrow has height of 2.4 ± 0.1 nm, which could be a protofilament; the fibril indicated by pink bracket has average height of higher points 4.6 ± 0.1 nm and lower points 2.8 ± 0.1 nm, which could be a “1+1” fibril; the fibril indicated by the blue bracket has an average height of higher points 5.5 ± 0.5 nm and lower points 3.5 ± 0.1 nm, which could be a “2+1” fibril. The Z-range is 9.1 nm.

Some fibrils were observed to be connected to more than one fibril (**Figure 3-18**), suggesting that the formation of mature fibrils from the intertwining of subunits

might happen starting from the two ends or even in the middle of the subunits; also that fibrils of different assembly levels might be forming at the same time.

3.2.4 The Late Stages of Lysozyme Fibrillization

After 11 to 14 days of incubation (**Figure 3-22**), the sample solution started to have a gel-like appearance. Most lysozyme fibrils appeared to have clear periodicity with a periodicity to diameter ratio of ~ 20 . Interestingly, some fibrils appeared to have sinusoidal shape (**Figure 3-22**, indicated by pink arrows), which might be due to some degree of unwinding of the subunits created during the adsorption process of the fibrils to the substrate.

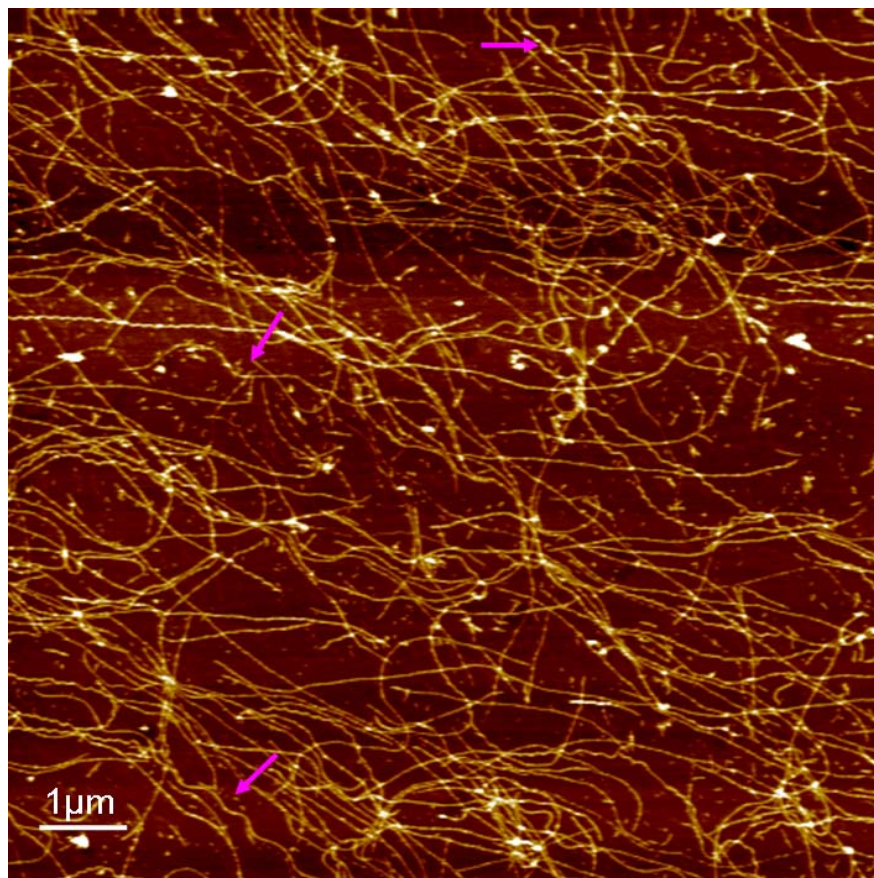


Figure 3-22 An AFM height image of lysozyme fibrils after 11 days of incubation. The pink arrows indicate some fibrils with sinusoidal shape. The Z-range is 26.6 nm.

Circular fibrils, the diameter of which was typically 250~350 nm, were also observed after 14 days of incubation (Figure 3-23).

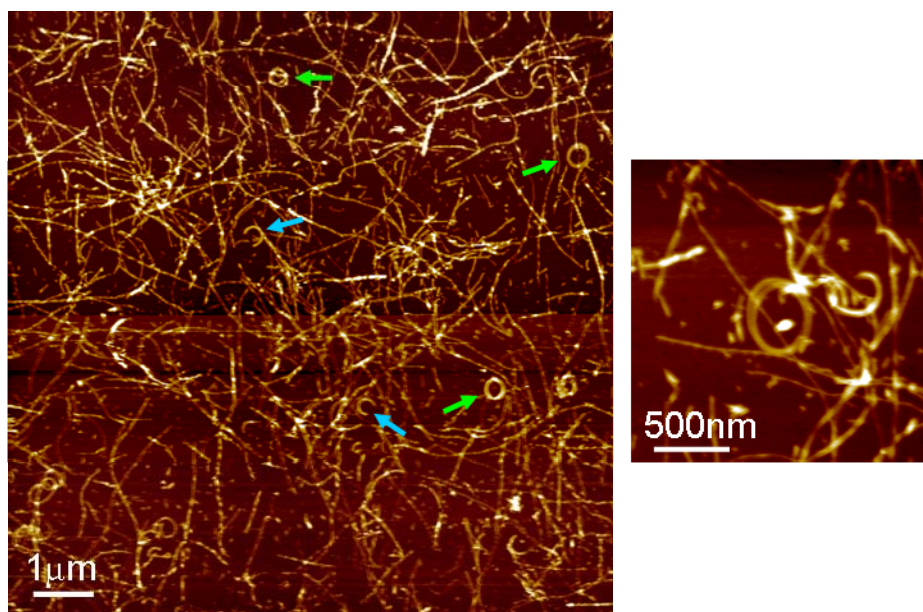


Figure 3-23 AFM height images of lysozyme fibrils after 14 days of incubation. The green arrows indicate several fibrils with circular structures. The blue arrows indicate two fibrils with half circular structures. The image on the right has better resolution, with one circular fibril on the middle. The Z-range of the left image is 24.3 nm.

Previous studies on solvational and hyperbaric tuning of amyloidogenesis with insulin fibrils suggested that circular structures of amyloid fibrils are probably a lower void volume alternative to straight fibrils (Jansen *et al.* 2004; Grudzielanek *et al.* 2005; also see section 1.3.1.3). The fact that the circular structure of lysozyme fibrils were only observed at the late stages of fibrillization when fibrils became “crowded”, agreed with this theory. However, no high hydrostatic pressure and addition of cosolvents or cosolutes were required in this case, which

suggests that simpler conditions could be applied to manipulate the conformation of amyloid fibrils.

3.3 Alternative Assembly of Tubular and Spherical Nanostructures from FF Peptides

The self-assembly of FF peptide monomers into nanotubes happens very rapidly (Reches and Gazit 2003). In order to observe the formation of FF nanotubes, the sample for AFM operation needs therefore to be prepared immediately after the FF nanotubes are formed, so that further self-assembly is interrupted.

FF nanotubes prepared by Reches and Gazit's method (2003), where FF peptide was dissolved in HFIP at high concentrations (100mg/mL) and then diluted into the aqueous solution at a final μM concentration range (for detailed preparation see section 2.2.4), were typically several micrometers in length and 50 to 300 nm in diameter (Figure 3-24). However, short and thin fibrillar structures of 2 to 4 nm in height were also sometimes observed along with the long and thick nanotubes (Figure 3-24). Associating with the tentative model proposed by Görbitz (2006) (see section 1.3.3.2), the long and thick nanotubes may have their proposed multilayer tubular wall, while the short and thin fibrils might well be single-wall nanotubes.

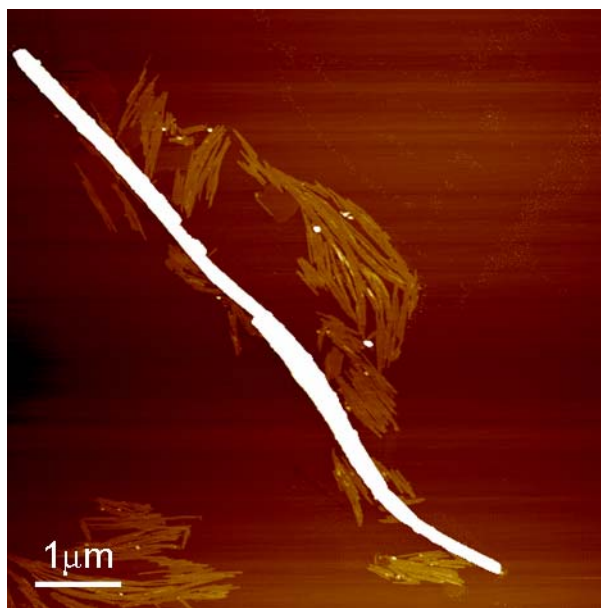


Figure 3-24 AFM image of typical long and thick FF nanotubes along with short and thin fibrillar structures. The long and thick FF nanotubes lying from the top left to the bottom right on the middle of this image is whitened because the colour scale has been adjusted in order to enhance the appearance of the short and thin fibrillar structures. The Z-range is 107.2 nm.

Song and co-workers reported (2004) another nanotube preparation method, where FF peptide was dissolved in water to 2mg/mL at 65 °C, and the sample equilibrated for 30 min and then gradually cooled to room temperature (**Figure 3-25 a**). They noted that when 0.1 mL of the nanotube mixture was diluted by adding 0.1 mL of water, vesicles were present in addition to the nanotubes (**Figure 3-25 b**; also see section 1.3.3.1). Song suggested that the concentration of the peptide is a key factor in the formation of the nanotubes. However, by noticing the presence of vesicles in the SEM image of FF nanotubes before dilution in Song's paper (**Figure 3-25 a**, indicated by pick arrows), I suspected that the temperature might play an important role in the alternative formation of tubular and spherical structures. Bearing this in mind, I used modified Reches and Gazit's (2003)

method to investigate the effect of temperature on the formation of FF nanostructures.

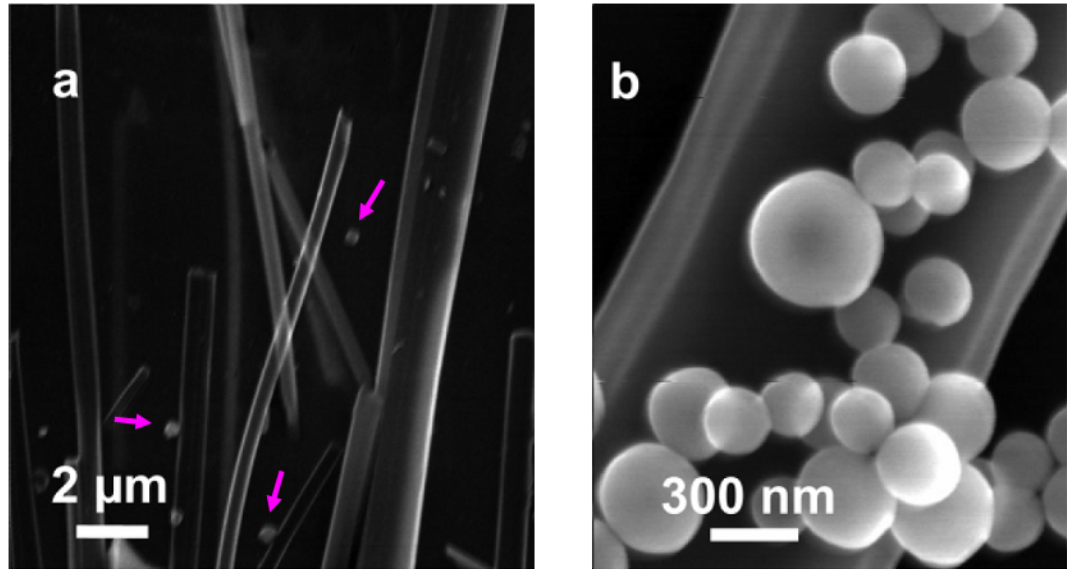


Figure 3-25 SEM images of (a) peptide nanotubes and (b) a mixture of nanotubes and vesicles (figure and caption adapted from Song *et al.* 2003, Fig 1)

FF peptide HFIP stock solution (100mg/mL) and distilled water were pre-warmed in a 40°C water bath. The AFM sample (2mg/mL) was then prepared using this stock solutions and distilled water (detailed preparation see section 2.2.4). An AFM topography image of this sample is displayed in **Figure 3-26**. Spherical structures of 2 to 4 nm in height were observed. Thin fibrillar structures of ~1 nm in height, 200 to 300 nm in length were also observed.

In a similar manner, the FF peptide HFIP stock solution (100mg/mL) and distilled water were pre-warmed in 65°C water bath. The AFM sample (2mg/mL) then prepared using these stock solution and distilled water. An AFM topography

image of this sample is displayed in **Figure 3-27**. Spherical structures of 2 to 4 nm in height were observed. However, no tubular structures were observed.

As stated before, results from original Reches and Gazit's (2003) method had only nanotubes but no spherical structures observed. Comparing the results from modified Reches and Gazit's method, it seemed that the temperature is likely to be a key factor in the alternative assembly of tubular and spherical nanostructures during FF self-assembly. The tubular structures might be kinetically favoured (Reches and Gazit 2004).

Reches and Gazit have also reported (2004) the formation of spherical nanostructures of diphenylglycine peptide, a highly similar analogue of diphenylalanine peptide. Comparing this to the formation of spherical nanostructures of FF peptides, the diphenylglycine peptide might have lower energy barrier to form spherical nanostructures. By controlling the temperature, the formation of tubular structures from diphenylglycine peptide or other analogues of FF peptide might therefore be possible.

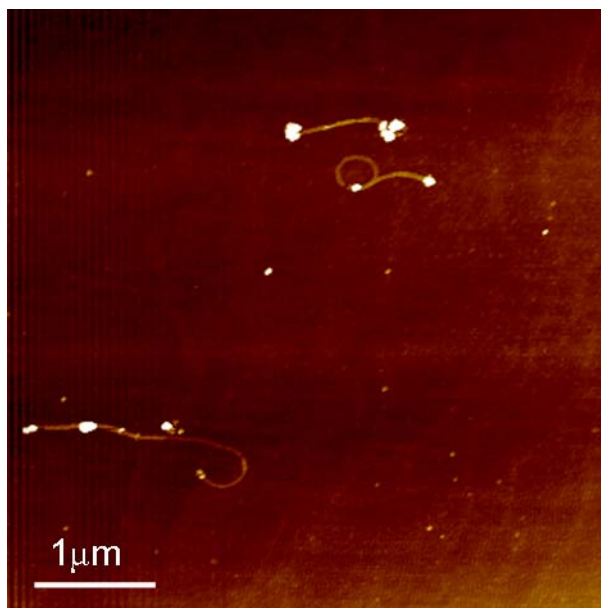


Figure 3-26 An AFM image of FF nanostructures self-assembled at 40°C. A few thin fibrillar structures of ~1 nm in height, 200 to 300 nm in length were observed along with spherical structures of 2 to 4 nm in height. The Z-range is 21.7 nm.

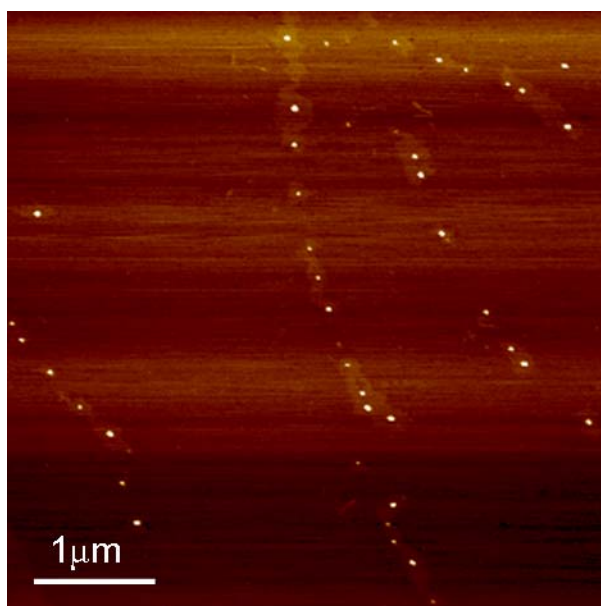


Figure 3-27 An AFM image of FF nanostructures self-assembled at 65°C. Spherical structures of 2 to 4 nm in height were observed. The vesicles lie in lines, which is most likely due to the drying process during sample preparation. The Z-range is 6.2 nm.

3.4 Conclusion

In this chapter, the imaging capability of AFM has been explored and a range of imaging studies monitoring the dynamic processes of protein nanotubes have been presented. A better understanding of the dynamic processes of protein nanotubes, provides the information on manipulating these protein nanotubular materials, which is desired in order to utilize them in applications.

The dissociation process of *Salmonella* flagellar filaments in low pH solution was found to happen within an hour; therefore, real-time monitoring was possible. All parts of a filament exposed to the low pH solution were found to instantly break down to single flagellin proteins at the same time.

If the dynamic process of protein nanotubes occurs on timescales that are too long or too short for real-time AFM monitoring, the process has to be interrupted so that the sample can be prepared for AFM operation. For example, the fibrillization process of lysozyme fibrils takes up to two weeks, while the formation of nanostructures from FF peptides takes only a few seconds to a few minutes.

By observing the fibrillization process of lysozyme fibrils, the “n+1” model has been proposed: a protofilament may intertwine with a fibril consisting of more than one protofilament to form higher assembly level fibrils. This model complements the hierarchical assembly model proposed by Khurana (2003).

The effect of temperature on the alternative formation of tubular and spherical nanostructures of FF peptides was also investigated, which may suggest a general way of controlling the formation of nanostructures from FF peptides and its similar analogues.

Chapter 4 Persistence Length Study of Protein Nanotubes

From Chapter 4 to Chapter 6, I will present the different approaches which were employed to access the physical properties of protein nanotubes using AFM. In this chapter, a persistence length method will be applied on three different nanotubes. Persistence length is a mechanical property quantifying the flexibility of a filament, in this case a protein nanotube, which provides an indication of how much a filament “persists” in its initial orientation. Associating the geometry of the cross section of the filament studied, the elasticity of the filament is also able to be estimated.

4.1 Theory and Method

4.1.1 Persistence Length is a Measure of the Flexibility of a Filament

The definition of persistence length is “the average projection of the end-to-end vector on the tangent to the chain contour at a chain end in the limit of infinite chain length” (IUPAC Gold Book). Considering a filament as succession of segment vectors of length l , as demonstrated in **Figure 4-1**, the angle between the end-to-end vector from position 0 to position 1 and the tangent vector at position 0 is θ . The projection of the end-to-end vector on the tangent vector is $l\cos\theta$. The average of this projection is $l\langle\cos\theta\rangle$ ($\langle\rangle$ denotes the average). If the contour

length of the filament becomes sufficiently long, consequently the number of segments becomes sufficiently large, the average projection approaches a constant value, which is termed the persistence length P (Equation 4-1).

$$\langle \cos \theta \rangle = e^{-(l/P)}$$

Equation 4-1

In other words, the persistence length is the length over which correlations in the segment directions are lost. The expectation value of the cosine of the angle falls off exponentially with distance. A more detailed explanation of persistence length can be found in Frontali's (1979) and Hagerman's (1988) work.

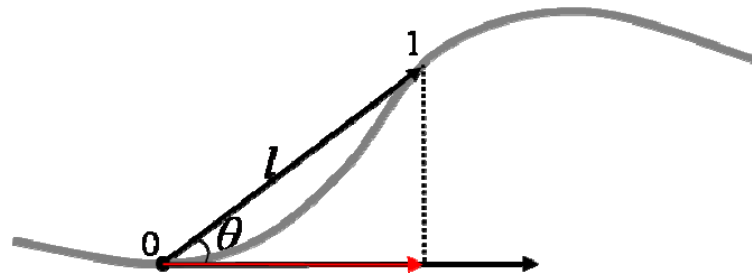


Figure 4-1 A sketch of a thin flexible filament. The segment vector from position 0 to position 1, the tangent vector at position 0, and the angle θ between these two vectors are shown. The projection of the segment vector on the tangent vector is shown by a red arrow.

Persistence length is independent of the contour length of the filament (Hagerman, 1988). However, the persistence length is related to the end-to-end distance of the filament. The relation between the mean-square end-to-end distance R and the persistence length P is given by Equation 4-2 (Flory 1969; Rivetti *et al.* 1996).

$$\langle R^2 \rangle = 4Ps \left[1 - \frac{2P}{s} (1 - e^{-s/2P}) \right]$$

Equation 4-2

where s is the contour length of the filament.

The persistence length is a measure of the flexibility of a filament. The higher the persistence length, the more rigid the filament; the lower the persistence length, the more flexible it is. The flexibility of a filament is related to its elasticity through **Equation 4-3** (Landau and Lifshitz 1980; 1986).

$$EI = k_B TP$$

Equation 4-3

where E is the Young's modulus, I is the area moment of inertia of the cross section of the filament ($I = \pi D^4/64$, for a circular area with diameter D), k_B is the Boltzmann constant and T is the absolute temperature. If the persistence length of the filament can be obtained from AFM images, together with the geometry of the cross section, the Young's modulus can therefore be estimated.

4.1.2 Analysing AFM Images of Nanofibrils and Nanotubes to Obtain Their Persistence Lengths

AFM images of nanofibrils or nanotubes were analysed using Veca, an image processing software developed by A. Orta (LBSA, University of Nottingham, UK). The analysis process is as follows:

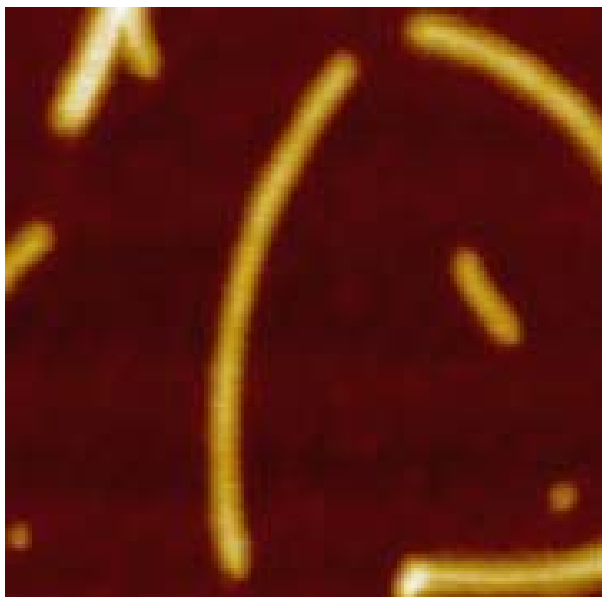


Figure 4-2 An AFM tapping mode height image of *Salmonella* flagellar filaments observed on mica in air. The size of the image is 1 μm×1 μm. The filament of interest is the long filament lying approximately vertically on the middle of this image.

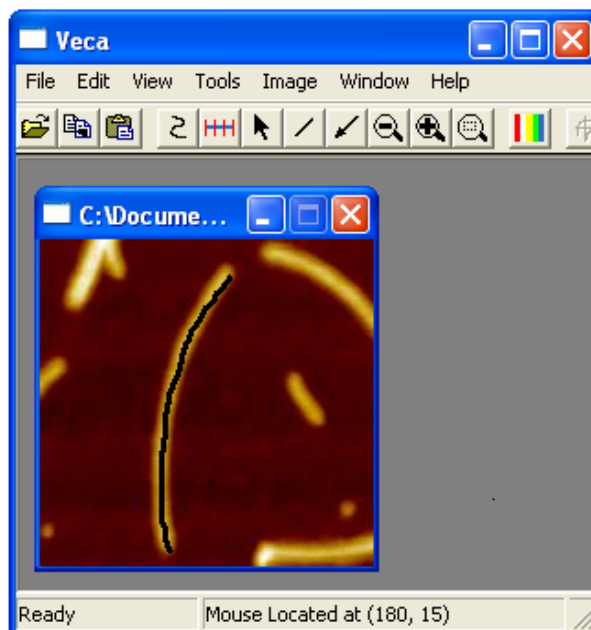


Figure 4-3 Use of “Freehand” tool to trace the contour of a filament within Veca. The layout of Veca is shown. The AFM image of **Figure 4-2** is open inside of Veca. The black line along the filament is the trace line drawn with the mouse using the “Freehand” tool of Veca.

First, AFM height images were exported from SPIP software (**Figure 4-2**) (see section 2.1.3 for the details of using SPIP software). After calibration of the scale, the contours of nanofibrils or nanotubes were traced using the “Freehand” tool within the Veca software. The layout of Veca is displayed in **Figure 4-3**.

Second, the contour of the filament then was digitalised and recorded as a set of XY-coordinate by Veca. In order to minimise experimental data acquisition errors, a smoothing procedure using the weighted average of five contiguous XY-coordinates centred about a given XY-coordinate was performed (Mucke *et al.* 2004).

$$V_{i,correct} = \frac{1V_{i-2} + 2V_{i-1} + 4V_i + 2V_{i+1} + 1V_{i+2}}{10}$$

Equation 4-4

where V_i is the vector of the tangent to the curve on XY-coordinate i . This procedure removes two points at each end of the filament. The smoothed XY-coordinates of the filament shown in **Figure 4-2** are displayed in **Figure 4-4**.

Third, **Equation 4-1** or **Equation 4-2** was used to compute the persistence length. If **Equation 4-1** was used, the filament contour was split into segments of increasing segment length l , and for each set of segment length, the mean cosine angle $\langle \cos \theta \rangle$ and the persistence length P calculated. The persistence length was then plotted as a function of contour segment length l (**Figure 4-5**). A clear maximum value of persistence length P_0 was discerned using this method, which corresponding to the value of the persistence length of the filament.

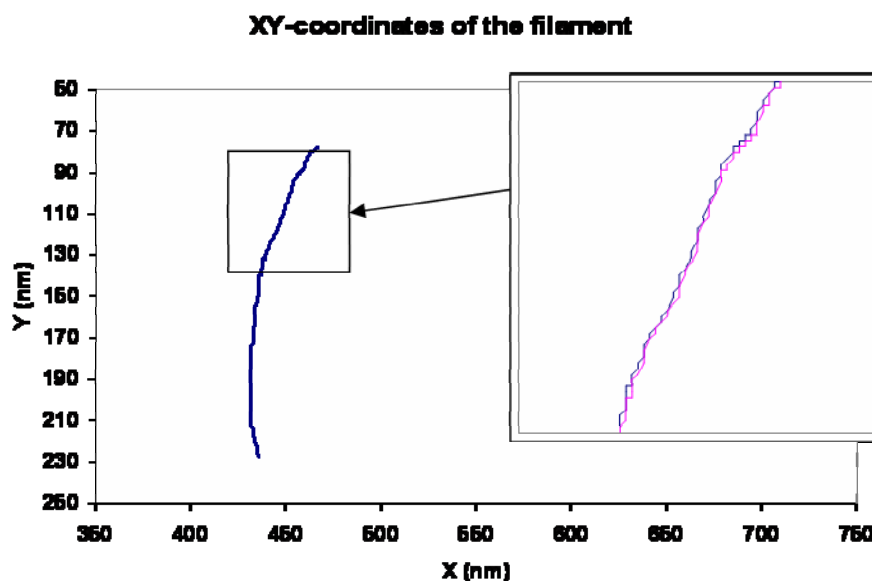


Figure 4-4 The contour of the filament shown in **Figure 4-2** is digitalised to XY-coordinate sets here. The blue curve is plotted with smoothed XY-coordinates. The part enclosed by the square is enlarged and shown on the inset. The pink curve on the inset is plotted with the original XY-coordinates before smoothing.

As shown in **Figure 4-5**, the value of persistence length typically was found to decrease at lower and higher contour segment length l . At lower l , the discretization during data processing results in an underestimation of persistence length. At higher l , the small angles are overlooked; therefore the number of small angles is undercounted, which leads to underestimation of persistence length as well.

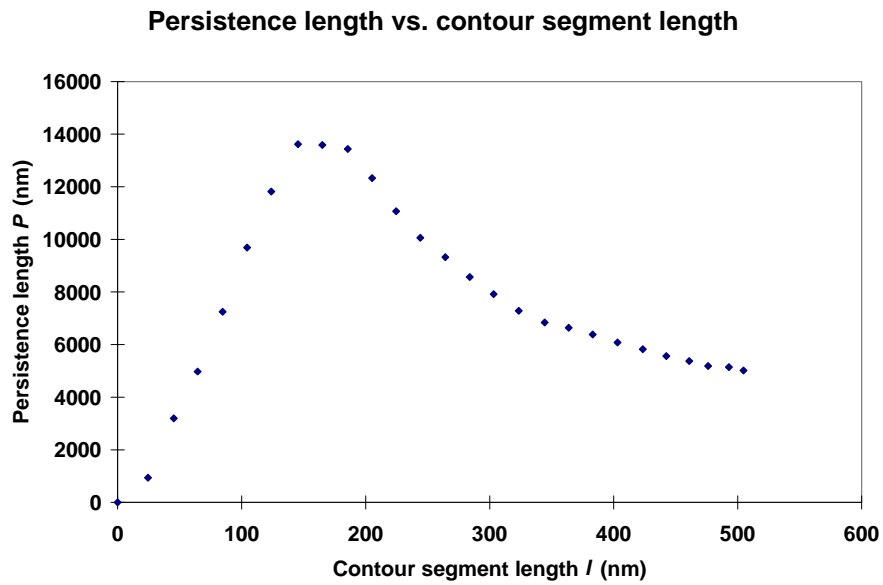


Figure 4-5 Persistence length P against contour segment length l . A peak value of persistence length $P_0 = 13.6 \mu\text{m}$ in the range $l = 120 \text{ nm}$ to 200 nm can be discerned, which is the value of persistence length of the filament shown on **Figure 4-2**.

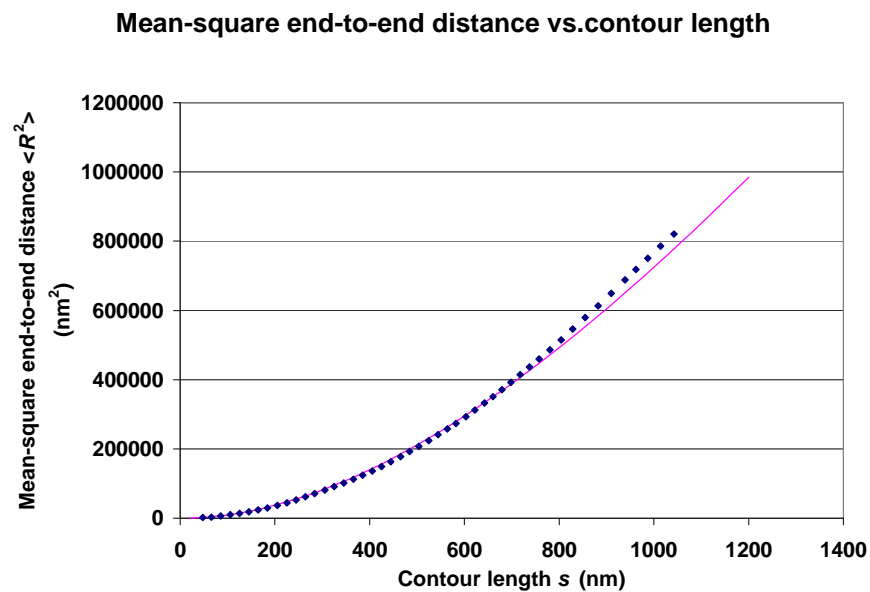


Figure 4-6 The plot of the mean square end-to-end distance $\langle R^2 \rangle$ against the contour length s of the filament on **Figure 4-2**. The pink line is the fitted curve using the Levenberg-Marquardt algorithm (Press *et al.* 1992). The persistence length computed for this filament is $P_R = 474 \text{ nm}$.

If **Equation 4-2** was used, the filament was split into segments of increasing contour length s , and for each set of contour lengths, the mean-square end-to-end distance $\langle R^2 \rangle$ calculated. The mean-square end-to-end distance was then plotted against the contour length s . The experimental data then is fitted into **Equation 4-3** to obtain the persistence length P_R , using the Levenberg-Marquardt algorithm (Press *et al.* 1992).

4.2 The Persistence Length of Flagellar Filaments in Different Environments

As discussed in section 3.1, *Salmonella* flagellar filaments were imaged under different conditions in order to investigate the effects of the environment on their structures. Here, in order to investigate the environmental effect on their elastic properties, the topography images obtained in section 3.1 (e.g. **Figure 3-1**, **Figure 3-10** and **Figure 3-11**) were used to compute the persistence length.

Although images of *Salmonella* flagellar filaments on mica in aqueous environments have been obtained, imaging in aqueous environments is difficult to operate and time consuming. As bulk data was needed for persistence length calculation, images of *Salmonella* flagellar filaments on mica in air (see section 3.1.1) were used to obtain persistence length. The limited on mica in liquid images obtained (see section 3.1.2) agreed with the on mica in air persistence length results.

A typical data analysis of a *Salmonella* flagellar filament obtained by applying **Equation 4-1** is displayed in **Figure 4-5**. The peak values of persistence length obtained in my experiments lied between $l = 100$ nm to 200 nm. As explained

above (section 4.1), underestimation of persistence length at lower l values is expected. Therefore only filaments with contour length longer than 400 nm were selected for measuring persistence length. This selection rule also had an advantage of giving a clear peak value of persistence length in the chart of persistence length versus contour segment length. The persistence length of *Salmonella* flagellar filaments on mica in air obtained was $P_0 = 11 \pm 2 \mu\text{m}$.

A typical data analysis of a *Salmonella* flagellar filament through the application of Equation 4-2 is displayed in Figure 4-6. The persistence length of *Salmonella* flagellar filaments on mica in air was found to be $P_R = 0.46 \pm 0.08 \mu\text{m}$. The distribution of P_R is displayed in Figure 4-7.

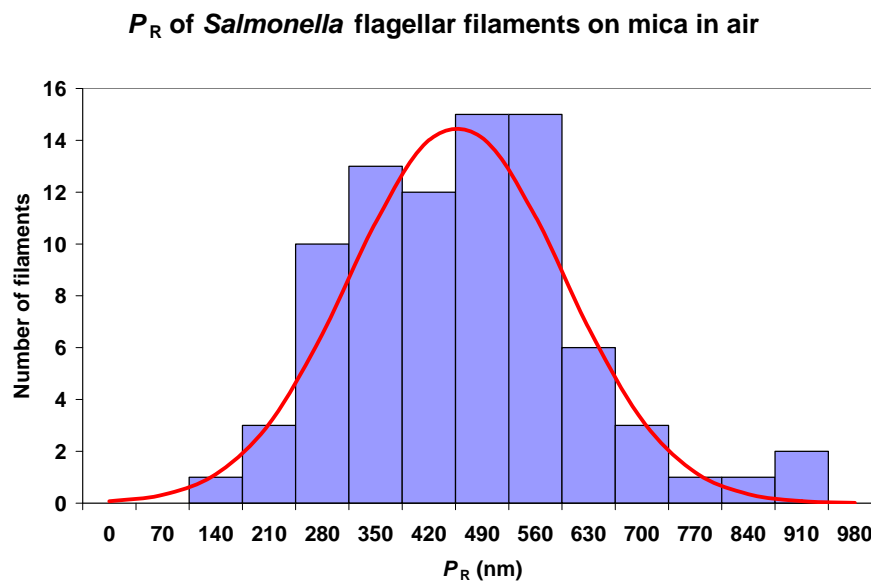


Figure 4-7 Histogram of the persistence length obtained for *Salmonella* flagellar filaments on mica in air through the application of Equation 4-2. The mean persistence length measured was found to be $P_R = 0.46 \pm 0.08 \mu\text{m}$ ($N = 82$).

The topography images of *Salmonella* flagellar filaments on gold in air and in propanol-water (80:20) mixture obtained in section 3.1.3 were also used to compute persistence length.

Salmonella flagellar filaments were found to be broken over the gaps between the gold islands of gold substrates (indicated by a blue arrow in **Figure 4-8** (left)). This is most likely due to the drying process during sample preparation, and/or by the force applied by the AFM probe during scanning. The two pink arrows in **Figure 4-8** (left) indicate the ends of two filaments which lie down over the edge of a gold island. This can be observed more clearly in the 3D picture (**Figure 4-8** (right), also indicated by two pink arrows). In addition to the selection rule described above, which was employed to select the filaments with contour lengths over 400 nm, another selection rule was applied for on gold analysis, which was that only those filaments or part of the filaments lying upon one plateau were selected for measurement persistence length.

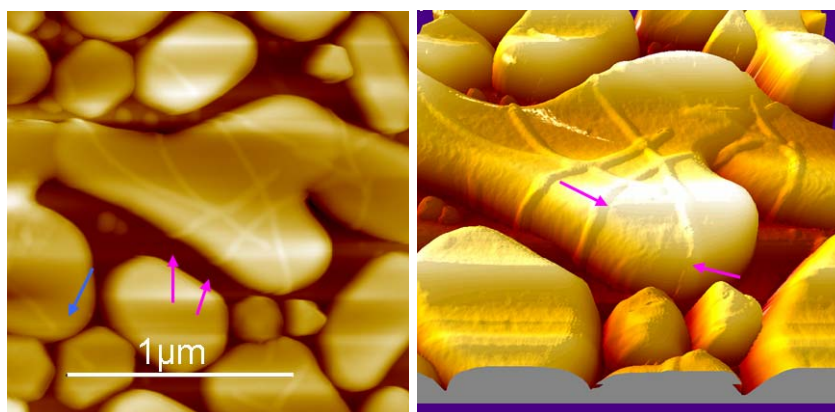


Figure 4-8 Tapping mode AFM height image of *Salmonella* flagellar filaments in air on gold. The right picture is a 3-D picture of the left image generated by SPIP software. Stock sample solutions were 100 times diluted. The Z-scale is 240.0 nm.

In a similar manner, the persistence length for *Salmonella* flagellar filaments on gold in air was found to be $P_{\theta} = 13 \pm 3 \mu\text{m}$ and $P_R = 0.20 \pm 0.05 \mu\text{m}$. The persistence length of the *Salmonella* flagellar filaments imaged on gold in propanol-water (80:20) mixture were found to be $P_{\theta} = 4.1 \pm 0.4 \mu\text{m}$ and $P_R = 0.19 \pm 0.04 \mu\text{m}$.

The average persistence lengths (P_R , P_{θ}) of *Salmonella* flagellar filaments on mica and gold in air, and on gold in propanol-water mixture are displayed in **Table 4-1**.

Table 4-1 *Salmonella* flagellar filaments in different environments.

Environment		On mica	On gold	
		In air	In air	In 80% propanol
Persistence length	P_R (μm)	0.46 ± 0.08	0.20 ± 0.05	0.19 ± 0.04
	P_{θ} (μm)	11 ± 2	13 ± 3	4.1 ± 0.4
P_R/P_{θ}		4.2%	1.5%	4.6%

AFM images of the filaments showed the contour of the filaments transformed from three dimensional (3D) to two dimensional (2D) surfaces. If the energy of the interaction between the filaments and the substrate was in the range of the thermal energy, the filaments would be able to freely equilibrate on the substrate prior to adsorption, and the elastic properties would be conserved during the adsorption process. In this case, the value of the persistence length obtained in 2D is identical to the persistence length of the same filament in 3D (Mücke *et al.* 2004).

However, if the energy of the interaction between the filaments and the substrate is bigger than the thermal energy, the filaments would be kinetically trapped by the support before having equilibrated. In this case, the persistence length of the filaments in 2D will yield a smaller apparent persistence length, which depends on the surface adsorption mechanism (Mücke *et al.* 2004).

As displayed in **Table 4-1**, in all the environments that have been investigated, the persistence lengths (P_R) obtained by applying **Equation 4-2** were less than 5% of the persistence lengths (P_θ) obtained by applying **Equation 4-1**. One way to explain this could be, the kinetics of trapping, which likely initiates through the pinning of a few arbitrary points of the filament to the substrate and proceeds by the adsorption of the intermediate parts of the molecule. This suggests that the use of a global property such as end-to-end distance R to deduce persistence length may lead to an underestimation of the value of persistence length (Abels *et al.* 2006). However, assuming during kinetic trapping the angular distribution of the filament in 3D is preserved and the mechanical information is transferred onto the 2D plane, using local properties such as angle θ may obtain a more accurate value of persistence length.

The values of persistence length obtained above agreed with the persistence length obtained by Trachtenberg and Hammel (1992), which was from 4.5 to 41.14 μm . Using the persistence length obtained on gold in air ($13 \pm 3 \mu\text{m}$), the Young's modulus of *Salmonella* flagellar filaments could be estimated (**Equation 4-3**), which was $E = 22 \pm 4 \text{ MPa}$.

4.3 Change of Flexibility during Fibrillization of Lysozyme Fibrils

The fibrillization process of lysozyme fibrils was visualised using AFM (see section 3.2). Under certain conditions, lysozyme proteins were found to self-assemble from single proteins to protofilaments, and then the protofilaments intertwine with each other to form mature fibrils. An “n+1” model has been proposed to complete Khurana’s model (2003) to explain the hierarchical assembly levels of lysozyme (see section 3.2 for a detailed explanation of the fibrillization pathway).

Table 4-2 Persistence length of lysozyme protofilaments and fibrils of different assembly levels during fibrillization.

Models	Protofilaments	Fibrils				
		1+1	2+1	2+2	4+1	4+4
Persistence length P_{θ} (μm)	0.42 ± 0.07	16 ± 2	25 ± 3	28 ± 3	29 ± 3	52 ± 4
Young’s modulus E (GPa)	1.3 ± 0.6	8.9 ± 1.0	4.1 ± 0.8	3.1 ± 0.9	1.5 ± 0.3	1.0 ± 0.1

The fibril models are explained in detail in section 3.2. For example, lysozyme proteins self-assemble to protofilaments; two protofilaments intertwine with each other to form a “1+1” fibril; two “1+1” fibrils intertwine with each other to form a “2+2” fibril; a “1+1” fibril intertwine with a protofilament to form a “2+1” fibril; etc. The Young’s modulus E was obtained by bringing P_{θ} into **Equation 4-3**.

In order to obtain elasticity information during the fibrillization process for lysozyme fibrils, the persistence lengths were computed from the same AFM

topography images obtained to monitor structural changes during fibrillization (e.g. **Figure 3-16** and **Figure 3-18**; see section 3.2). Lysozyme protofilaments or fibrils were categorised by their heights, then through the application of **Equation 4-1**, their persistence lengths were obtained (see section 4.1). All calculated persistence lengths are displayed in **Table 4-2**.

The persistence length of a “1+1” fibril, which is the fibril composed of two protofilaments intertwining with each other, was found to be $16 \pm 2 \mu\text{m}$ (**Table 4-2**), which was 38 times of the persistence length of the protofilaments ($0.42 \pm 0.07 \mu\text{m}$) (**Table 4-2**). However, the persistence lengths of fibrils of different assembly levels were all found to be of the same order of magnitude. The persistence length of the “4+4” fibrils, which is that of the highest assembly level observed, was found to be $52 \pm 4 \mu\text{m}$, only 3 times the persistence length of the “1+1” fibrils. By bringing the persistence lengths into **Equation 4-3**, the Young’s moduli E were calculated (**Table 4-2**). Although the persistence length increased with the increasing of the assembly level, the Young’s modulus only increased from the protofilaments to “1+1” fibril, and then the Young’s modulus actually decreased with the increasing of the assembly level from “1+1” fibril to “4+4” fibril. In other words, the higher the assembly level of the fibrils, the less flexible the lysozyme fibrils appear to be, but the softer the fibrils are.

Gere stated in his book “Mechanics of Materials” (2004) about the elasticity of cables, which are constructed from wires wound together. “Under the same tensile load, the elongation of a cable is greater than the elongation of a solid bar of the same material and same metallic cross-sectional area, because the wires in a cable “tighten up” in the same manner as the fibers in a rope. Thus, the modulus of

elasticity (Young's modulus) of a cable is less than the modulus of the material of which it is made."

Assuming a lysozyme fibril is constructed from fibrils of a lower assembly level intertwined together, in the similar manner as a cable constructed from wires, the Young's modulus of this fibril could be less than the Young's modulus of the fibrils of the lower assembly level from which this fibril constructed. For instance, the "2+2" fibril is constructed from two "1+1" fibrils, and the Young's modulus of "2+2" fibril is 3.1 ± 0.9 GPa (Table 4-2), which is lower than the Young's modulus of "1+1" fibril (8.9 ± 1.0 GPa). The "4+4" fibril is constructed from two "2+2" fibrils, and the Young's modulus of "4+4" fibril is 1.0 ± 0.1 GPa, which is even lower than the Young's modulus of "2+2" fibril (3.1 ± 0.9 GPa). However, the Young's modulus of a protofilament is 1.3 ± 0.6 GPa, which is only ~15% of the Young's modulus of "1+1" fibril (8.9 ± 1.0 GPa). The intertwining of protofilaments to form a "1+1" fibril, seemed however to increase the Young's modulus. A reason could be that protofilaments do not simply intertwine with each other to form "1+1" fibrils; instead, protofilaments might undergo some structural change, in order to form "1+1" fibrils; which results the increasing of Young's modulus from protofilaments to "1+1" fibrils.

The average Young's modulus of protofilaments and fibrils of different assembly levels was found to be 3.3 GPa, which is consistent with that reported for insulin fibrils 3.3 GPa (Smith *et al.* 2006). Smith and co-workers obtained this 3.3 GPa value as an average value of insulin fibrils without specifying their assembly level.

4.4 Flexibility of diphenylalanine Fibrils

The diphenylalanine fibrils (FF fibrils) were found to range from several micrometers to over 100 μm in length (Reches and Gazit's 2003; Song *et al.* 2004). AFM images of FF fibrils on mica surface were obtained using a Nanoscope multimode AFM equipped with a J-scanner (Veeco, Santa Barbara, CA, USA), which has a maximum X-Y scan size $120 \times 120 \mu\text{m}^2$ (data sheet is available to download on manufacturer's website <http://veeco.com/>). However, with large X-Y scan sizes, or X-Y scan size close to the maximum, drift artefacts become common on AFM images (West and Starostina n.d.). A typical AFM image of FF fibrils taken during my experiments had X-Y scan size $10 \times 10 \mu\text{m}^2$ to $50 \times 50 \mu\text{m}^2$, and therefore most of the FF fibrils observed under AFM imaging exceeded the X-Y scan size. In other words, an AFM image could only capture fragment of a FF fibril, or fragments of FF fibrils. The obtained AFM images, most fragments of FF fibrils appeared to be "straight" and have infinite persistence length. Only a few fibrils with thinner diameter (40 to 50 nm in height) were captured with their whole length on one AFM image. Those fibrils were used to compute the persistence length and the Young's modulus.

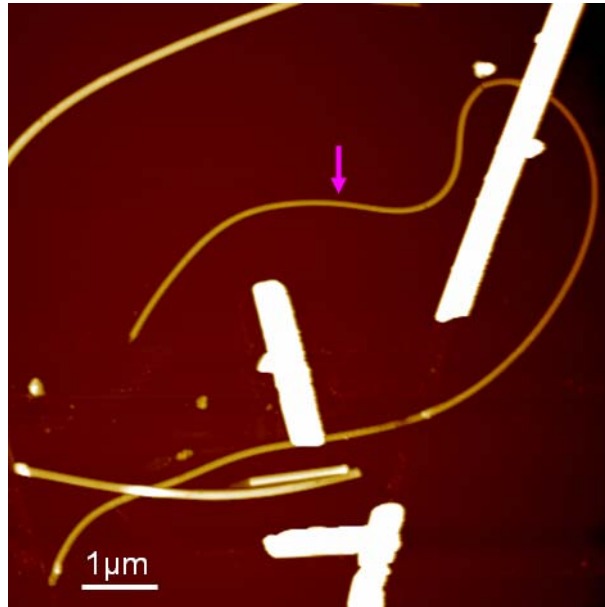


Figure 4-9 AFM image of FF nanotubes. The nanotubes indicated by a pink arrow is 40 ± 1 nm in height and has a persistence length P_0 22 ± 2 μm . The Z-range is 441.4 nm.

A FF fibril with thinner diameter is shown in **Figure 4-9** (indicated by a pink arrow). The height of this fibril is 40 ± 1 nm. The persistence length P_0 is 22 ± 2 μm . Using this persistence length, the Young's modulus of this fibril was computed 0.8 ± 0.2 MPa. This value is much smaller than the value of the Young's modulus obtained by Kol and co-workers (2005), which was ~ 19 GPa. Kol and co-workers studied FF fibrils with diameters ranging from 150 to 300 nm, and noted that the diameter of FF fibrils had no apparent effect on the elasticity of FF fibrils. One possible reason could be the effect of the diameter of FF fibrils on their elasticity falls off with the increasing of the diameter. In other words, within a lower diameter range (e.g. 40 to 150 nm), the elasticity of FF fibrils increases rapidly from MPa to GPa; within higher diameter range (e.g. 150 nm to 300 nm), the effect of the diameter on the elasticity of FF fibrils is within the experimental error. Unfortunately, as explained above, the persistence length method as a

means to calculate elasticity is not suitable for FF fibrils with bigger diameters. Therefore, a full assessment of the relation between the elasticity and the diameter of FF fibrils could not be achieved with the persistence length method (see section 6.3.1 for comparison).

4.5 Conclusion

Persistence length is a measure of the flexibility of a filamentous structure. If the geometry of the cross section of the filament is known, its Young's modulus of this filament can be obtained. AFM topography images of such structures show the contour of the filaments transformed from three dimensional to two dimensional surfaces. By analysing AFM images, the persistence lengths of filaments can be obtained.

In this chapter, the work of achieving the Young's moduli of *Salmonella* flagellar filaments, lysozyme fibrils and FF fibrils through measurement of persistence length has been presented. On gold surfaces and imaged in air, *Salmonella* flagellar filaments were found to have a persistence length of 13 μm , lysozyme fibrils of different assembly levels had a persistence lengths from 16 to 52 μm , and thin FF fibrils had a persistence length of 22 μm . Accordingly, *Salmonella* flagellar filaments have a Young's modulus 22 MPa, lysozyme fibrils an average Young's modulus 3.3 GPa, and thin FF fibrils a Young's modulus 0.8 MPa.

As limited by the range of scan size and the resolution of AFM imaging, the persistence length method presented here is not suitable for nanotubes or fibrils with too high or too low persistence length. The major errors of the persistence length methods include: the underestimation of the persistence length caused by

the transformation of nanotubes or fibrils from 3D to a 2D plane; the inaccuracy in determination of the diameter of the cross section of nanotubes or fibrils for calculation of the Young's modulus.

Chapter 5 Using the Adhesive Interaction between AFM Tips and Sample Surfaces to Measure the Elasticity of Protein Nanotubes

The adhesive interaction between the AFM tips and the sample surfaces can be used to provide the elastic information about the sample (Sun *et al.* 2004). Unlike indentation methods (Kol *et al.* 2005), this technique does not require location of the tip onto the centre of a protein nanotube and also minimises interference from the substrate (Akhremitchev and Walker 1999). In this chapter, the effect of the ionic strength on the elasticity of *Salmonella* flagellar filaments was investigated using the adhesive interaction method.

5.1 Theory and Method

5.1.1 The JKR (Johnson, Kendall and Roberts) Model

When an AFM tip approaches a soft sample, the adhesive force can draw the tip into the sample; when the AFM tip retracts from the soft sample, the tip can also pull the sample up because of the adhesive force (Sun *et al.* 2004). Considering the AFM tip as a sphere and using a spring to represent the AFM cantilever, the adhesive interaction between the AFM tip and a soft sample is shown in **Figure 5-1 (a)**. A typical force-versus-indentation curve is also shown in **Figure 5-1 (b)**.

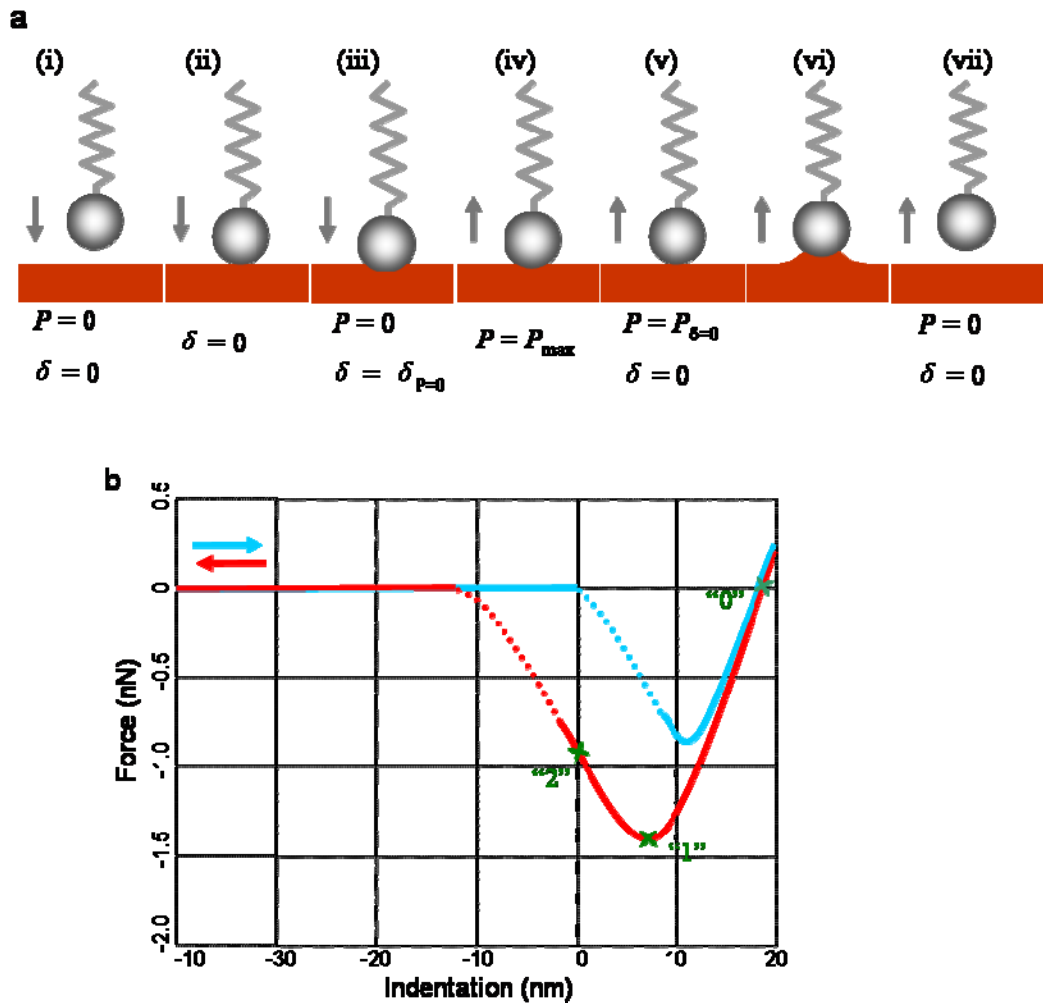


Figure 5-1 The adhesive interaction between the AFM tip and the sample. In (a), the AFM tip is represented as a sphere and the spring represents the AFM cantilever. The sequence shows: the AFM tip approaches (i) and contacts (ii) the sample; then the tip is drawn into the sample by the adhesive interaction (iii); when the tip retracts from the sample (iv, v), the sample will be pulled up by the adhesive force (vi) before it finally ruptures from the sample (vii). A typical force-versus-indentation curve is shown in (b). The blue curve is the approaching curve and the red curve is the retracting curve. On the retracting curve, point “0”, “1” and “2” are the moments represented on (iii), (iv) and (v), respectively (Sun *et al.* 2004).

The details of how to obtain a force-versus-indentation curve and how to define the zero indentation point is explained in section 2.1.1.3. Upon approach, the tip

jumps into contact with the sample surface at the point of mechanical instability, when the gradient of the interaction force exceeds the force constant of the cantilever. Once the tip contacts the surface, the tip is pulled into the sample by the adhesive interaction. At point “0” (**Figure 5-1** (a, iii) and (b)), there is zero external force on the AFM cantilever; the indentation of the sample is purely due to the adhesive interaction; and the stored elastic energy and the surface energy are balanced. At point “1” (**Figure 5-1** (a, iv) and (b)), the tip has a maximum external force. At point “2” (**Figure 5-1** (a, v) and (b)), the indentation is zero. Upon retraction of the tip from the sample, the tip pulls up the sample, and eventually becomes detached from the sample surface.

If the AFM tip and the sample are both treated as spheres and the radius a of the contact area is small (much smaller than both of the sphere radii), a theory proposed by Johnson, Kendall and Roberts (JKR theory) (1971) can be applied. The relationship between the external load P and the contact radius a , and the relationship between the indentation δ of the sample and the contact radius a are given by **Equation 5-1** and **Equation 5-2**, respectively.

$$a^3 = \frac{R}{K} \left\{ P + 3\pi R\gamma_{12} + \left[6\pi RP\gamma_{12} + (3\pi R\gamma_{12})^2 \right]^{\frac{1}{2}} \right\}$$

Equation 5-1

$$\delta = \frac{a^2}{R} \left[1 - \frac{2}{3} \left(\frac{a_{P=0}}{a} \right)^{\frac{3}{2}} \right]$$

Equation 5-2

where γ_{12} is the interfacial energy, $a_{P=0}$ is the contact radius under zero external load, K is a constant related to the elastic constants of the AFM tip and the sample, and R is the normalised radius of the two spheres. K and R are given by **Equation 5-3** and **Equation 5-4**, respectively.

$$K = \frac{4}{3\pi(k_{\text{tip}} + k_{\text{sample}})}$$

Equation 5-3

$$R = \frac{R_{\text{tip}} R_{\text{sample}}}{R_{\text{tip}} + R_{\text{sample}}}$$

Equation 5-4

where k_{tip} and k_{sample} are the elastic constants of the AFM tip and the sample respectively, and R_{tip} and R_{sample} are the tip radius and the sample radius, respectively. k_{tip} and k_{sample} are related to the elastic modulus of the tip and the sample as given by **Equation 5-5** and **Equation 5-6**, respectively.

$$k_{\text{tip}} = \frac{1 - \nu_{\text{tip}}^2}{\pi E_{\text{tip}}}$$

Equation 5-5

$$k_{\text{sample}} = \frac{1 - \nu_{\text{sample}}^2}{\pi E_{\text{sample}}}$$

Equation 5-6

where ν is the Poisson ratio and E_{tip} and E_{sample} is the Young's modulus of the tip and sample, respectively. Because the sample radius is much larger than the tip radius, the normalised radius is equivalent to the tip radius: $R = R_{\text{tip}}$ ($R_{\text{tip}} \ll R_{\text{sample}}$).

The generally used AFM silicon nitride tip has a Young's modulus ~220 GPa while the Young's modulus of the silicon cantilever ~190 GPa (Cuenot *et al.* 2000). The protein nanotube of interest has a Young's modulus only ~20 MPa (Trachtenberg and Hammel 1992 and also see section 4.2.4). Therefore, combining **Equation 5-3**, **Equation 5-5** and **Equation 5-6**:

$$E_{\text{sample}} = \frac{3(1-\nu_{\text{sample}}^2)}{4} K \quad (E_{\text{tip}} \gg E_{\text{sample}})$$

Equation 5-7

For each point on the force-versus-indentation curve, there are three variables: the contact radius a , interfacial energy γ , and Young's modulus of the sample E_{sample} . The external load P and the indentation δ can be read directly from the force-versus-indentation curve. Combining any two points on the force-versus-indentation curve, using **Equation 5-1** and **Equation 5-2**, a , γ and E_{sample} can be obtained (Sun *et al.* 2004). For the ease of data processing, special points on the force-versus-indentation curve are chosen: the point where $P = 0$ (**Figure 5-1 b**, point "0") and the point where $\delta = 0$ (**Figure 5-1 b**, point "2").

At the point $P = 0$, **Equation 5-1** and **Equation 5-2** become:

$$a_{P=0}^3 = \frac{6\pi R^2 \gamma_{12}}{K}$$

Equation 5-8

$$\delta_{P=0} = \frac{a_{P=0}^2}{3R}$$

Equation 5-9

At point $\delta = 0$, **Equation 5-1** and **Equation 5-2** become:

$$a_{\delta=0}^3 = \frac{R}{K} \left\{ P_{\delta=0} + 3\pi R\gamma_{12} + \left[6\pi R P_{\delta=0} \gamma_{12} + (3\pi R\gamma_{12})^2 \right]^{\frac{1}{2}} \right\}$$

Equation 5-10

$$\left(\frac{a_{P=0}}{a_{\delta=0}} \right)^{\frac{3}{2}} = \frac{3}{2}$$

Equation 5-11

Combining **Equation 5-8** and **Equation 5-10**, then **Equation 5-11**:

$$P_{\delta=0} = -\frac{4}{3} \pi R \gamma_{12}$$

Equation 5-12

where the negative sign means the external load is on the direction of retraction from the sample.

Combining **Equation 5-8**, **Equation 5-9** and **Equation 5-12**:

$$K = \frac{-P_{\delta=0}}{2} \left(\frac{3}{R\delta_{P=0}^3} \right)^{\frac{1}{2}}$$

Equation 5-13

Bringing **Equation 5-13** into **Equation 5-7**:

$$E_{\text{sample}} = \frac{3(\nu_{\text{sample}}^2 - 1)P_{\delta=0}}{8} \left(\frac{3}{R\delta_{P=0}^3} \right)^{\frac{1}{2}}$$

Equation 5-14

From **Equation 5-14**, the Young's modulus of the sample can be obtained.

5.1.2 Applying JKR Model to Obtain the Young's Modulus of a Sample

In this section, the details of data processing of a typical force-versus-indentation curve will be explained with an example.

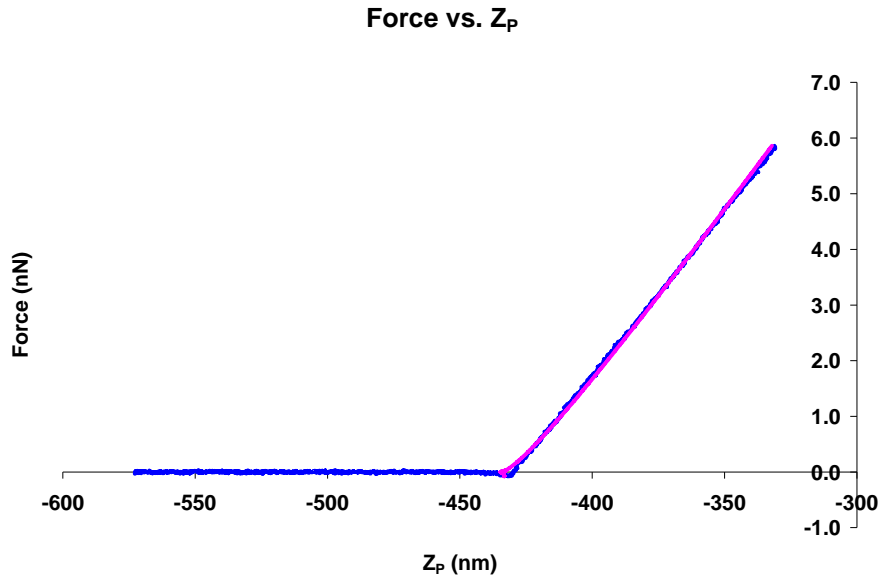
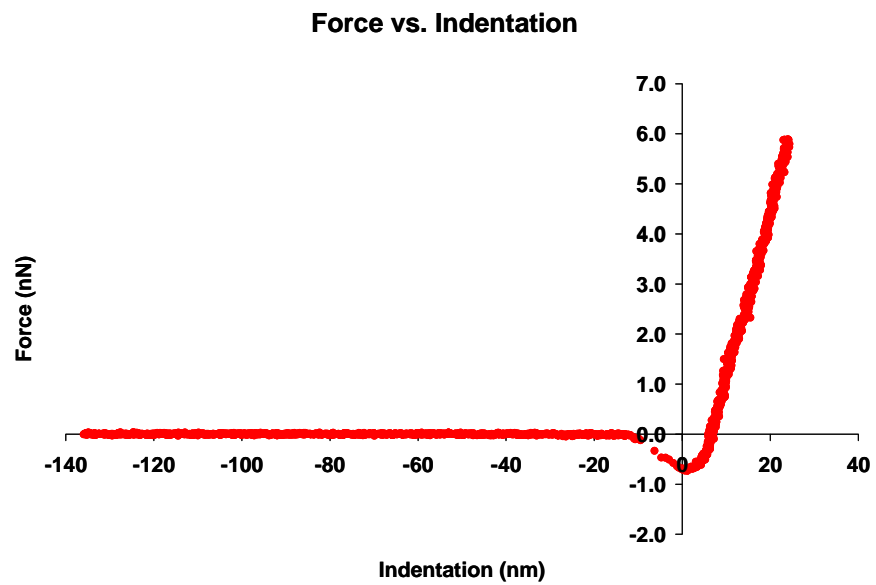


Figure 5-2 A force-versus-displacement approach curve. A silicon nitride tip was used, with the spring constant k_c of 0.07292 N/m determined by thermal method (see section 2.1.1.3). *Salmonella* flagellar filaments were deposited onto mica surface (see section 2.2). The experiment was carried out in PBS buffer with $MgCl_2$ ($I = 0.1$ M, $c_{PBS} = 0.01$ M, $c_{Mg^{2+}} = 0.01$ M, pH 7.0). The blue curve is the experimental data curve. The pink curve is the fitting curve with Hertzian model (see section 2.1.1.3). $Z_{p0} = -434.7 \pm 0.1$ nm were obtained by the fitting.

The force-versus-displacement approach curve of a silicon nitride tip ($k_c = 0.07292$ N/m) on *Salmonella* flagellar filaments in buffer solution is shown on **Figure 5-2**. In order to find the zero piezo displacement point, the experimental data in the range when the tip and sample came into contact were fitted with a Hertzian model (see section 2.1.1.3).

a



b

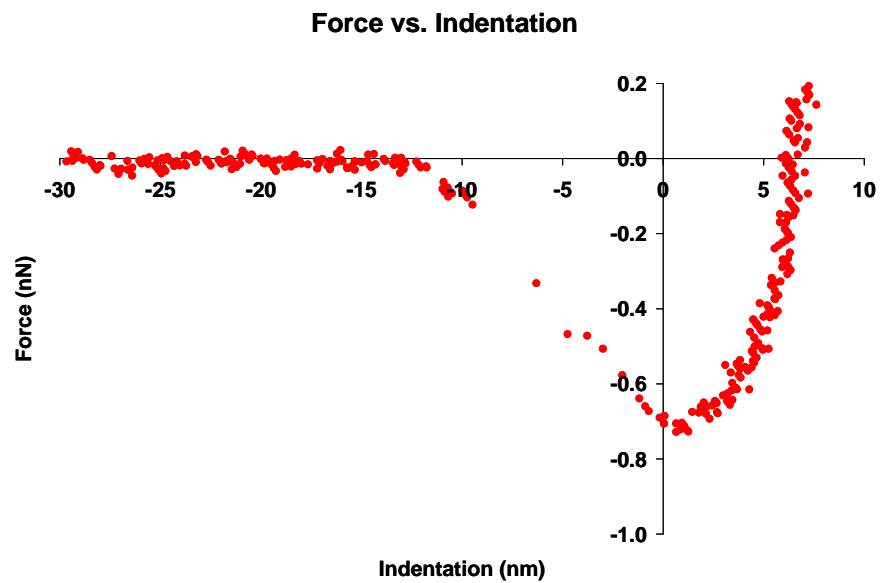


Figure 5-3 The force-versus-indentation retract curve from the same experiment of **Figure 5-2**. (a) is the whole retract curve and (b) is zoomed part of the curve. Reading from (b), there are $P_{\delta=0} = 0.69$ nN and $\delta_{P=0} = 6.7$ nm.

Using the zero piezo displacement obtained from fitting to the approach curve, the force-versus-indentation retract curve could be obtained (**Figure 5-3**). The values $P_{\delta=0} = 0.69$ nN and $\delta_{P=0} = 6.7$ nm were read directly from the force-versus-indentation retracting curve. Tip radius $R = 3.0$ nm was obtained using blind reconstruction method with SPIP software (see section **2.1.3**). Blind reconstruction is a technique of estimating the geometry of AFM tip from the topographic image data (Villarrubia 1997; Williams *et al.* 1996). A thin film of porous aluminum consisting of hexagonal hollow cells (Mikromash, USA) was imaged using the same tip used in the adhesive interaction experiment in order to estimate the geometry of the tip. Bringing all these values to **Equation 5-14** resulted $E = 11.2$ MPa.

A number of force curves under the same conditions were then obtained in order to calculate the average Young's modulus (**Figure 5-4**). The average Young's modulus E of *Salmonella* flagellar filaments under this condition was $E = 7.2 \pm 0.8$ MPa.

A control experiment has also been done under the same condition. A retract force curve obtained on mica surface in buffer solution is displayed in **Figure 5-5**. The mica surface is hard with a high Young's modulus (140 to 200 GPa, manufacturer's data), and it can be treated as a non-deformable surface with attraction force (see section **2.1.1.3**).

E of *Salmonella* flagellar filaments on mica in buffer
($I = 0.1$ M, $c_{Mg} = 0.01$ M, pH 7.0)

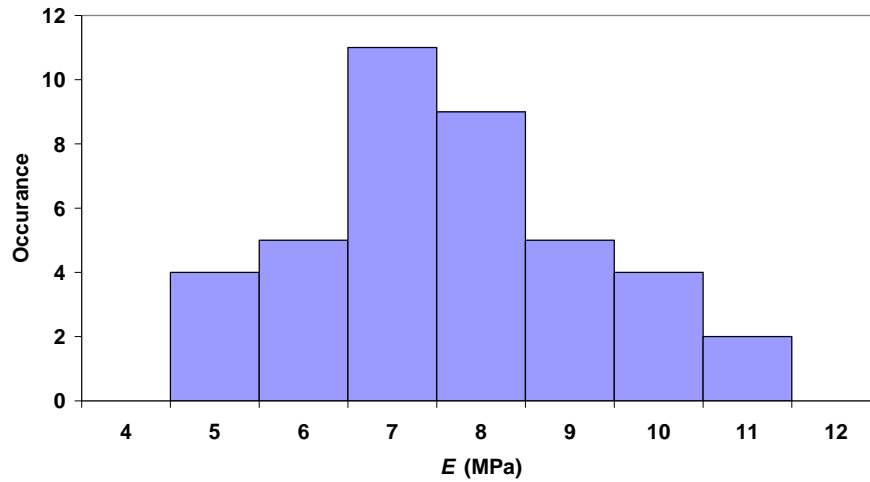


Figure 5-4 Histogram of Young's modulus E of *Salmonella* flagellar filaments on mica in PBS buffer with $MgCl_2$ ($I = 0.1$ M, $c_{PBS} = 0.01$ M, $c_{Mg^{2+}} = 0.01$ M, pH 7.0) obtained using adhesive interaction method. The mean Young's modulus $E = 7.2 \pm 0.8$ MPa ($N = 40$).

Force vs. Indentation

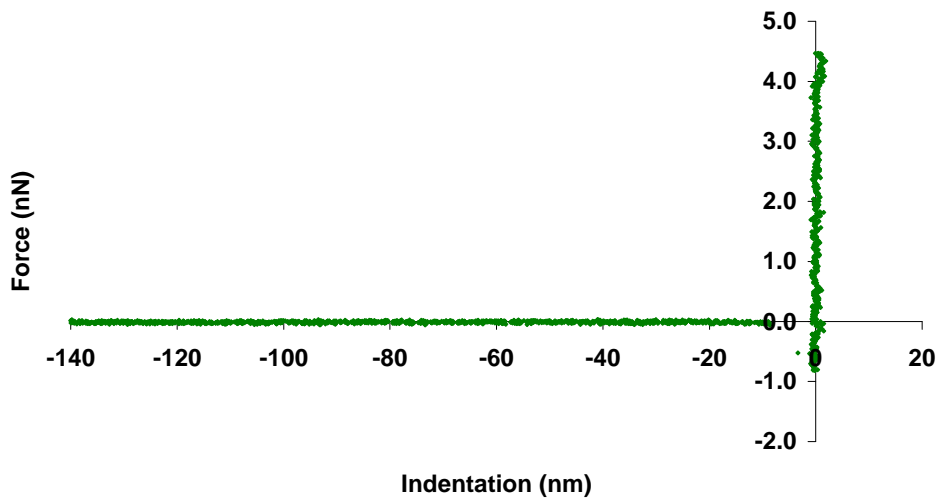


Figure 5-5 The force-versus-indentation retractor curve from the control experiment. The force curve was obtained on mica surface in PBS buffer with $MgCl_2$ ($I = 0.1$ M, $c_{PBS} = 0.01$ M, $c_{Mg^{2+}} = 0.01$ M, pH 7.0). The same tip was used as in the experiment of **Figure 5-2** and **Figure 5-3**.

5.2 The Effects of the Ionic Strength on the Elasticity of *Salmonella* Flagellar Filaments

In a similar manner as explained in the previous section, force curves of *Salmonella* flagellar filaments on mica in different buffer solutions were obtained and the Young's modulus calculated using the JKR model (Johnson, Kendall and Roberts 1971).

Keeping the ionic strength I constant ($I = 0.5$ M, $c_{\text{PBS}} = 0.01$ M, pH 7.0), while changing the concentration of Mg^{2+} , the Young's modulus E of *Salmonella* flagellar filaments was obtained (Table 5-1).

Table 5-1 Young's modulus E of *Salmonella* flagellar filaments in buffer solutions with different concentrations of Mg^{2+} .

Ionic strength I (M)	Concentration of Mg^{2+} $c_{\text{Mg}^{2+}}$ (M)	Young's modulus E (MPa)
0.5	0.01	13.0 ± 1.8
0.5	0.05	12.0 ± 2.6
0.5	0.1	13.5 ± 2.2

Salmonella flagellar filaments were deposited on mica surfaces in buffer solutions ($c_{\text{PBS}} = 0.01$ M, pH 7.0, pH adjusted using HCl or NaOH, I adjusted using NaCl). The Young's modulus E was obtained using adhesive interaction method explained in previous section.

There was no statistically significant difference among the three Young's modulus groups with $c_{\text{Mg}^{2+}}$ of 0.01M, 0.05M and 0.1M. Therefore there was no obvious relation between E and $c_{\text{Mg}^{2+}}$ (Table 5-1). However, when the concentration of Mg^{2+} was kept constant, the Young's modulus of *Salmonella*

flagellar filaments increased with the increasing of ionic strength of the solutions (Table 5-2).

Table 5-2 Young's modulus E of *Salmonella* flagellar filaments in buffer solutions with different ionic strength.

Ionic strength I (M)	Concentration of Mg^{2+} $c_{Mg^{2+}}$ (M)	Young's modulus E (MPa)
0.1	0.01	7.2 ± 0.8
0.5	0.01	13.0 ± 1.8
1.0	0.01	18.6 ± 4.5

Salmonella flagellar filaments were deposited on mica surface in buffer solutions ($c_{PBS} = 0.01$ M, pH 7.0, pH adjusted using HCl or NaOH, I adjusted using NaCl). The Young's modulus E was obtained using adhesive interaction method explained in previous section.

Table 5-3 Summary of Young's modulus E of *Salmonella* flagellar filaments in different buffer solutions.

Ionic strength I (M)	Concentration of Mg^{2+} $c_{Mg^{2+}}$ (M)	Young's modulus E (MPa)
0.1	0.01	7.2 ± 0.8
0.5	0.01	13.0 ± 1.8
0.5	0.05	12.0 ± 2.6
0.5	0.1	13.5 ± 2.2
1.0	0.01	18.6 ± 4.5
1.0	0.2	20.5 ± 5.3

Salmonella flagellar filaments were deposited on mica surface in buffer solutions ($c_{PBS} = 0.01$ M, pH 7.0, pH adjusted using HCl or NaOH, I adjusted using NaCl). The Young's modulus E was obtained using adhesive interaction method explained in previous section.

All the experimental results of Young's modulus E of *Salmonella* flagellar filaments obtained using adhesive interaction method were summed up and displayed in **Table 5-3**. Young's modulus E was plotted against the ionic strength I of the buffer solutions (**Figure 5-6**).

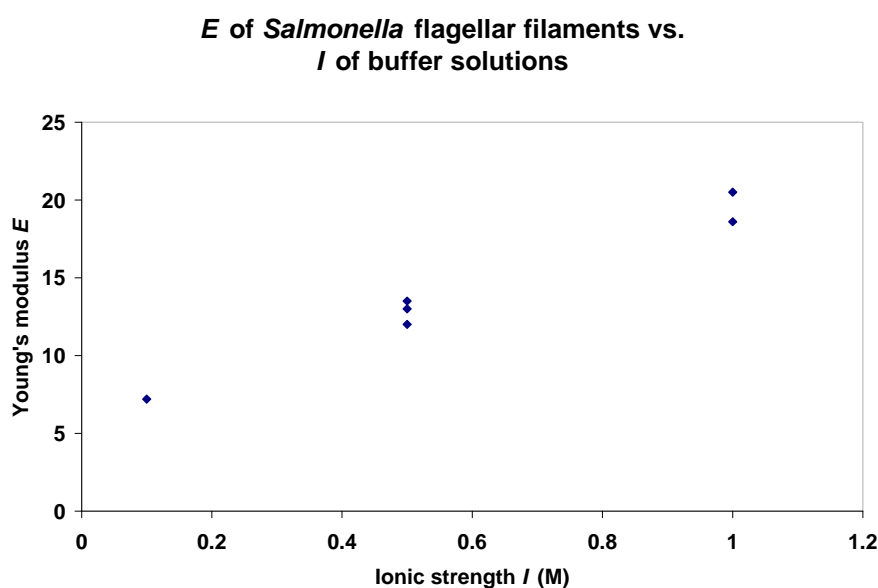


Figure 5-6 Young's modulus E of *Salmonella* flagellar filaments versus the ionic strength I of buffer solutions. *Salmonella* flagellar filaments were on mica surface in buffer solutions ($c_{\text{PBS}} = 0.01$ M, pH 7.0, pH was adjusted using HCl or NaOH, I was adjusted using NaCl). Data is from **Table 5-3**. The error bars are not shown for clarity.

As explained in section 3.1, Mg^{2+} acts as a bridge between *Salmonella* flagellar filaments and the mica surface in pH 7.0 buffer solution to immobilise the filaments onto the substrate. Using the adhesive interaction method, the concentration of Mg^{2+} (from 0.01M to 0.2M) in buffer solutions was found not to have an effect on the elasticity of *Salmonella* flagellar filaments. However, when the ionic strength of the buffer solutions (regulated by NaCl) increased, the

Young's modulus of *Salmonella* flagellar filaments increased. In other words, the higher the ionic strength of the buffer is, the harder *Salmonella* flagellar filaments appeared to become (Adami *et al.* 1999; Srigriraju *et al.* 2005). This discovery showed the potential of flagellar filaments as smart materials. The alteration of elasticity of flagellar filaments can be easily controlled by modifying the ionic strength of the fluidic environment they are in.

One systematic error of the resulting Young's modulus from this adhesive interaction method is caused by the determination of the tip radius R . As explained in section 5.1.2, the tip radius R was obtained by using the blind reconstruction method provided by SPIP software (Villarrubia 1997; Williams *et al.* 1996). However, only the radius of the "worst case tip" can be obtained by this method. This "worst case tip" is the tip that is able to scan all parts of the surface with its apex, but the tip might be sharper in reality. This brought a possible error on the Young's modulus obtained using Equation 5-14. If the tip in reality is 10% sharper, the value of the Young's modulus would be 5% greater than calculated.

In order to apply the adhesive interaction method to *Salmonella* flagellar filaments in buffer solutions without Mg^{2+} , the force-versus-indentation curves in these solutions were obtained. However, the force-versus-indentation curves in buffer solutions without Mg^{2+} did not show an adhesive part, instead, they had plateaux.

5.3 Investigating the Interaction between *Salmonella* Flagellar Filaments and Mica Substrates in Electrolyte Environments

As presented in section 3.1, the AFM tapping mode images of *Salmonella* flagellar filaments on mica in pH 7.0 buffer solution containing Mg^{2+} were obtained. If Mg^{2+} was not present, the *Salmonella* flagellar filaments could not be immobilised onto the mica surface and allow scanning of AFM tip. However, the force curves of *Salmonella* flagellar filaments could be obtained within this environment. Unlike the force curves of *Salmonella* flagellar filaments on mica in pH 7.0 solution with Mg^{2+} , there were visible plateaux in those force curves. The force-versus-indentation curves collected had either one or two plateaux (e.g. the force curve in **Figure 5-7** has two plateaux). Force curve consisting more than two plateaux was not found during my experiments. A typical force-versus-indentation curve of *Salmonella* flagellar filaments on mica in pH 7.0 buffer without Mg^{2+} is shown in **Figure 5-7**.

There are two visible plateaux in the force-versus-indentation curve in **Figure 5-7**. The heights of the plateaux most likely reflect the constant equilibrium desorption forces resulting from the process of peeling off one or more individual filaments from the surface with the AFM tip (Friedsam *et al.* 2004). In this particular sample (**Figure 5-7**), the heights of the two plateaux are $F_1 = 0.11$ nN and $F_2 = 0.21$ nN. These two values are the average of the heights of all the experimental points of each plateau respectively. The more negative end (the end on the direction of retracting the tip from the surface) of each plateau could represent the rupture of the filament from the mica surface or from the AFM tip. The lengths of plateaux, which will be referred as desorption lengths in this

section, correspond to partial or full lengths of the desorbed filaments. In this particular sample (**Figure 5-7**), the lengths are $l_1 = 151$ nm, $l_2 = 183$ nm.

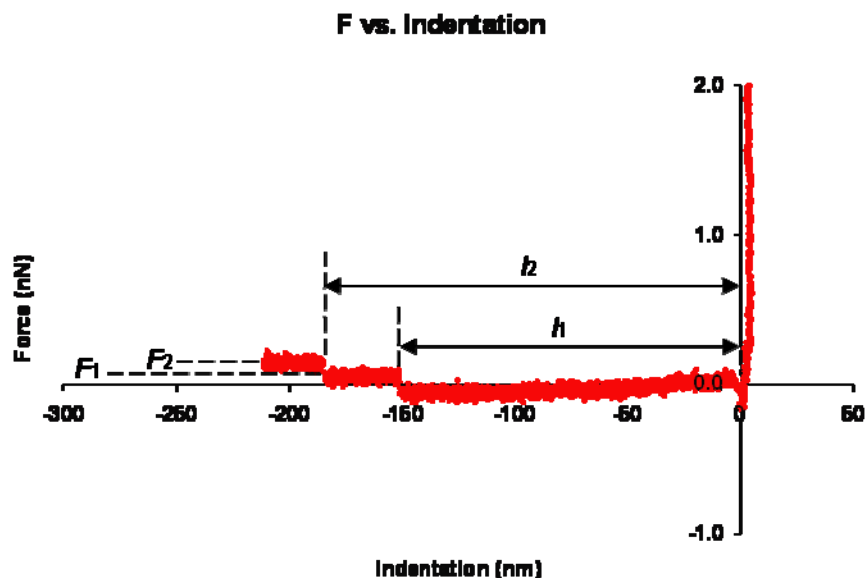


Figure 5-7 A force-versus-indentation retracting curve of *Salmonella* flagellar filaments on mica surface in pH 7.0 buffer ($c_{\text{PBS}} = 0.01$ M) without Mg^{2+} . A silicon nitride tip was used. There are two visible plateaux with heights $F_1 = 0.11$ nN and $F_2 = 0.21$ nN and length $l_1 = 151$ nm and $l_2 = 183$ nm.

In order to do batch analysis of the plateaux, I developed a programme “Stepfinder” written in Visual Basic for Application (VBA) language for Microsoft Excel. The stepfinder programme reads the X-Y coordinates of force-versus-indentation curves and calculates the central difference of the function $P = f(\delta)$ (where P is the force and δ is the indentation) (Abramowitz and Stegun 1972). The central difference is then plotted against the indentation δ . The peaks on the central difference curve correspond to the starting and ending points of the plateaux on the force-versus-indentation curve. Using the points between the

starting and ending points of the plateaux, the average of the forces and the lengths of the plateaux can be obtained. All the experimental points between the starting and ending points of a plateau were used to calculate the average desorption force and the desorption length. This programme considerably accelerated the speed of the data process. The following histogram of the desorption forces was obtained (Figure 5-8).

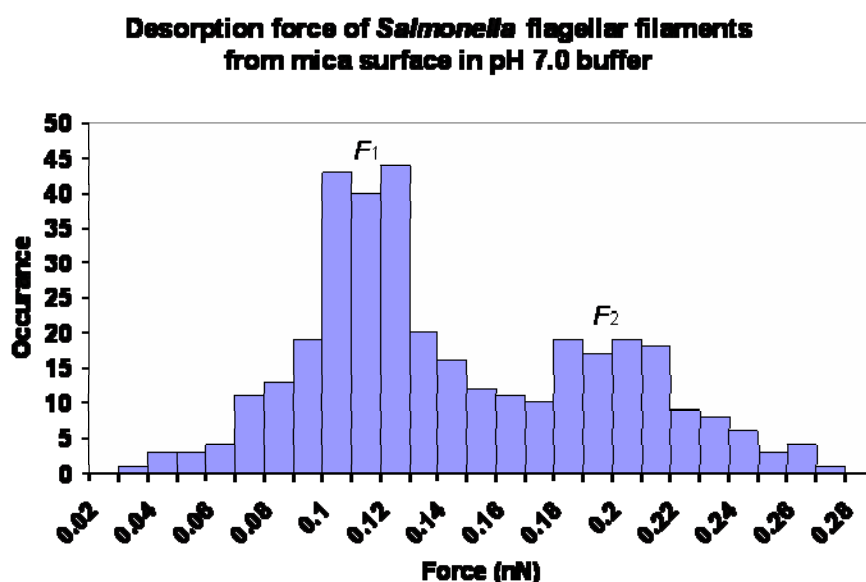


Figure 5-8 Histogram of desorption forces of *Salmonella* flagellar filaments from mica surface in pH 7.0 buffer without Mg^{2+} . Two peaks on this histogram are $F_1 = 0.11 \pm 0.1$ nN and $F_2 = 0.20 \pm 0.1$ nN (N = 344).

As shown in **Figure 5-8**, there are two peaks on the histogram of desorption forces (F_1 and F_2). By fitting Gaussian distributions to the two peaks separately, $F_1 = 0.11 \pm 0.1$ nN and $F_2 = 0.20 \pm 0.1$ nN were obtained. The peaks on the histogram of desorption force reflect the force required to peel off one or more flagellar filaments from the mica surface (Friedsam *et al.* 2004). The F_1 and F_2 on

the histogram correspond to the F_1 and F_2 plateaux on the force-versus-indentation curve (**Figure 5-7**). Considering F_2 is approximately two times of F_1 , if F_1 is the force required to peel off a single flagellar filament from the mica surface, F_2 could be the force required to peel off two flagellar filaments from the mica surface at the same time.

The desorption length of *Salmonella* flagellar filaments on mica surface in pH 7.0 buffer without Mg^{2+} was found to be from 4 nm to 197 nm. This value range is lower than the value range of the length of *Salmonella* flagellar filaments obtained by AFM imaging 1.0 to 3.0 μm (see section 3.1). One way to explain this difference could be that the desorption length of the filament is only part of a whole filament. In other words, the picking up and peeling off process by AFM tip were only applied to part of the filament. The reason why this happened is most likely that the AFM tip picked up a filament from the middle of the filament instead of from the end, or the rupture of the filament from the AFM tip could happen before the full length of filament had peeled off the surface.

This experiment showed that the adhesive interaction method requires the filaments to be immobilised onto the substrate surface. In pH 7.0 buffer, with Mg^{2+} , *Salmonella* flagellar filaments could be immobilised onto mica surface and the adhesive interaction method could be applied to obtain the elasticity (see previous section 5.2). However, without Mg^{2+} , in pH 7.0 buffer, *Salmonella* flagellar filaments would be picked up and peeled off the mica surface by AFM tip. This peeling off experiment could be utilised to access the desorption forces between the protein nanotubes and different substrate surfaces, which could provide the information of manipulating protein nanotubes individually.

5.4 Conclusion

If a protein nanotube is properly immobilised onto a substrate surface, when an AFM tip retracts from the surface of the soft protein nanotube, the tip can pull up and deform the sample because of the adhesive force. This deformation of the protein nanotube is related to its elasticity. In this chapter, the JKR (Johnson, Kendall and Roberts 1971) model has been applied to obtain the elastic information of *Salmonella* flagellar filaments, and the effect of the ionic strength on the elasticity of *Salmonella* flagellar filaments investigated.

The Young's modulus of *Salmonella* flagellar filaments was found to be from 7.2 MPa to 21.5 MPa. The concentration of Mg^{2+} (from 0.01 M to 0.2 M) in buffer solutions was found not to have effect on the elasticity of *Salmonella* flagellar filaments. However, when the ionic strength of the buffer solutions increased, the Young's modulus of *Salmonella* flagellar filaments increased.

The adhesive interaction method requires the protein nanotubes to be immobilised onto the substrate surface. Without Mg^{2+} , in pH 7.0 buffer, *Salmonella* flagellar filaments could be picked up and peeled off the mica surface by AFM tip with a desorption force of 0.11 nN.

Chapter 6 Using the Bending Beam Model

to Estimate the Elasticity of Protein

Nanotubes

If a protein nanotube can be placed over a cavity of the substrate, a suspended beam configuration is produced at the nanoscale. The beam will have different degrees of bending with different loading forces acting on it, related to its elastic properties. By using an AFM probe to apply loading forces on a protein nanotube, its elastic properties can therefore be obtained. In this chapter, the bending beam model is explained and then applied to protein nanotubes for this type of analysis.

6.1 Theory

6.1.1 Deformation of a Fixed-End Bending Beam

As explained in Gere's book "Mechanics of Materials" (1991) for the case of a concentrated load acting at the midpoint of a suspended fixed-end beam, using a unit-load method, the deflections at the midpoint of the beam when considering the effects of both bending moments and shear forces is as follows:

$$\begin{aligned}\delta &= \delta_B + \delta_S \\ &= FL^3 / 192EI + f_s FL / 4GA\end{aligned}$$

Equation 6-1

where δ is the deflection, δ_B is the deflection due to bending, δ_S is the deflection due to shearing; E is the Young's modulus, G is the shear modulus; F is the loading force; L is the suspended length; f_s is a cross-sectional property called the form factor for shear, which is a dimensionless quantity that can be evaluated for each particular shape of beam ($f_s = 10/9$ for a cylindrical beam); A is the cross-sectional area of the fibril; I is the moment of inertia of area A ($I = \pi D^4/64$ for a filled circular area with diameter D , $I = \pi(D_o^4 - D_i^4)/64$ for a tubular circular area with outer diameter D_o and inner diameter D_i).

We define E_{bending} as the bending modulus that corresponds to the Young modulus that would be deduced if shear deformations were neglected:

$$\begin{aligned}\delta &= \delta_B + \delta_S \\ &= FL^3 / 192EI + f_s FL / 4GA \\ &= FL^3 / 192E_{\text{bending}} I\end{aligned}$$

Equation 6-2

From **Equation 6-2**, there is:

$$1 / E_{\text{bending}} = 1 / E + (48f_s I / GA)(1 / L^2)$$

Equation 6-3

For a beam with several different suspended lengths, the Young's modulus can be obtained from the intercept of the plot of $1/E_{\text{bending}}$ versus $1/L^2$ and the shear modulus can be obtained from the gradient.

6.1.2 Applying the Bending Beam Model to Nanotubes

If a protein nanotube can be placed over a cavity of the substrate, a suspended beam configuration at the nanoscale is produced (**Figure 6-1**). Assuming the two ends are clamped, the elastic deformation in the middle of the suspended part of

the fibril resulting from a concentrated load can be expressed as **Equation 6-1** (Salvetat *et al.* 1999; Kis *et al.* 2002; Niu *et al.* 2007).

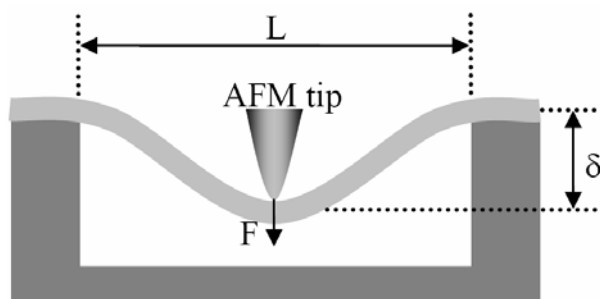


Figure 6-1 Schematic of the suspended beam configuration produced by a protein nanotube lying over a cavity on the substrate. The AFM is used to apply a loading force to the protein nanotube and to determine directly the resulting deflection (figure adapted from Niu *et al.* 2007).

The deflection δ , the suspended length L and the second moment I can be obtained from the profiles of the AFM images of the protein nanotubes. F is the AFM loading force on the nanotube, which is considered as a concentrated force midway along the suspended length of the nanotube. In contact mode AFM images, the loading force is equal to the product of the cantilever deflection, the deflection sensitivity and the spring constant of the AFM probe (see section 2.1.1.3 for the details of calculating force). From **Equation 6-2**, E_{bending} can be calculated. Because E_{bending} depends on the dimension of the protein nanotube from which it is calculated (**Equation 6-2**), in order to compare the elasticity under different experimental conditions by the means of comparing E_{bending} , the same nanotube was used.

In order to obtain Young's modulus E and shear modulus G from **Equation 6-3**, a protein nanotube lying across several holes of the substrate with different suspended length L was found. Assuming the geometry of the cross section remains the same along the protein nanotube, the Young's modulus can be obtained from the intercept of the plot of $1/E_{\text{bending}}$ versus $1/L^2$, and the shear modulus from the gradient.

6.2 β 2-microglobulin Fibrils Lying over Gaps within the Gold

Substrate

An attempt to apply the bending beam model to β 2-microglobulin fibrils was made. The β 2-microglobulin protein solution was incubated at 37°C for 5 days (see section 2.2.3 for the details of sample preparation). The resulting fibrils (**Figure 6-2**) were found to have an average height of 5.8 ± 0.8 nm and lengths from ~ 200 nm up to ~ 4 μ m ($N = 100$). Some fibrils with clear periodicity were observed (**Figure 6-2**) (detailed morphology studies of β 2-microglobulin fibrils by AFM can be found in Kad *et al.* 2003 and Gosal *et al.* 2005).

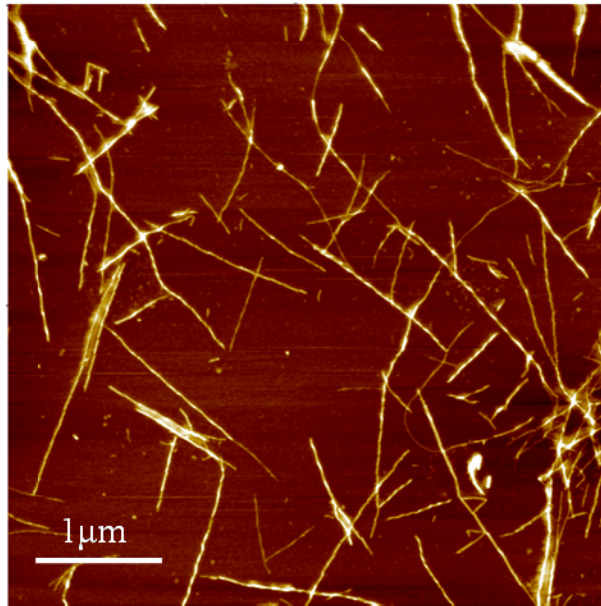


Figure 6-2 AFM height image of β 2-microglobulin fibrils after 5 days of incubation. The Z-range is 21.6 nm.

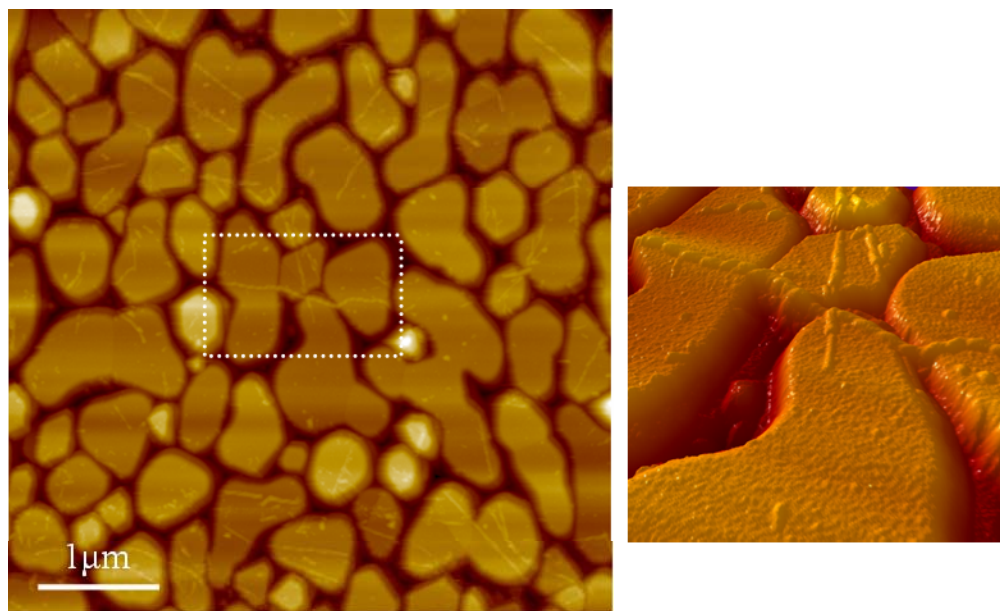


Figure 6-3 AFM image of β 2-microglobulin fibrils obtained in water on gold surfaces. The image on the left is a tapping mode height image. The picture on the right is a 3D representation (generated by SPIP software; see section 2.1.3) of the fibril in the centre of the left image indicated by the white dot-line rectangle.

The gold substrate obtained using evaporation gold coater (see section 2.2.5) has atomically flat islands (typically 0.2 μm to 1.0 μm in width), separated by gaps ~ 30 nm to ~ 150 nm in width. If a $\beta 2$ -microglobulin fibril can be placed over a gap of gold substrate, a suspended beam configuration is produced. However, in order to obtain the value of the loading force (see section 6.1), AFM contact mode images of $\beta 2$ -microglobulin fibrils needed to be obtained. Contact mode AFM imaging applies higher lateral forces on a sample than tapping mode (see section 2.1.1.2). A $\beta 2$ -microglobulin fibril lying over a gap on a gold surface (**Figure 6-3**) was imaged in tapping mode. When switched to contact mode (in order to calculate the forces applied, for the bending beam model), the fibril broke over the gap. No contact mode images of $\beta 2$ -microglobulin fibrils lying over gaps were obtained throughout these studies.

An attempt to apply the bending beam model to *Salmonella* flagellar filaments was also made and the similar situation as for $\beta 2$ -microglobulin fibrils was found: both *Salmonella* filaments and lysozyme fibrils did not survive the imaging process i.e. they broke over the gaps of gold substrate, most likely due to the force applied by the AFM tip during contact mode imaging.

6.3 Elasticity of diphenylalanine Fibrils

The bending beam model was successfully applied to AFM images of diphenylalanine nanotubes (FF nanotubes) suspended across cavities. A micropatterned silicon substrate (with holes of 5 $\mu\text{m} \times 5 \mu\text{m}$ and 200 nm deep) (see section 2.2.5) was used to provide cavities for the suspended beam configuration (Gere 1991).

To prepare samples an aliquot of 10 μL of fresh FF nanotubes sample solution (see section 2.2 for the details of sample preparation) was dropped onto a UV cleaned micropatterned silicon substrate and subsequently dried under a gentle flow of nitrogen. This protocol produced fibrils which were found to occasionally lie over the holes of the substrate.

6.3.1 Elasticity of FF Nanotubes at Room Temperature

What is a “good” deflection?

From Equation 6-2, with the same loading force F and the suspended length L , the deflection δ increases with the decrease of the diameter D of the cross section of the fibril. The range of the loading force in AFM experiments can vary from nN to μN in an ambient atmosphere (Seo and Jhe 2008). The micropatterned silicon substrate employed had square shaped holes of $5\ \mu\text{m} \times 5\ \mu\text{m}$, which meant that the suspended length was up to $7\ \mu\text{m}$ (the length of the diagonals of the holes). The deflection was up to the depth of the holes of the substrate, which was 200 nm. In practice, FF nanotubes with the cross section of around 150-200 nm in diameter were found to provide good bending beam configurations.

Examples of FF nanotubes lying over holes of the silicon grid with different deflections are displayed in Figure 6-4 (details of AFM analysis see section 2.1.2). The deflection of the fibril is the vertical difference between the middle of the suspended part and the part of the nanotube lying on the silicon substrate before or after the hole. The two points taken to measure the deflection theoretically also need to be on the centre of the cross section of the fibril (Figure 6-4 (i)) (Gere 1991).

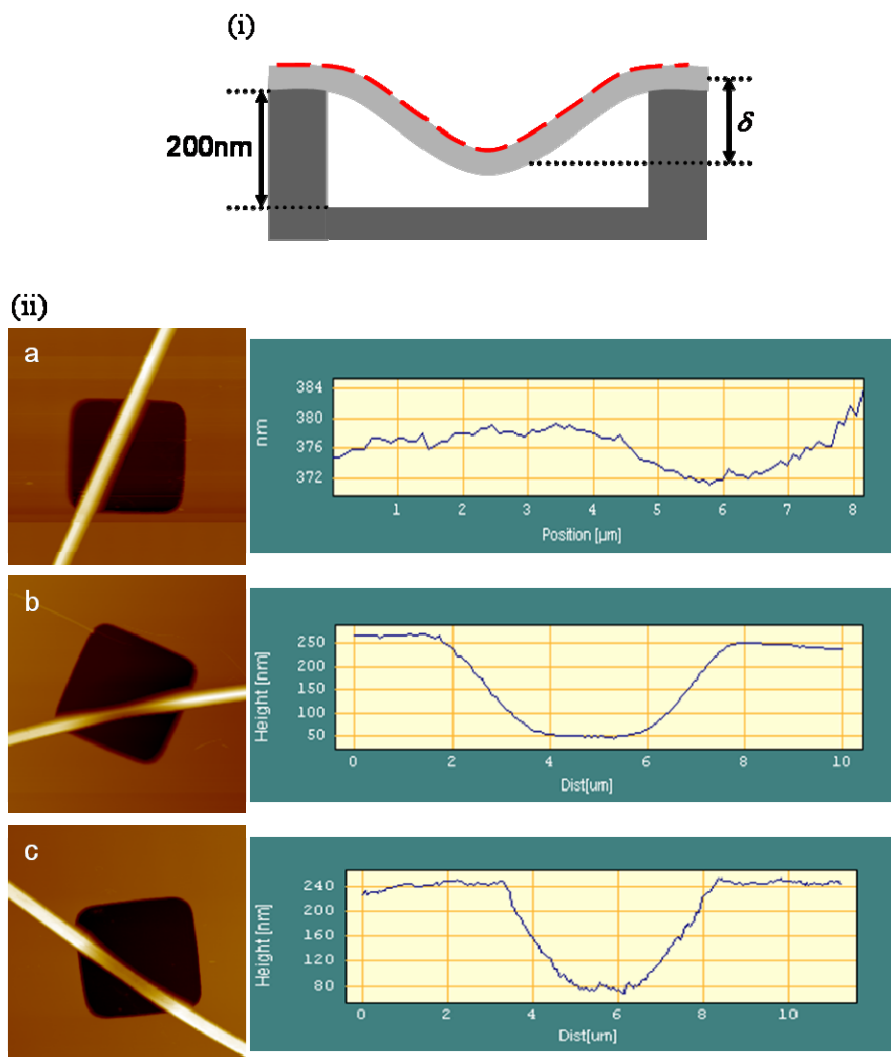


Figure 6-4 Examples of FF nanotubes lying over holes of the silicon substrate with different deflections. (i) A schematic showing a fibril lying over a hole. The depth of the hole is 200 nm. The red broken line indicates where the profiles in (ii) are. (ii) (a) A FF nanotube over a hole with negligible deflection. The profile on the right shows that the vertical difference along the fibril was ~ 10 nm. (b) A FF nanotube touching the bottom of the hole of the substrate. The profile on the right shows the deflection was ~ 200 nm. However, $\sim 2 \mu\text{m}$ (from $\sim 4 \mu\text{m}$ to $\sim 6 \mu\text{m}$ on the x axis) of the fibril seems horizontal, which indicates that it is most likely touching the bottom of the hole. (c) A FF nanotube over a hole with a "good" deflection. The profile on the right shows the deflection was 160 nm. The size of each image in (ii) is $10 \mu\text{m} \times 10 \mu\text{m}$. The Z-range of each image in (ii) is $1.035 \mu\text{m}$, $1.137 \mu\text{m}$ and 966.5 nm , respectively.

However, the profiles obtained from AFM height images only show the heights of the upper surface of the sample. Therefore, assuming the geometry of the cross section remains the same along the fibril, the surface profiles on the top along the fibril (**Figure 6-4 (i)**, indicated by red dot-line) also represent the profiles along the centre of the fibril. A FF nanotube over a hole with negligible deflection, a FF nanotube touching the bottom of the hole of the substrate and a FF nanotube over a hole with a “good” deflection are shown in **Figure 6-4 (ii)**.

Is the deflection reversible?

In order to verify that the deflection of the suspended parts of the fibrils was reversible, the following experiment was performed. For example, a fibril of 155 nm in diameter lying over a hole with suspended length 3.88 μm was imaged. The loading force was increased and then decreased back to approximately the original value. The parameters and results are shown in **Table 6-1**. It can be seen that for this filament the deflection was reversible and increased with increasing loading force.

Table 6-1 The reversible indentation of a FF nanotube over a hole under the loading force of AFM tip.

Loading force F (nN)	Indentation δ (nm)	E_{bending} (GPa)
21.5	155	1.53
22.6	164	1.52
24.7	177	1.54
26.8	190	1.55
21.9	162	1.49

A fibril of 155 nm in diameter lying over a hole with suspended length 3.88 μm was imaged. The loading force was increased from 21.5 nN to 26.8 nN and then decreased back to 21.9 nN. The indentation was increased with the loading force from 155 nm to 190 nm and then be no more than 200 nm (which is the depth of the holes of the silicon substrate). If the loading force exceeded this limit, the fibril would probably be touching and sticking to the bottom of the hole and therefore the indentation might not be reversible any more. In this particular sample above (**Table 6-1**), the loading force could not exceed 27.7 nN.

As stated in section 6.1, from the profile of a fibril over a hole with “good” deflection, the E_{bending} could be calculated. In order to calculate E and G , a fibril lying across several holes with at least three different suspended lengths was however needed (Salvetat *et al.* 1999; Kis *et al.* 2002), which was particularly difficult to obtain.

Obtaining E and G

An example of a fibril lying across five holes of the silicon grid is displayed in **Figure 6-5**. As can be observed, the fibril has different suspended lengths over each hole. For this fibril, its length also exceeds the maximum scan size.

Using the height determined from the profile of the cross section as the diameter D , E_{bending} was obtained from **Equation 6-2**. The graph of $1/E_{\text{bending}}$ against $1/L^2$ for this fibril is displayed in **Figure 6-6**. From **Equation 6-3**, assuming the geometry of the cross section was constant, the Young’s modulus E was determined as 27 ± 4 GPa and the shear modulus G as 0.21 ± 0.03 GPa (Niu *et al.* 2007).

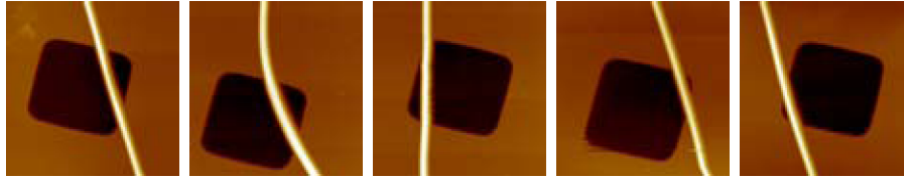


Figure 6-5 AFM images of a single FF nanotube on a silicon grid. One fibril lying across five holes of silicon grid, consequently with different suspended lengths L . The diameter of the fibril was 236 nm and the loading force was 86.7 nN. The size of each image is $10\ \mu\text{m} \times 10\ \mu\text{m}$ and the Z-range is 704 nm (figure adapted from Niu *et al.* 2007).

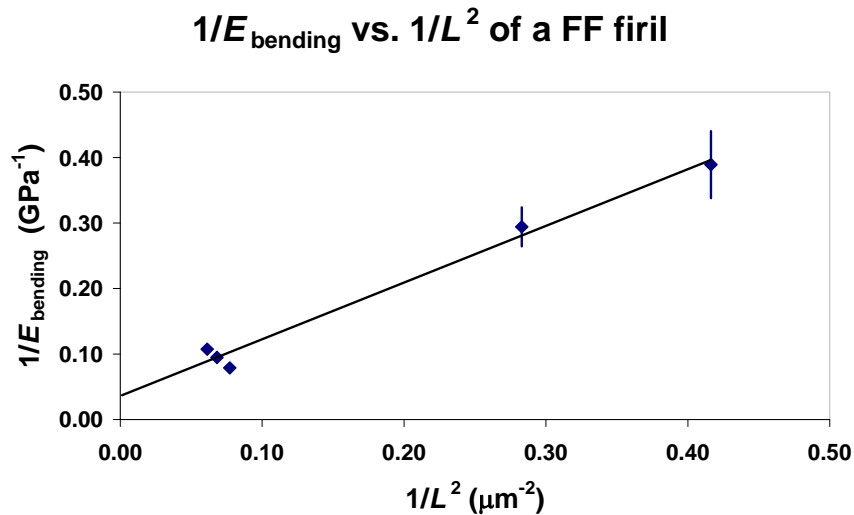


Figure 6-6 The graph of $1/E_{\text{bending}}$ against $1/L^2$ of the fibril in **Figure 6-5**. The error bars of the three left points are within the marker size.

From direct force measurement (indentation experiments) in a previous AFM study, the Young's modulus of FF nanotubes was determined to be 19 GPa (Kol *et al.* 2005). The result obtained using bending beam model therefore agreed with the result from direct force measurement. The difficulty of using direct force measurements however, is the need to align the AFM tip on the middle of a single

fibril. The bending beam model avoids this serious difficulty and also allows the shear modulus to be obtained.

The result showed that G is only ~1-3% of E . For ordinary materials which are homogeneous and linearly elastic, G is typically 0.3 to 0.5 times of E (Gere 1991). The low G/E ratio therefore suggests that FF nanotubes are anisotropic materials and the FF peptides are more strongly bound in the longitudinal direction than the axial direction. In FF nanotubes, there are hydrogen bonds and aromatic stacking interactions between the individual FF peptides. It is highly possible that hydrogen bonds contribute more in the longitudinal direction while aromatic stacking interactions contribute more in the axial direction (Görbitz 2006).

Determination of D effects the resulting E and G

For the bending beam model, the boundary conditions are critical. The fibrils studied were usually several times longer than the size of the holes of the silicon grid; the position of the fibrils remained the same through AFM operation, so we could assume a fibril suspended on a hole was clamped at the two ends. The main source of experimental error therefore comes from the determination of diameter D , because the bending modulus E_{bending} is related to the fourth power of D (see section 6.1.1). If the cross section of the fibril is a filled circular area, using the height determined from the profile of the cross section as the diameter D , the Young's modulus E is 27 ± 4 GPa and the shear modulus G is 0.21 ± 0.03 GPa. Using the width at the half height as diameter D (see section 2.1.3), E is 3.6 ± 0.6 GPa and G is 0.08 ± 0.01 GPa. However, the FF nanotubes are actually hollow tubes (Reches and Gazit 2003; Song *et al.* 2004; also see section 1.3.3), but the inner diameter could not be obtained from AFM imaging. If the cross section of

the fibril is a hollow circular area, assuming the inner diameter D_i is 70% of the outer diameter D_o (Song *et al.* 2004), using the width at the half height as outer diameter D_o , the resulting E is 4.7 ± 0.7 GPa and G is 0.15 ± 0.02 GPa, which does not change the order of magnitude.

If as stated in Kol's paper (2005), the diameter of the cross section (from ~150 nm to ~300 nm) does not have effect on the Young's modulus of FF nanotubes, the Young's modulus obtained from any single one of FF nanotubes using this bending beam method represents the Young's modulus of all the FF nanotubes. However, as described in section 4.4, this conclusion could not be drawn before all diameters (from under 150 nm to more than 300 nm) have been investigated. The bending beam method has the potential to be used to investigate the relationship between the diameter of the cross section and the Young's modulus, provided substrates with different sizes and/or depths of cavities are to be used.

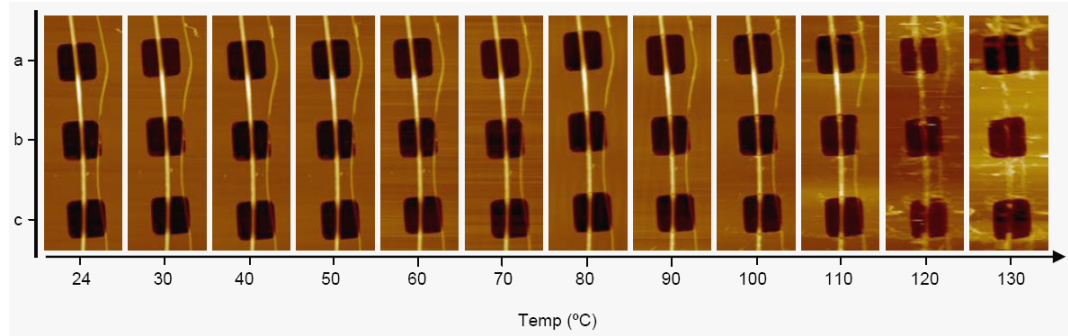
6.3.2 Effect of Temperature on the Elasticity of FF

For temperature studies, samples were placed onto the stage of EnviroScope AFM (Digital Instruments) and initially imaged at room temperature. The temperature was then increased from 30 °C to 130 °C with increments of 10 °C. Following each temperature increase the system was allowed to equilibrate for 5 minutes before imaging commenced (see section 2.1.2 for the details).

A sequence of images of the same two fibrils from room temperature (24 °C) to 130 °C is displayed (Figure 6-7 (i)). There was no visible change on the morphology of the fibrils at temperatures up to 100 °C. Higher temperatures caused the fibrils to begin to lose their structural integrity (Sedman *et al.* 2006; Kol *et al.* 2005). The three lines on Figure 6-7 (ii) show the value of E_{bending} for the

three holes (a, b, c) correspondingly of the left fibril on **Figure 6-7 (i)** at temperatures from 24 °C to 100 °C. The value of E_{bending} gradually decreased ~30% over this temperature range.

(i)



(ii)

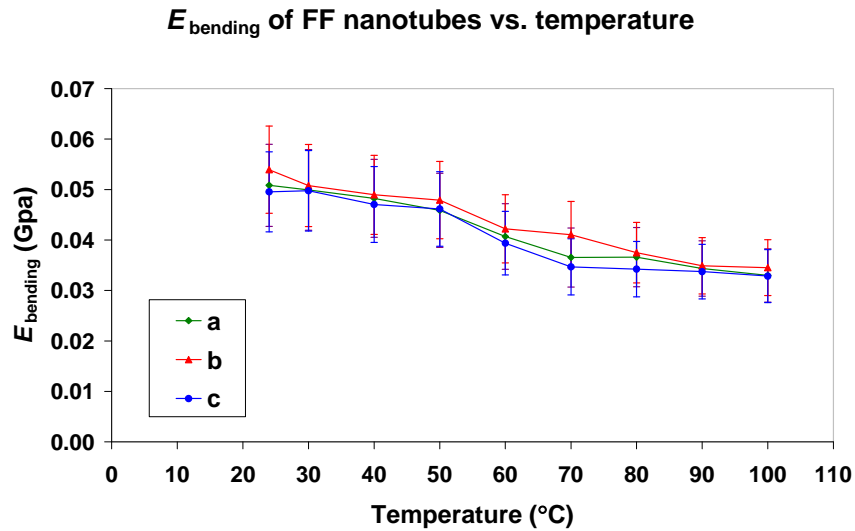


Figure 6-7 AFM images of FF nanotubes at different temperatures. (i) A sequence of images of the same two fibrils at the temperature from 24 to 130 °C. The size of each image is 30 μm (height) \times 10 μm (width). The Z-range of all the images in (i) is $1.18 \pm 0.08 \mu\text{m}$. Three lines on (ii) show the E_{bending} at three holes (a, b, c) corresponding to the left fibril on (i) at temperature from 24 to 100 °C (Niu *et al.* 2007).

A previous high-resolution scanning electron microscope (HRSEM) study showed that the FF nanotubes kept the same morphology at temperatures up to 150 °C (Adler-Abramovich *et al.* 2006). In previous AFM study however, Sedman and co-workers (2006) showed that during *in situ* heating experiments FF nanotubes kept their wall integrity at temperatures up to 100 °C. On increasing the temperature further to 150 °C, the nanotubes lost spatial volume. They suggested that this was possibly because of the loss of water from the FF nanotubes, and that the elevated temperature made the nanotubes more deformable as they became distorted by the AFM probe as part of the imaging process. Time-of-flight secondary ion mass spectrometry (ToF-SIMS) analysis suggested that at temperatures at and above 150 °C, the loss in mass and apparent degradation in the nanotubes morphology is due to the loss of phenylalanine (Sedman *et al.* 2006).

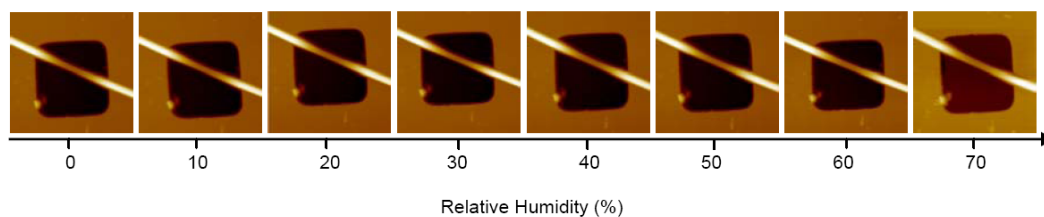
The present study showed that the value of E_{bending} gradually decreased ~30% at temperature from 24 °C to 100 °C. A possible reason could be that the increase in temperature increases the movement of FF peptides within the FF nanotube, which decreases the strength of the interactions between them. This, in-turn results in a decrease in E and G , also E_{bending} . However, since the decrease of E_{bending} was only ~30% at temperature from 24 °C to 100 °C, without changing the order of magnitude, the conclusion could be drawn that the elasticity as well as morphology of FF nanotubes remained stable (on the experimental time scale) as the temperature was increased from room temperature (24 °C) up to 100 °C. This is consistent with the previous studies (Adler-Abramovich *et al.* 2006; Sedman *et al.* 2006).

6.3.3 Effect of Humidity on the Elasticity of FF Nanotubes

In a similar manner to the temperature studies described in section 6.3.2, a study of the relation between the elasticity of FF nanotubes and humidity was carried out. The relative humidity was first decreased to near 0, and then increased to 70% in increments of 10%. Following each humidity increase the system was allowed to equilibrate for 5 minutes (details see section 2.1.2).

A sequence of images of the same fibril lying across a hole at humidities from 0 to 70% RH is displayed (**Figure 6-8 (i)**). The E_{bending} of three different fibrils in three different humidity experiments is also displayed (**Figure 6-8 (ii)**). There was no visible change in morphology of the fibrils from 0 to 70% RH. Nor was there an obvious relation between the E_{bending} and the relative humidity. For each fibril, the maximum difference of the E_{bending} at different relative humidity was less than 50%.

(i)



(ii)

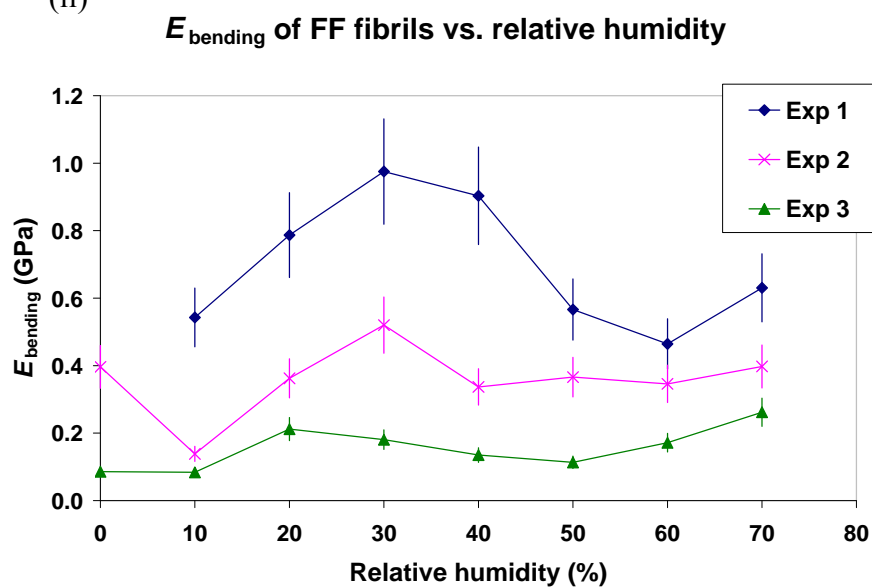


Figure 6-8 AFM images of FF nanotubes at different relative humidities. (i) A sequence of images of a same fibril lying across a hole at relative humidities from 0% to 70%. The size of each image is $10 \mu\text{m} \times 10 \mu\text{m}$. The Z-range of all the images in (i) is $1.07 \pm 0.02 \mu\text{m}$. (ii) E_{bending} of three different fibrils in three different humidity experiments (Niu *et al.* 2007).

6.4 Conclusion

A suspended beam configuration at the nanoscale can be produced when a protein nanotube is placed over a cavity within an underlying substrate. The elastic deformation of the suspended part of this nanoscale beam depends on the dimension of this beam, the suspended length, the loading force on the beam and also the elasticity of this beam (Gere 1991). When imaging a protein nanotube over a cavity using AFM in contact mode, the AFM probe applies a certain loading force on the nanotube; at the same time information on the dimension of the nanotube and the suspended length can be obtained from AFM images. Therefore, the elasticity of the protein nanotube can be obtained (Salvetat *et al.* 1999; Kis *et al.* 2002; Niu *et al.* 2007). In this chapter, the work of applying bending beam model to FF nanotubes has been presented.

Using bending beam model, the Young's modulus 27 ± 4 GPa and the shear modulus 0.21 ± 0.03 GPa of FF fibrils were obtained. It has also been shown that FF nanotubes retained their rigidity at temperatures from room temperature up to 100 °C, and also relative humidities from 0 to 70%. This study has therefore provided a better understanding of the structure and properties of FF nanotubes. If FF nanotubes are to be used as biomaterials, such as scaffolds for metal wires and nanoelectromechanics (see section 1.3.3.3 for the applications of FF nanotubes), the knowledge of how their elastic properties vary with simple parameters such as temperature and humidity is essential.

For the type of investigation performed within this chapter, the bending beam method avoids difficulties with aligning the AFM tip on the middle of a single

nanotube, as is needed in direct force measurement (Kol *et al.* 2005). It also allows the shear modulus to be obtained along with the Young's modulus. The bending beam method also can provide a way to study the relation between the elasticity and the dimension of the nanotubes, as well as the environmental conditions (such as temperature, humidity and solution). However, the bending beam method is only suitable for protein nanotubes with relatively high Young's modulus.

Salvetat and co-workers (1995) applied bending beam model to single-walled carbon nanotube and obtained the Young's modulus ~ 1 TPa; Kis (2002), Kasas (2004) and co-workers applied the bending beam model to microtubules and suggested that the Young's modulus was ~ 2 GPa, with a lower limit of 100 MPa. The Young's modulus of FF fibrils obtained in the presented study was 27 GPa. Neither the attempt to apply bending beam model to $\beta 2$ -microglobulin fibrils nor to *Salmonella* flagellar filaments was successful. These protein nanotubes broke over the cavities of gold substrate under the forces associated with sample preparation and/or applied by the AFM tip during imaging. From other elasticity studies presented in the previous chapters (**chapter 4** and **5**) and in the literature (Trachtenberg and Hammel 1992; Gosal *et al.* 2005), these protein nanotubes have the Young's modulus on the order of 10^1 to 10^2 MPa. From all these available data, it seems that the lower limit of the Young's modulus of nanotubes or fibrils that the bending beam model can be applied to is on the order of 1 GPa.

Chapter 7 Final Conclusions: AFM is a Powerful Tool for Investigating the Properties of Protein Nanotubes

Protein nanotubes have a wide range of potential applications in biotechnology (see section 1.2.3, 1.3.2 and 1.3.3.3). A comprehensive understanding of their properties has therefore become a prerequisite for their use in rational materials design. In this thesis, a range of protein nanotubes have been investigated by AFM as examples to develop methods of obtaining the structural and mechanical information of protein nanotubes. In this final chapter, the methods presented in previous chapters will be compared, in addition to a summary of the protein nanotube property data obtained.

7.1 AFM Methods of Investigating Protein Nanotubes

AFM is capable of visualizing and monitoring dynamic processes. Not only could the change in morphology of protein nanotubes be visualized, but also changes in their mechanical properties were monitored as dynamic processes. For example, changes in the morphology (see section 3.2) and flexibility (see section 4.3) of lysozyme fibrils during fibrillization were investigated. As another example, the morphologies and the elasticities of FF nanotubes were monitored as temperatures were increased from room temperature to 100 °C (see section 6.3.2).

Chapters 4 to 6 describe a range of different methods to obtain the mechanical properties of protein nanotubes. Historically, the indentation method has been used to obtain the elastic properties of samples using AFM. The indentation method is based on pressing the AFM probe into the nanotube sample surface, and the contact region of the resulting force-versus-distance curves used to provide quantitative information on its elastic properties. However, this method was not suitable for most of the protein nanotubes analysed within this thesis. For instance, the diameters of the protein nanotubes investigated in this thesis were typically in the range of 5-200 nm. Commonly used silicon nitride AFM probes have a nominal tip radius of 20 nm (manufacturer's data; Veeco Probes, Camarillo, CA, USA; also see section 2.1.2). Practically it was therefore difficult to accurately locate the tip onto the centre of a protein nanotube. Even if possible, a small uncertainty in location can result in a significant error in calculating the elasticity of the protein nanotubes (Sun *et al.* 2004). In addition, since the protein nanotubes are soft and thin, the underlying substrate modulus may interfere with the force-versus-distance curves, therefore interfere with the resulting elasticity of the sample obtained by indentation method. Active indentation into the protein nanotubes may also break the stress-strain linearity of the protein nanotubes. Therefore, alternative AFM methods needed to be developed/utilized to obtain the mechanical properties of protein nanotubes under investigation within this thesis.

The persistence length method, adhesive interaction method and bending beam method were described and utilized within chapters 4-6. All of these methods had the ability to investigate relationships between the elastic properties of protein nanotubes and other factors, such as the solution environment (section 4.2 and 5.2),

substrate (section 4.2), temperature (section 6.3.2) and humidity (section 6.3.3). However, each method was found only to be suitable for protein nanotubes with elasticities within a certain range. For example, the bending beam method was found to be suitable for protein nanotubes with Young's moduli above 1GPa. The persistence length method was found to be suitable for protein nanotubes with Young's moduli on the order of 10^1 to 10^2 MPa. Although, theoretically the adhesive interaction method was suitable for protein nanotubes with a wider range of Young's moduli, it required the protein nanotubes to be immobilised onto the substrate surface in liquid.

7.2 The Mechanical Properties of Protein Nanotubes

The protein nanotubes investigated by AFM in this thesis included *Salmonella* flagellar filaments, lysozyme fibrils and FF nanotubes. *Salmonella* flagellar filaments were found to have a Young's modulus of 22 ± 4 MPa (from the persistence length method) or from 7.2 MPa to 20.5 MPa (from the adhesive interaction method). Lysozyme fibrils of different assembly levels were found to have an average Young's modulus 3.3 GPa (from persistence length method). FF nanotubes were found to have a Young's modulus 27 ± 4 GPa (from the bending beam method).

The Young's modulus of a range of materials (Alonso and Goldmann 2003) is shown in **Figure 7-1**. Putting the presented results in this thesis onto this Young's modulus scale (shown by blue arrows in **Figure 7-1**), provides us better idea when it comes to rational materials design. All of the investigated protein nanotube structures had Young's moduli lying between that of gelatin and bone (**Figure 7-1**). This strongly highlights their potential, in terms of mechanical properties, for a

range of applications including drug-delivery systems, tissue-engineering scaffolds, 3D cell culture and templating. (see section 1.2.3, 1.3.2 and 1.3.3.3).

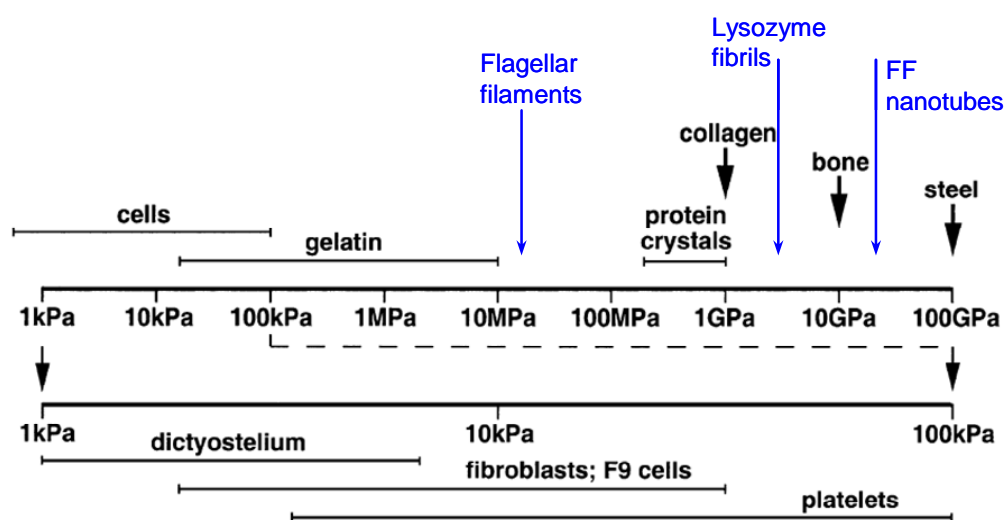


Figure 7-1 Young’s modulus of different materials. The diagram shows a spectrum from very hard to very soft materials: steel > bone > collagen > protein crystals > gelatin > rubber > cells (figure adapted from Alonso and Goldmann 2003).

7.3 Future Directions

As summarised in section 7.2, the mechanical properties of three different protein nanotubes have been putting onto the Yong’s modulus scale of materials. In future, if a database of mechanical properties of protein nanotubes could be built up using the AFM methods developed and utilized within this thesis, the development of the applications of protein nanotubes will be well accelerated, as the right protein nanotubes will be utilized for the right applications.

As accessories of the main aim of this thesis, which has been summarised in section 7.1 and 7.2, some of the results also inspired other directions of study. For instance, the circular structure of lysozyme fibrils were observed at the later stage of fibrillization (see section 3.2.4) without the need of high hydrostatic pressure nor the addition of organic solvents (Jasen 2004; Grudzielanek et al. 2005). Further and more in depth investigation into this matter may provide better understanding on the fibrillization mechanism of amyloid fibrils, which may be useful for understanding the amyloid related diseases and manipulating fibrillization for applications.

References

Adami, R.; Choquet, D.; Grazi, E., Rhodamine phalloidin F-actin - Critical concentration versus tensile strength. *European Journal of Biochemistry* **1999**, 263, (1), 270-275.

Adler-Abramovich, L.; Reches, M.; Sedman, V. L.; Allen, S.; Tendler, S. J. B.; Gazit, E., Thermal and chemical stability of diphenylalanine peptide nanotubes: Implications for nanotechnological applications. *Langmuir* **2006**, 22, (3), 1313-1320.

Allen, S.; Chen, X. Y.; Davies, J.; Davies, M. C.; Dawkes, A. C.; Edwards, J. C.; Roberts, C. J.; Sefton, J.; Tendler, S. J. B.; Williams, P. M., Detection of antigen-antibody binding events with the atomic force microscope. *Biochemistry* **1997**, 36, (24), 7457-7463.

Allison, D. P.; Hinterdorfer, P.; Han, W. H., Biomolecular force measurements and the atomic force microscope. *Current Opinion in Biotechnology* **2002**, 13, (1), 47-51.

Ban, T.; Yamaguchi, K.; Goto, Y., Direct observation of amyloid fibril growth, propagation, and adaptation. *Accounts of Chemical Research* **2006**, 39, (9), 663-670.

Baumann, C. G.; Smith, S. B.; Bloomfield, V. A.; Bustamante, C., Ionic effects on the elasticity of single DNA molecules. *Proceedings of the National Academy of Sciences of the United States of America* **1997**, 94, (12), 6185-6190.

Berg, H. C., The rotary motor of bacterial flagella. *Annual Review of Biochemistry* **2003**, 72, 19-54.

Berry, R. M.; Armitage, J. P., The bacterial flagella motor. *Advances in Microbial Physiology*, **1999**, 41, 291-337.

Binnig, G.; Quate, C. F.; Gerber, C., Atomic Force Microscope. *Physical Review Letters* **1986**, 56, (9), 930-933.

Blair, D. F., Flagellar movement driven by proton translocation. *Febs Letters* **2003**, 545, (1), 86-95.

Bong, D. T.; Clark, T. D.; Granja, J. R.; Ghadiri, M. R., Self-assembling organic nanotubes. *Angewandte Chemie-International Edition* **2001**, 40, (6), 988-1011.

Bong, D. T.; Ghadiri, M. R., Self-assembling cyclic peptide cylinders as nuclei for crystal engineering. *Angewandte Chemie-International Edition* **2001**, 40, (11), 2163-2166.

Bottomley, L. A.; Coury, J. E.; First, P. N., Scanning probe microscopy. *Analytical Chemistry* **1996**, 68, (12), R185-R230.

Bowen, W. R.; Lovitt, R. W.; Wright, C. J., Application of atomic force microscopy to the study of micromechanical properties of biological materials. *Biotechnology Letters* **2000**, 22, (11), 893-903.

Butt, H. J.; Cappella, B.; Kappl, M., Force measurements with the atomic force microscope: Technique, interpretation and applications. *Surface Science Reports* **2005**, 59, (1-6), 1-152.

Cappella, B.; Dietler, G., Force-distance curves by atomic force microscopy. *Surface Science Reports* **1999**, 34, 1-3.

Carrion-Vazquez, M.; Oberhauser, A. F.; Fisher, T. E.; Marszalek, P. E.; Li, H. B.; Fernandez, J. M., Mechanical design of proteins-studied by single-molecule force spectroscopy and protein engineering. *Progress in Biophysics & Molecular Biology* **2000**, *74*, (1-2), 63-91.

Chamberlain, A. K.; MacPhee, C. E.; Zurdo, J.; Morozova-Roche, L. A.; Hill, H. A. O.; Dobson, C. M.; Davis, J. J., Ultrastructural organization of amyloid fibrils by atomic force microscopy. *Biophysical Journal* **2000**, *79*, (6), 3282-3293.

Chen, R. J.; Bangsaruntip, S.; Drouvalakis, K. A.; Kam, N. W. S.; Shim, M.; Li, Y. M.; Kim, W.; Utz, P. J.; Dai, H. J., Noncovalent functionalization of carbon nanotubes for highly specific electronic biosensors. *Proceedings of the National Academy of Sciences of the United States of America* **2003**, *100*, (9), 4984-4989.

Chiti, F.; Dobson, C. M., Protein misfolding, functional amyloid, and human disease. *Annual Review of Biochemistry* **2006**, *75*, 333-366.

Dammer, U.; Hegner, M.; Anselmetti, D.; Wagner, P.; Dreier, M.; Huber, W.; Guntherodt, H. J., Specific antigen/antibody interactions measured by force microscopy. *Biophysical Journal* **1996**, *70*, (5), 2437-2441.

Dammer, Y.; Hegner, M.; Anselmetti, D.; Wagner, P.; Dreier, M.; Huber, W.; Guntherodt, H. J., Specific antigen/antibody interactions measured by force microscopy. *Biophysical Journal* **1996**, *70*, (5), 2437-2441.

Djalali, R.; Chen, Y. F.; Matsui, H., Au nanocrystal growth on nanotubes controlled by conformations and charges of sequenced peptide templates. *Journal of the American Chemical Society* **2003**, *125*, (19), 5873-5879.

Dobson, C. M., Protein misfolding, evolution and disease. *Trends in Biochemical Sciences* **1999**, 24, (9), 329-332.

Dobson, C. M.; Sali, A.; Karplus, M., Protein folding: A perspective from theory and experiment. *Angewandte Chemie-International Edition* **1998**, 37, (7), 868-893.

Dufrene, Y. F., Atomic force microscopy, a powerful tool in microbiology. *Journal of Bacteriology* **2002**, 184, (19), 5205-5213.

Dupres, V.; Verbelen, C.; Dufrene, Y. F., Probing molecular recognition sites on biosurfaces using AFM. *Biomaterials* **2007**, 28, (15), 2393-2402.

Ebbesen, T. W.; Ajayan, P. M., Large-scale Synthesis of Carbon Nanotubes. *Nature* **1992**, 358, (6383), 220-222.

Engel, A.; Muller, D. J., Observing single biomolecules at work with the atomic force microscope. *Nature Structural Biology* **2000**, 7, (9), 715-718.

Fan, F.; Ohnishi, K.; Francis, N. R.; Macnab, R. M., The FliP and FliR proteins of *Salmonella typhimurium*, putative components of the type III flagellar export apparatus, are located in the flagellar basal body. *Molecular Microbiology* **1997**, 26, (5), 1035-1046.

Fennimore, A. M.; Yuzvinsky, T. D.; Han, W. Q.; Fuhrer, M. S.; Cumings, J.; Zettl, A., Rotational actuators based on carbon nanotubes. *Nature* **2003**, 424, (6947), 408-410.

Fisher, T. E.; Marszalek, P. E.; Oberhauser, A. F.; Carrion-Vazquez, M.; Fernandez, J. M., The micro-mechanics of single molecules studied with atomic force microscopy. *Journal of*

Physiology-London **1999**, 520, (1), 5-14.

Fisher, T. E.; Oberhauser, A. F.; CarrionVazquez, M.; Marszalek, P. E.; Fernandez, J. M., The study of protein mechanics with the atomic force microscope (vol 24, pg 379, 1999). *Trends in Biochemical Sciences* **2000**, 25, (1), 6-6.

Florin, E. L.; Moy, V. T.; Gaub, H. E., Adhesion Forces between Individual Ligand-receptor Pairs. *Science* **1994**, 264, (5157), 415-417.

Friedsam, C.; Seitz, M.; Gaub, H. E., Investigation of polyelectrolyte desorption by single molecule force spectroscopy. *Journal of Physics-Condensed Matter* **2004**, 16, (26), S2369-S2382.

Fukasaku, K.; Takeda, K.; Shiraishi, K., First-principles study on electronic structures of protein nanotubes. *Journal of the Physical Society of Japan* **1998**, 67, (11), 3751-3760.

Gao, X. Y.; Matsui, H., Peptide-based nanotubes and their applications in bionanotechnology. *Advanced Materials* **2005**, 17, (17), 2037-2050.

Gazit, E., A possible role for pi-stacking in the self-assembly of amyloid fibrils. *Faseb Journal* **2002**, 16, (1), 77-83.

Gere, J. M.; Timoshenko, S. P., *Mechanics of Materials*. Third SI ed.; Chapman and Hall, London: 1991.

Ghadiri, M. R.; Granja, J. R.; Milligan, R. A.; McRee, D. E.; Khazanovich, N., Self-assembling Organic Nanotubes Based on a Cyclic Peptide Architecture. *Nature* **1993**, 366, (6453), 324-327.

- Goldsbury, C.; Frey, P.; Olivieri, V.; Aebi, U.; Muller, S. A., Multiple assembly pathways underlie amyloid-beta fibril polymorphisms. *Journal of Molecular Biology* **2005**, 352, (2), 282-298.
- Gorbitz, C. H., The structure of nanotubes formed by diphenylalanine, the core recognition motif of Alzheimer's beta-amyloid polypeptide. *Chemical Communications* **2006**, (22), 2332-2334.
- Gras, S. L., Amyloid fibrils: From disease to design. New biomaterial applications for self-assembling cross-beta fibrils. *Australian Journal of Chemistry* **2007**, 60, (5), 333-342.
- Gras, S. L., Protein misfolding: a route to new nanomaterials. *Advanced Powder Technology* **2007**, 18, (6), 699-705.
- Greig, L. M.; Philp, D., Applying biological principles to the assembly and selection of synthetic superstructures. *Chemical Society Reviews* **2001**, 30, (5), 287-302.
- Grimbergen, J. A.; Visscher, K.; Demesquita, D. S. G.; Brakenhoff, G. J., Isolation of Single Yest-cells by Optical Trapping. *Yeast* **1993**, 9, (7), 723-732.
- Guo, T.; Nikolaev, P.; Rinzler, A. G.; Tomanek, D.; Colbert, D. T.; Smalley, R. E., Self-assembly of Tubular Fullerenes. *Journal of Physical Chemistry* **1995 (a)**, 99, (27), 10694-10697.
- Guo, T.; Nikolaev, P.; Thess, A.; Colbert, D. T.; Smalley, R. E., Catalytic Growth of Single-walled Nanotubes by Laser Vaporization. *Chemical Physics Letters* **1995 (b)**, 243, (1-2), 49-54.

Hansma, H. G.; Bezanilla, M.; Zenhausern, F.; Adrian, M.; Sinsheimer, R. L., Atomic Force Microscopy of DNA in Aqueous-Solutions. *Nucleic Acids Research* **1993**, 21, (3), 505-512.

Hansma, H. G.; Sinsheimer, R. L.; Li, M. Q.; Hansma, P. K., Atomic Force Microscopy of Single-stranded and Double-stranded DNA. *Nucleic Acids Research* **1992**, 20, (14), 3585-3590.

Harata, K.; Muraki, M.; Jigami, Y., Role of ARG115 in the Catalytic Action of Human Lysozyme – X-Ray Structure of HIS115 and GLU115 and Glu115 Mutants. *Journal of Molecular Biology* **1993**, 233, (3), 524-535.

Harper, J. D.; Lansbury, P. T., Models of amyloid seeding in Alzheimer's disease and scrapie: Mechanistic truths and physiological consequences of the time-dependent solubility of amyloid proteins. *Annual Review of Biochemistry* **1997**, 66, 385-407.

Heinz, W. F.; Hoh, J. H., Relative surface charge density mapping with the atomic force microscope. *Biophysical Journal* **1999**, 76, (1), 528-538.

Hinterdorfer, P.; Baumgartner, W.; Gruber, H. J.; Schilcher, K.; Schindler, H., Detection and localization of individual antibody-antigen recognition events by atomic force microscopy. *Proceedings of the National Academy of Sciences of the United States of America* **1996**, 93, (8), 3477-3481.

Homma, M.; Iino, T., Locations of Hook-associated Proteins in Flagellar Structures of *Salmonella typhimurium*. *Journal of Bacteriology* **1985**, 162, (1), 183-189.

Inaka, K.; Kuroki, R.; Kikuchi, M.; Matsushima, M., Crystal-structures of the Apomutant and

Holomutant Human Lysozymes with an Introduced Ca²⁺ Binding-site. *Journal of Biological Chemistry* **1991**, 266, (31), 20666-20671.

Israelachvili, J. N., *Intermolecular and Surface Forces*. 2nd ed.; Academic Press: San Diego, CA, USA, 1992.

Jansen, R.; Dzwolak, W.; Winter, R., Amyloidogenic self-assembly of insulin aggregates probed by high resolution atomic force microscopy. *Biophysical Journal* **2005**, 88, (2), 1344-1353.

Jansen, R.; Grudzielanek, S.; Dzwolak, W.; Winter, R., High pressure promotes circularly shaped insulin amyloid. *Journal of Molecular Biology* **2004**, 338, (2), 203-206.

Kamiya, R.; Asakura, S., Flagellar Transformations at Alkaline pH. *Journal of Molecular Biology* **1976 (a)**, 108, (2), 513-518.

Kamiya, R.; Asakura, S., Helical Transformations of Salmonella Flagella in vitro. *Journal of Molecular Biology* **1976 (b)**, 106, (1), 167-186.

Khurana, R.; Ionescu-Zanetti, C.; Pope, M.; Li, J.; Nielson, L.; Ramirez-Alvarado, M.; Regan, L.; Fink, A. L.; Carter, S. A., A general model for amyloid fibril assembly based on morphological studies using atomic force microscopy. *Biophysical Journal* **2003**, 85, (2), 1135-1144.

Kis, A.; Kasas, S.; Babic, B.; Kulik, A. J.; Benoit, W.; Briggs, G. A. D.; Schonenberger, C.; Catsicas, S.; Forro, L., Nanomechanics of microtubules. *Physical Review Letters* **2002**, 89, (24), 248101.

Kohli, P.; Martin, C. R., Smart nanotubes for biotechnology. *Current Pharmaceutical Biotechnology* **2005**, 6, (1), 35-47.

Kol, N.; Adler-Abramovich, L.; Barlam, D.; Shneck, R. Z.; Gazit, E.; Rousso, I., Self-assembled peptide nanotubes are uniquely rigid bioinspired supramolecular structures. *Nano Letters* **2005**, 5, (7), 1343-1346.

Krebs, M. R. H.; Wilkins, D. K., Formation and seeding of amyloid fibrils from wild-type hen lysozyme and a peptide fragment from the beta-domain. *Journal of Molecular Biology* **2000**, 300, (3), 541-549.

Krejcová, K.; Rabisková, M., Nano- and microtubes for drugs. *Chemické Listy* **2008**, 102, (1), 35-39.

Kubori, T.; Matsushima, Y.; Nakamura, D.; Uralil, J.; Lara-Tejero, M.; Sukhan, A.; Galan, J. E.; Aizawa, S., Supramolecular structure of the Salmonella typhimurium type III protein secretion system. *Science* **1998**, 280, (5363), 602-605.

Kumara, M. T.; Srividya, N.; Muralidharan, S.; Tripp, B. C., Bioengineered flagella protein nanotubes with cysteine loops: Self-assembly and manipulation in an optical trap. *Nano Letters* **2006**, 6, (9), 2121-2129.

Kumara, M. T.; Tripp, B. C.; Muralidharan, S., Self-assembly of metal nanoparticles and nanotubes on bioengineered flagella scaffolds. *Chemistry of Materials* **2007**, 19, (8), 2056-2064.

Lee, G. U.; Kidwell, D. A.; Colton, R. J., Sensing Discrete Streptavidin Biotin Interactions with Atomic-Force Microscopy. *Langmuir* **1994**, 10, (2), 354-357.

Li, W. Z.; Xie, S. S.; Qian, L. X.; Chang, B. H.; Zou, B. S.; Zhou, W. Y.; Zhao, R. A.; Wang, G., Large-scale synthesis of aligned carbon nanotubes. *Science* **1996**, 274, (5293), 1701-1703.

Lyubchenko, Y. L.; Oden, P. I.; Lampner, D.; Lindsay, S. M.; Dunker, K. A., Atomic Force Microscopy of DNA and Bacteriophage in Air, Water and Propanol – the Role of Adhesion Forces. *Nucleic Acids Research* **1993**, 21, (5), 1117-1123.

Makin, O. S.; Serpell, L. C., Structures for amyloid fibrils. *Febs Journal* **2005**, 272, (23), 5950-5961.

Marti, O.; Elings, V.; Haugan, M.; Bracker, C. E.; Schneir, J.; Drake, B.; Gould, S. A. C.; Gurley, J.; Hellemans, L.; Shaw, K.; Weisenhorn, A. L.; Zasadzinski, J.; Hansma, P. K., Scanning Probe Microscopy of Biological Samples and Other Surfaces. *Journal of Microscopy-Oxford* **1988**, 152, 803-809.

Melosh, N. A.; Boukai, A.; Diana, F.; Gerardot, B.; Badolato, A.; Petroff, P. M.; Heath, J. R., Ultrahigh-density nanowire lattices and circuits. *Science* **2003**, 300, (5616), 112-115.

Merrill, E. W.; Dennison, K. A.; Sung, C., Partitioning and Diffusion of Solutes in Hydrogels of Poly (Ethylene Oxide). *Biomaterials* **1993**, 14, (15), 1117-1126.

Mesibov, R.; Adler, J., Chemotaxis toward Amino-acids in Escherichia-coli. *Journal of Bacteriology* **1972**, 112, (1), 315.

Minamino, T.; Macnab, R. M., Components of the Salmonella flagellar export apparatus and classification of export substrates. *Journal of Bacteriology* **1999**, 181, (5), 1388-1394.

- Modi, A.; Koratkar, N.; Lass, E.; Wei, B. Q.; Ajayan, P. M., Miniaturized gas ionization sensors using carbon nanotubes. *Nature* **2003**, 424, (6945), 171-174.
- Namba, K.; Vonderviszt, F., Molecular architecture of bacterial flagellum. *Quarterly Reviews of Biophysics* **1997**, 30, (1), 1-65.
- Niu, L. J.; Chen, X. Y.; Allen, S.; Tendler, S. J. B., Using the bending beam model to estimate the elasticity of diphenylalanine nanotubes. *Langmuir* **2007**, 23, (14), 7443-7446.
- Noy, A.; Vezenov, D. V.; Kayyem, J. F.; Meade, T. J.; Lieber, C. M., Stretching and breaking duplex DNA by chemical force microscopy. *Chemistry & Biology* **1997**, 4, (7), 519-527.
- Ohnishi, K.; Ohto, Y.; Aizawa, S. I.; Macnab, R. M.; Iino, T., FLGD Is a Scaffolding Protein Needed for Flagellar Hook Assembly in *Salmonella*-typhimurium. *Journal of Bacteriology* **1994**, 176, (8), 2272-2281.
- Okamoto, H.; Takeda, K.; Shiraishi, K., First-principles study of the electronic and molecular structure of protein nanotubes. *Physical Review B* **2001**, 64, (11).
- Perutz, M. F.; Finch, J. T.; Berriman, J.; Lesk, A., Amyloid fibers are water-filled nanotubes. *Proceedings of the National Academy of Sciences of the United States of America* **2002**, 99, (8), 5591-5595.
- Radmacher, M.; Tillmann, R. W.; Fritz, M.; Gaub, H. E., From Molecules to Cells – Imaging Soft Samples with the Atomic Force Microscop. *Science* **1992**, 257, (5078), 1900-1905.
- Ralston, J.; Larson, I.; Rutland, M. W.; Feiler, A. A.; Kleijn, M., Atomic force microscopy and direct surface force measurements - (IUPAC technical report). *Pure and Applied*

Chemistry **2005**, 77, (12), 2149-2170.

Reches, M.; Gazit, E., Casting metal nanowires within discrete self-assembled peptide nanotubes. *Science* **2003**, 300, (5619), 625-627.

Reches, M.; Gazit, E., Formation of closed-cage nanostructures by self-assembly of aromatic dipeptides. *Nano Letters* **2004**, 4, (4), 581-585.

Reich, Z.; Kapon, R.; Nevo, R.; Pilpel, Y.; Zmora, S.; Scolnik, Y., Scanning force microscopy in the applied biological sciences. *Biotechnology Advances* **2001**, 19, (6), 451-485.

Rief, M.; Gautel, M.; Oesterhelt, F.; Fernandez, J. M.; Gaub, H. E., Reversible unfolding of individual titin immunoglobulin domains by AFM. *Science* **1997**, 276, (5315), 1109-1112.

Rossell, J., Protein Immobilization for AFM. PhD Thesis, University of Nottingham, **2003**.

Salvetat, J. P.; Briggs, G. A. D.; Bonard, J. M.; Bacsá, R. R.; Kulik, A. J.; Stockli, T.; Burnham, N. A.; Forro, L., Elastic and shear moduli of single-walled carbon nanotube ropes. *Physical Review Letters* **1999**, 82, (5), 944-947.

Santos, N. C.; Castanho, M., An overview of the biophysical applications of atomic force microscopy. *Biophysical Chemistry* **2004**, 107, (2), 133-149.

Sarikaya, M.; Tamerler, C.; Jen, A. K. Y.; Schulten, K.; Baneyx, F., Molecular biomimetics: nanotechnology through biology. *Nature Materials* **2003**, 2, (9), 577-585.

Scheibel, T., Protein fibers as performance proteins: new technologies and applications. *Current Opinion in Biotechnology* **2005**, 16, (4), 427-433.

Scheibel, T.; Parthasarathy, R.; Sawicki, G.; Lin, X. M.; Jaeger, H.; Lindquist, S. L., Conducting nanowires built by controlled self-assembly of amyloid fibers and selective metal deposition. *Proceedings of the National Academy of Sciences of the United States of America* **2003**, 100, (8), 4527-4532.

Sedman, V. L.; Adler-Abramovich, L.; Allen, S.; Gazit, E.; Tendler, S. J. B., Direct observation of the release of phenylalanine from diphenylalanine nanotubes. *Journal of the American Chemical Society* **2006**, 128, (21), 6903-6908.

Seo, Y.; Jhe, W., Atomic force microscopy and spectroscopy. *Reports on Progress in Physics* **2008**, 71, (1).

Seymour, F. W. K.; Doetsch, R. N., Chemotactic Responses by Motile Bacteria. *Journal of General Microbiology* **1973**, 78, (OCT), 287-296.

Shao, Z. F.; Mou, J.; Czajkowsky, D. M.; Yang, J.; Yuan, J. Y., Biological atomic force microscopy: What is achieved and what is needed. *Advances in Physics* **1996**, 45, (1), 1-86.

Sipe, J. D.; Cohen, A. S., Review: History of the amyloid fibril. *Journal of Structural Biology* **2000**, 130, (2-3), 88-98.

Smith, J. F.; Knowles, T. P. J.; Dobson, C. M.; MacPhee, C. E.; Welland, M. E., Characterization of the nanoscale properties of individual amyloid fibrils. *Proceedings of the National Academy of Sciences of the United States of America* **2006**, 103, (43), 15806-15811.

Song, Y. J.; Challa, S. R.; Medforth, C. J.; Qiu, Y.; Watt, R. K.; Pena, D.; Miller, J. E.; van Swol, F.; Shelnut, J. A., Synthesis of peptide-nanotube platinum-nanoparticle composites.

Chemical Communications **2004**, (9), 1044-1045.

Srigiriraju, S. V.; Powers, T. R., Continuum model for polymorphism of bacterial flagella. *Phys Rev Lett* **2005**, 94, (24), 248101.

Stark, M.; Moller, C.; Muller, D. J.; Guckenberger, R., From images to interactions: High-resolution phase imaging in tapping-mode atomic force microscopy. *Biophysical Journal* **2001**, 80, (6), 3009-3018.

Steubing, R. W.; Cheng, S.; Wright, W. H.; Numajiri, Y.; Berns, M. W., Single Beam Optical Trapping and Micro manipulation of Mammalian-cells. *Proceedings of Laser-Tissue Interaction*, **1990**, 1202, 272-280.

Sun, Y. J.; Akhremitchev, B.; Walker, G. C., Using the adhesive interaction between atomic force microscopy tips and polymer surfaces to measure the elastic modulus of compliant samples. *Langmuir* **2004**, 20, (14), 5837-5845.

Tso, W. W.; Adler, J., Negative Chemotaxis in Escherichia-coli. *Journal of Bacteriology* **1974**, 118, (2), 560-576.

Vesenka, J.; Guthold, M.; Tang, C. L.; Keller, D.; Delaine, E.; Bustamante, C., Substrate Preparation for Reliable Imaging of DNA-molecules with the Scanning Force Microscope. *Ultramicroscopy* **1992**, 42, 1243-1249.

Vinckier, A.; Gervasoni, P.; Zaugg, F.; Ziegler, U.; Lindner, P.; Groscurth, P.; Pluckthun, A.; Semenza, G., Atomic force microscopy detects changes in the interaction forces between GroEL and substrate proteins. *Biophysical Journal* **1998**, 74, (6), 3256-3263.

Waterhouse, S. H.; Gerrard, J. A., Amyloid fibrils in bionanotechnology. *Australian Journal of Chemistry* **2004**, *57*, (6), 519-523.

Weisenhorn, A. L.; Hansma, P. K.; Albrecht, T. R.; Quate, C. F., Forces in Atomic Force Microscopy in Air and Water. *Applied Physics Letters* **1989**, *54*, (26), 2651-2653.

Weisenhorn, A. L.; Maivald, P.; Butt, H. J.; Hansma, P. K., Measuring Adhesion, Attraction, and Repulsion between Surfaces in Liquids with an Atomic Force Microscope. *Physical Review B* **1992**, *45*, (19), 11226-11232.

West, P.; Starostina, N., A Guide to AFM Image Artifacts (version 1.2). <URL: <http://www.pacificnanotech.com/afm-artifacts.html>> [accessed 10 Oct 2008]

Williams, P. M.; Shakesheff, K. M.; Davies, M. C.; Jackson, D. E.; Roberts, C. J.; Tendler, S. J. B., Blind reconstruction of scanning probe image data. *Journal of Vacuum Science & Technology B* **1996**, *14*, (2), 1557-1562.

Woods, R. D.; Takahashi, N.; Aslam, A.; Pleass, R. J.; Aizawa, S. I.; Sockett, R. E., Bifunctional nanotube scaffolds for diverse ligands are purified simply from *Escherichia coli* strains coexpressing two functionalized flagellar genes. *Nano Letters* **2007**, *7*, (6), 1809-1816.

Yemini, M.; Reches, M.; Gazit, E.; Rishpon, J., Peptide nanotube-modified electrodes for enzyme-biosensor applications. *Analytical Chemistry* **2005** (a), *77*, (16), 5155-5159.

Yemini, M.; Reches, M.; Rishpon, J.; Gazit, E., Novel electrochemical biosensing platform using self-assembled peptide nanotubes. *Nano Letters* **2005** (b), *5*, (1), 183-186.

Yonekura, K.; Maki-Yonekura, S.; Namba, K., Growth mechanism of the bacterial flagellar

filament. *Research in Microbiology* **2002**, 153, (4), 191-197.

Yonekura, K.; Maki-Yonekura, S.; Namba, K., Complete atomic model of the bacterial flagellar filament by electron cryomicroscopy. *Nature* **2003**, 424, (6949), 643-650.

Zasadzinski, J. A. N.; Schneir, J.; Gurley, J.; Elings, V.; Hansma, P. K., Scanning Tunneling Microscopy of Freeze-fracture Replicas of Biomembranes. *Science* **1988**, 239, (4843), 1013-1015.

Zhang, S. G., Fabrication of novel biomaterials through molecular self-assembly. *Nature Biotechnology* **2003**, 21, (10), 1171-1178.

Zhao, X. B.; Pan, F.; Lu, J. R., Recent development of peptide self-assembly. *Progress in Natural Science* **2008**, 18, (6), 653-660.

Zhong, Z. H.; Wang, D. L.; Cui, Y.; Bockrath, M. W.; Lieber, C. M., Nanowire crossbar arrays as address decoders for integrated nanosystems. *Science* **2003**, 302, (5649), 1377-1379.

Zlatanova, J.; Lindsay, S. M.; Leuba, S. H., Single molecule force spectroscopy in biology using the atomic force microscope. *Progress in Biophysics & Molecular Biology* **2000**, 74, (1-2), 37-61.

Publication

The following article based on some of the work in this thesis was published during the course of this project.

Niu, L. J.; Chen, X. Y.; Allen, S.; Tandler, S. J. B., Using the bending beam model to estimate the elasticity of diphenylalanine nanotubes. *Langmuir* **2007**, *23*, (14), 7443-7446.

Using the Bending Beam Model to Estimate the Elasticity of Diphenylalanine Nanotubes

Lijiang Niu, Xinyong Chen, Stephanie Allen, and Saul J. B. Tendler*

Laboratory of Biophysics and Surface Analysis, School of Pharmacy, The University of Nottingham, Nottingham NG7 2RD, U.K.

Received April 6, 2007. In Final Form: May 18, 2007

The core recognition motif of the amyloidogenic β -amyloid polypeptide, diphenylalanine peptide, has previously been shown to self-assemble into discrete, well-ordered, stiff nanotubes under mild conditions. The nanotubes keep the same morphology from room temperature up to 100 °C. In the presented study, we applied the bending beam model to atomic force microscopy images of diphenylalanine nanotubes suspended across cavities and obtained the Young's modulus 27 ± 4 GPa and the shear modulus 0.21 ± 0.03 GPa. We also showed that the elasticity of these nanotubes is stable within the same temperature range and at relative humidity from 0% to 70%. This study furthers our understanding of the structure and properties of these nanotubes, which are important for their potential applications in biotechnology.

Introduction

Self-assembled protein and peptide nanotubes are attractive as potential building blocks for a variety of applications, including scaffolds for tissue engineering, nanowires in microelectronics, functionalized composite materials, and drug delivery devices, not only because of their biocompatibility and chemical manipulability, but also because of their large-scale production ability and simple experimental conditions.^{1–4} An understanding of the physical properties of such nanotubes is important for applications which demand structural performance.

The diphenylalanine peptide, NH₂-Phe-Phe-COOH, the core motif of the β -amyloid polypeptide, efficiently self-assembles into FF fibrils under mild conditions.^{5–7} Previous studies have shown that FF fibrils are hollow, water-filled structures ranging from 50 to 1000 nm in diameter and are discrete nanotubes with no branching. Studies have also suggested that there are pores on the FF nanotube walls, which run parallel to the axis of the fibril.⁸

In the current study, the elastic properties of FF nanotubes at different temperatures and humidities have been investigated using atomic force microscopy (AFM).

Materials and Methods

Preparation of FF Fibrils. FF peptide was purchased from Sigma-Aldrich (Gillingham, Dorset, UK). Fresh stock solutions were prepared by dissolving the lyophilized peptide in 1,1,1,3,3,3-hexafluoropropan-2-ol (HFIP) (Sigma-Aldrich) at a concentration of 100 mg/mL. Peptide stock solution was diluted in double distilled (dd) H₂O to a final concentration of 2 mg/mL. An aliquot of 10 μ L of the sample solution was then immediately dropped onto a UV-cleaned micropatterned silicon substrate (with holes of 5 μ m \times 5 μ m and 200 nm deep) and subsequently dried under a gentle flow of nitrogen. This protocol produced fibrils which occasionally lie over the holes of the substrate.

* E-mail: saul.tendler@nottingham.ac.uk

- (1) Gao, X. Y.; Matsui, H. *Adv. Mater.* **2005**, *17*, 2037–2050.
- (2) Scheibel, T. *Curr. Opin. Biotechnol.* **2005**, *4*, 427–433.
- (3) Yemini, M.; Reches, M.; Rishpon, J.; Gazit, E. *Nano Lett.* **2005**, *1*, 183–186.
- (4) Yemini, M.; Reches, M.; Gazit, E.; Rishpon, J. *Anal. Chem.* **2005**, *16*, 5155–5159.
- (5) Reches, M.; Gazit, E. *Science* **2003**, *5619*, 625–627.
- (6) Song, Y. J.; Challa, S. R.; Medforth, C. J.; Qiu, Y.; Watt, R. K.; Pena, D.; Miller, J. E.; van Swol, F.; Shelnutt, J. A. *Chem. Commun.* **2004**, *9*, 1044–1045.
- (7) Gazit, E. *FASEB J.* **2002**, *1*, 77–83.
- (8) Gorbitz, C. H. *Chem. Commun.* **2006**, *22*, 2332–2334.

Atomic Force Microscopy. For elasticity measurements at room temperature, AFM images were generated using a MultiMode AFM (Digital Instruments, Veeco Metrology Group, Santa Barbara, CA) with a J-type scanner. For elasticity at elevated temperatures and modified humidities, an EnviroScope AFM (eScope AFM) (Digital Instruments) was used. This AFM has an enclosed sample chamber allowing temperature control and a humidity range of 0–80% RH. All imaging was performed in air in contact mode using V-shaped levers (Veeco Metrology Group) with nominal spring constants of 0.06 N/m (manufacturer's data). Scan rates employed were 1.0–2.0 Hz. Data was analyzed using Scanning Probe Image Processor program (Image Metrology A/S, Denmark).

For temperature studies, samples were placed onto the stage and initially imaged at room temperature. The temperature was then increased from 30 to 130 °C with increments of 10 °C. Following each temperature increase, the system was allowed to equilibrate for 5 min before imaging commenced.

In a similar manner, the relative humidity was decreased to nearly 0% and then increased to 70% with increments of 10%. Following each humidity increase, the system was allowed to equilibrate for 5 min.

Theoretical Basis

As stated, the FF fibrils occasionally lie over the holes of the silicon grid, producing a suspended-beam configuration at the nanoscale. In contact mode of AFM operation, while the AFM tip is scanning over the fibril, it applies a loading force on the fibril, which can be considered as a concentrated load midway along the suspended length of the fibril (Figure 1). The elastic deformation of the suspended part of the fibril resulting from a concentrated load can be regarded as the sum of deflections due to bending and shearing. Neglecting end effects, the deflection in the middle of the suspended part of the fibril is

$$\begin{aligned} \delta &= \delta_B + \delta_S \\ &= FL^3/192EI + f_3FL/4GA \\ &= FL^3/192E_{\text{bending}}I \end{aligned} \quad (1)$$

where δ is the deflection, δ_B is the deflection due to bending, δ_S is the deflection due to shearing; E is the Young's modulus, G is the shear modulus; F is the loading force, L is the suspended length, A is the cross-sectional area of the fibril; I is the moment of inertia of area A ($I = \pi D^4/64$ for a filled circular area with diameter D ; $I = \pi(D_o^4 - D_i^4)/64$ for a circular area with outer

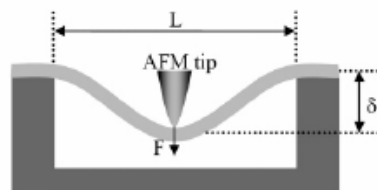


Figure 1. Schematic of the measurement. The FF fibrils occasionally lie over the holes of the silicon grid, producing a suspended beam configuration at the nanoscale. The AFM is used to apply a loading force to the fibril and to determine directly the resulting deflection.

diameter D_0 and inner diameter D_i); f_s is the form factor for shear determined by the geometry (equal to $10/9$ for a cylindrical beam); E_{bending} is the bending modulus that corresponds to the Young's modulus that would be deduced if shear deformations were neglected^{9–11}

The deflection δ , the suspended length L , and the second moment I can be obtained from the profiles of the AFM images of the fibrils. The F is AFM loading force on the fibril, which is considered as a concentrated force midway along the suspended length of the fibril.

From eq 1

$$1/E_{\text{bending}} = 1/E + (48f_s I/GA)(1/L^2) \quad (2)$$

Hence, for a fibril lying across several holes with different suspended lengths L , assuming that the geometry of the cross section remains the same along the fibril, the Young's modulus can be obtained from the intercept of the plot of $1/E_{\text{bending}}$ versus $1/L^2$ and the shear modulus can be obtained from the gradient.

Results

Elasticity at Room Temperature. An example of a fibril lying across five holes of the silicon grid is displayed (Figure 2). As can be observed, the fibril has different suspended lengths over each hole. For this fibril, its length exceeds the maximum scan size. The deformation of the suspended parts of the fibrils was reversible and increased linearly with increasing loading force (data not shown). Using the height determined from the profile of the cross section as the diameter D , E_{bending} could be obtained from eq 1. The graph of $1/E_{\text{bending}}$ against $1/L^2$ for this fibril is displayed in Figure 2(ii). From eq 2, assuming the geometry of the cross section was constant, the Young's modulus E is 27 ± 4 GPa and the shear modulus G is 0.21 ± 0.03 GPa.

Elasticity vs Temperature. A sequence of images of the same two fibrils from room temperature to 130°C is displayed (Figure 3(i)). There was no visible change in the morphology of the fibrils at temperatures up to 100°C . Higher temperatures caused the fibrils to begin to lose their structural integrity.^{12,13} The three lines in Figure 3(ii) show the value of E_{bending} for the three holes (a, b, c) corresponding to the left fibril in Figure 3(i) at temperatures from 24 to 100°C . The value of E_{bending} gradually decreased $\sim 30\%$ over this temperature range.

Elasticity vs Humidity. A sequence of images of a same fibril lying across a hole at humidity from 0% to 70% RH is

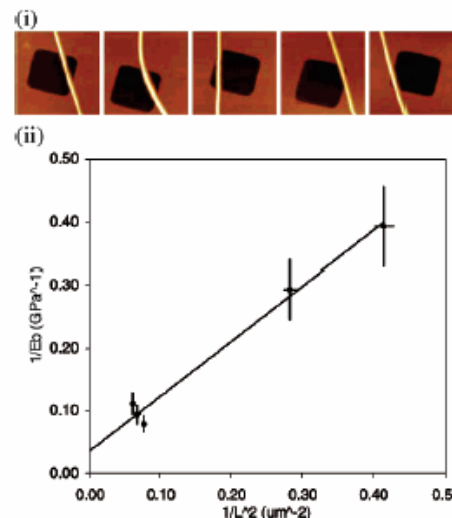


Figure 2. AFM images of a single FF nanotubes on a silicon grid. (i) One fibril lying across five holes of silicon grid, consequently with different suspended lengths L . The size of each image is $10 \mu\text{m} \times 10 \mu\text{m}$. From (i), the graph of $1/E_{\text{bending}}$ against $1/L^2$ of this fibril was obtained as shown in (ii).

displayed (Figure 4(i)). The E_{bending} of three different fibrils in three different elasticity vs humidity experiments is also displayed (Figure 4(ii)). There was no visible change in morphology of the fibrils from 0% to 70% RH, nor was there an obvious relation between the E_{bending} and the relative humidity. For each fibril, the maximum difference of the E_{bending} at different relative humidities was less than 50% .

Discussion

From direct force measurement (indentation experiments) in a previous AFM study, the Young's modulus of FF nanotubes was determined to be 19 GPa.¹⁴ For direct force measurement, in order to obtain the Young's modulus, the AFM tip has to be aligned at the center of a single nanotube surface and force-distance curves are acquired at the same position. The bending-beam model avoids the serious difficulty of aligning the AFM tip and also allows the shear modulus to be obtained.

For the bending-beam model, the boundary conditions are critical. The fibrils were usually several times longer than the size of the holes of the silicon grid; the position of the fibrils remained the same through AFM operation, so we could assume a fibril suspended on a hole was clamped at the two ends. The main source of experimental error comes from the determination of diameter D , because the bending modulus E_{bending} is related to the fourth power of D . As stated in the Results section, if the cross section of the fibril is a filled circular area, using the height determined from the profile of the cross section as the diameter D , the Young's modulus E is 27 ± 4 GPa and the shear modulus G is 0.21 ± 0.03 GPa. Using the width at the half-height as diameter D , E is 3.6 ± 0.6 GPa and G is 0.08 ± 0.01 GPa. The FF nanotubes are actually hollow tubes, but the inner diameter could not be obtained from AFM imaging. If the cross section of the fibril is a hollow circular area, assuming the inner diameter D_i is 70% of the outer diameter D_0 , using the width at the half-height as outer diameter D_0 , the resulting E is 4.7 ± 0.7 GPa and G is 0.15 ± 0.02 GPa, which does not change the order of

(9) Salvétat, J. P.; Erigys, G. A. D.; Bonard, J. M.; Baccsa, R. R.; Kulik, A. J.; Stockli, T.; Eumham, N. A.; Forno, L. *Phys. Rev. Lett.* **1999**, *5*, 944–947.

(10) Kis, A.; Kasas, S.; Babik, B.; Kulik, A. J.; Benoit, W.; Briggs, G. A. D.; Schonenberger, C.; Catsicas, S.; Forno, L. *Phys. Rev. Lett.* **2002**, *28*, 248101.

(11) Gere, J. M.; Timoshenko, S. P. *Mechanics of Materials*; Chapman and Hall: London, 1991.

(12) Adler-Abramovich, L.; Reches, M.; Sedman, V. L.; Allen, S.; Tendler, S. J. B.; Gazit, E. *Langmuir* **2006**, *3*, 1313–1320.

(13) Sedman, V. L.; Adler-Abramovich, L.; Allen, S.; Gazit, E.; Tendler, S. J. B. *J. Am. Chem. Soc.* **2006**, *21*, 6903–6908.

(14) Kol, N.; Adler-Abramovich, L.; Barlan, D.; Stueck, R. Z.; Gazit, E.; Rousso, I. *Nano Lett.* **2005**, *7*, 1343–1346.

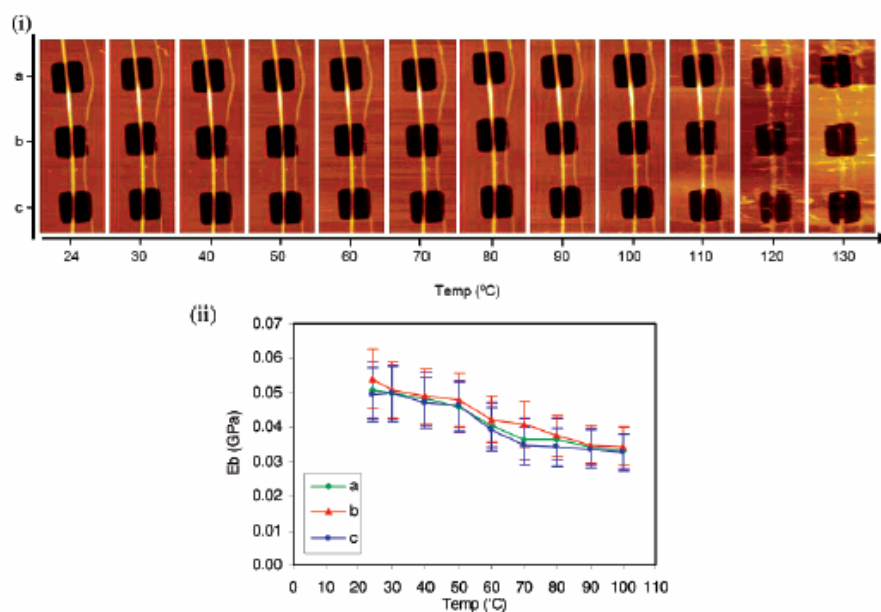


Figure 3. AFM images of FF nanotubes at different temperatures. (i) Sequence of images of the same two fibrils at the temperature from 24 to 130 °C. The size of each image is 30 μm (height) \times 10 μm (width). Three lines on Figure 3 (ii) show the E_{bending} at three holes (a, b, c) corresponding to the left fibril on (i) at temperature from 24 to 100 °C.

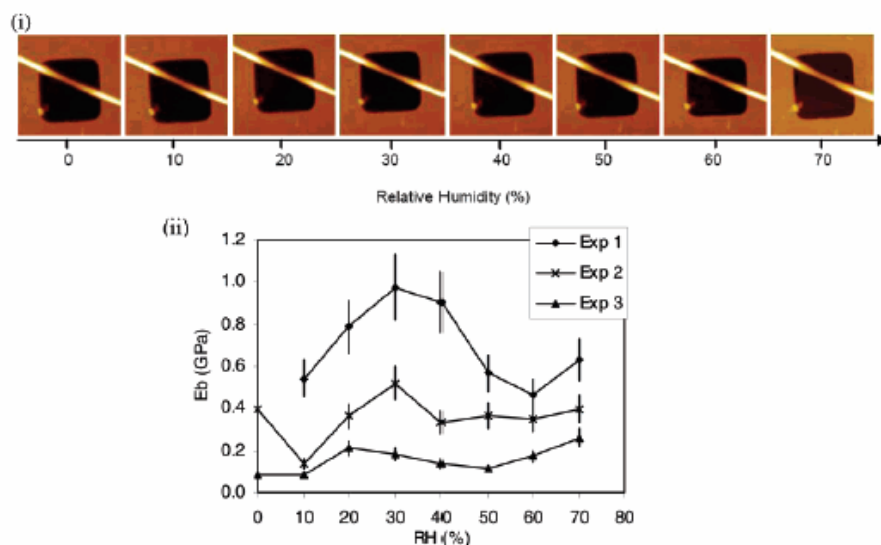


Figure 4. AFM images of FF nanotubes at different relative humidities. (i) Sequence of images of a same fibril lying across a hole at relative humidity from 0% to 70%. The size of each image is 10 μm \times 10 μm . (ii) E_{bending} of three different fibrils in three different elasticity vs humidity experiments.

magnitude. Our results agreed with the result from direct force measurement.¹⁴ Our results also showed that G is only 1–3% of E . For ordinary material, which is homogeneous and linearly elastic, G is 0.3 to 0.5 times E . The low G/E ratio means FF fibrils are anisotropic materials, and the FF peptides are relatively strongly bound in the longitudinal direction compared to the axial direction. In FF fibrils, there are hydrogen bonds and aromatic stacking interactions between the individual FF peptides.⁸ It is possible that hydrogen bonds contribute more in the longitudinal direction, while aromatic stacking interactions contribute more in the axial direction.

A previous high-resolution scanning electron microscope (HRSEM) study showed that the FF nanotubes kept the same morphology at temperatures up to 150 °C.¹² In a previous AFM study, Sedman et al. showed that FF nanotubes kept the wall integrity at temperatures up to 100 °C in situ. On increasing the temperature further to 150 °C, the nanotubes lost spatial volume. They suggested that this was possibly because of the loss of water from the FF nanotubes, and that the elevated temperature made the nanotubes more deformable and they became distorted by the AFM probe as part of the imaging process.¹³ Time-of-flight secondary ion mass spectrometry (ToF-SIMS) analysis

suggested that at temperatures at and above 150 °C, the loss in mass and apparent degradation in the nanotubes morphology is due to the loss of free phenylalanine.¹³ The present AFM study showed that the elasticity as well as morphology of FF nanotubes remained stable from room temperature up to 100 °C during the experimental time scale. This consists with all the previous studies. The present study also shows that the value of E_{bending} gradually decreased $\sim 30\%$ at temperature from 24 to 100 °C. A possible reason could be that the increase in temperature increases the movement of FF peptides in the FF fibril, which decreases the strength of the hydrogen bonds and aromatic stacking interactions between them. This causes the decreasing of E and G , which results in the decrease of E_{bending} .

Conclusions

We investigated the elastic properties of FF nanotubes by applying the bending-beam model to AFM images. We obtained the Young's modulus E of 27 ± 4 GPa and the shear modulus G of 0.21 ± 0.03 GPa of FF fibrils. We also showed that FF nanotubes kept their rigidity at temperature from room temperature up to 100 °C and relative humidity from 0% to 70%. Our study provided a better understanding of the structure and properties of FF nanotubes, which are important for their potential applications in biotechnology, such as biosensors, nanoelectromechanics, and medical devices.

LA7010106